

**DESIGNING AND MANUFACTURING OF
POROUS SPINAL CAGES USING Ti6Al4V
FOAMED METAL**

**A Thesis Submitted to
the Graduate School of Engineering and Sciences of
İzmir Institute of Technology
in Partial Fulfillment of the Requirements for the Degree of**

MASTER OF SCIENCE

in Mechanical Engineering

**by
M.Eren DİZLEK**

**July 2009
İZMİR**

We approve the thesis of **Mustafa Eren DİZLEK**

Prof. Dr. Mustafa GÜDEN
Supervisor

Prof. Dr. Ahmet ÇAKIR
Committee Member

Assoc. Prof. Dr. Hasan YILDIZ
Committee Member

03 July 2009

Assoc. Prof. Dr. Metin TANOĞLU
Head of the Mechanical Engineering
Department

Prof. Dr. Hasan BÖKE
Dean of the Graduate School of
Engineering and Sciences

ACKNOWLEDGEMENTS

My journey started as an engineering position in Hipokrat A.Ş. and continued as a research assistant in the Department of Mechanical Engineering at İzmir Institute of Technology, İzmir.

First and foremost, I wish to thank my advisor Professor Mustafa Güden for his supervision, kind guidance, encouragement and support during my studies and the project. I consider myself lucky to have a chance for working with him.

I am grateful to Hipokrat A.Ş. and Ministry of Trade and Industry for their financial support to my thesis project (Project grant: 00054.STZ.2007-1). Also I would like to thank my colleagues and friends working in my laboratory for their valuable suggestions and assistance on my studies.

For their endless support and motivation during my study and all my life, I would like to thank my parents and specially my sister, Ceren Dizlek.

A very special thank goes to a very special girl, Burcu Çabuk, for her great support, patience and giving motivation during my study and being a part of my life. Her existence gave power to finish my thesis study.

ABSTRACT

DESIGNING AND MANUFACTURING OF POROUS SPINAL CAGES USING Ti6Al4V FOAMED METAL

Open cell Ti6Al4V foams with varying porosities (50, 60 and 70%) were prepared at sintering temperatures between 1200 and 1350 °C using ammonium bicarbonate particles (315 - 500 µm) as space holder. Two different biomedical grade commercial, gas atomized spherical Ti6Al4V powders were used to prepare foams. Powder 1 was in size range of between 45 - 150 µm and Powder 2 in size range of between 30 - 90 µm. The foams were sintered under argon atmosphere in a tightly enclosed tube furnace. The resulting cellular structure of the foams showed bimodal pore size distribution, comprising macro pores (300 - 500 µm) and micro pores (1 - 30 µm). Compression tests of foam samples have shown that increasing sintering temperature or decreasing porosity increased the elastic modulus, yield and compressive strength and failure strain. The improvement in the mechanical properties of foams prepared using smaller size Ti6Al4V powder with bimodal particle distribution were attributed to the increased number of sintering necks and contact areas between the particles. The foam prepared with optimum porosity, pore size and mechanical properties for bone in-growth was further used to produce prototype porous spinal cages which are widely used in spinal surgery for vertebrae fixation. The geometries and size of the prototype spinal cages were determined through the measurements taken from human vertebrae. The foams for spinal cage preparation were first prepared in the form of plates and then core-drilled using water jet based on the design geometrical parameters determined for each vertebra segment.

ÖZET

Ti6Al4V KÖPÜK METAL İLE GÖZENEKLİ SPİNAL KAFES TASARIMI VE İMALATI

Farklı gözenek oranlarına sahip (%50, %60 ve %70) açık hücreli Ti6Al4V köpükler amonyum bikarbonat parçaları (315 - 500 µm) boşluk yapıcı madde olarak kullanılarak ve 1200 - 1350 °C arası sıcaklıklarda sinterlenerek hazırlanmıştır. Çalışmada iki tip, biyomedikal kullanıma uygun, ticari, gaz atomizasyonu yöntemiyle elde edilen küresel Ti6Al4V tozları kullanılmıştır. Toz 1 45 - 150 µm ve Toz 2 30 - 90 µm arası tanecik boyutuna sahiptir. Köpükler sıkıca yalıtılmış tüp fırın içerisinde argon atmosferi altında sinterlenmiştir. Elde edilen hücresel yapıdaki köpüklerde 300 - 500 µm arası makro ve 1 - 30 µm arası mikro olmak üzere iki tip gözenek modelinin oluştuğu gözlenmiştir. Köpük numuneler üzerinde uygulanan basma testleri artan sinterlenme sıcaklığının ve/veya azalan gözenek yüzdesinin, yapının elastik modülünü, akma mukavemetini, basma dayanımını ve ayrılma deformasyon oranını yükselttiği göstermiştir. Daha düşük tanecik boyutuna sahip Ti6Al4V tozun kullanılmasıyla köpük yapının mekanik özelliklerinin iyileştiği, bu iyileşmenin artan tanecik temas noktası ve toplam sinterlenme bölgesi alanına bağlı olduğu belirlenmiştir. Kemik entegrasyonu için optimum gözenek boyutu, gözenek yüzdesi ve mekanik özelliklerine sahip köpük yapılar, spinal cerrahide vertebra sabitlenmesinde sıkça kullanılan, gözenekli spinal kafes prototiplerinin üretilmesinde kullanılmıştır. Spinal kafes prototiplerinin şekilleri ve boyutları insan omurgasından alınan ölçümlere göre belirlenmiştir. Köpükler önce plaka şeklinde üretilmiş, sonra spinal kafesler su jeti ile kesme yöntemiyle, plakalardan her vertebra segmenti için tasarlanan şekillere göre kesilerek çıkartılmıştır.

TABLE OF CONTENTS

| | |
|---|----|
| LIST OF TABLES | ix |
| LIST OF FIGURES | x |
| CHAPTER 1. INTRODUCTION..... | 1 |
| CHAPTER 2. SKELETAL SYSTEM AND BONE | 4 |
| 2.1. Bone Structure | 4 |
| 2.2. Bone Formation (Ossification)..... | 9 |
| 2.3. Bone Fracture Healing | 9 |
| 2.4. Skeletal System | 10 |
| 2.5. Bone Types in Human Skeletal System..... | 11 |
| 2.6. Vertebral Column (Spine)..... | 12 |
| 2.6.1. Intervertebral Discs | 13 |
| 2.6.2. Vertebrae | 14 |
| 2.7. Vertebral Disc Diseases | 15 |
| 2.8. Spinal Surgery..... | 16 |
| CHAPTER 3. POROUS BIOMATERIALS: MANUFACTURING AND BONE INGROWTH PROPERTIES | 20 |
| 3.1. Bone Ingrowth into Porous Implants | 20 |
| 3.2. Fabrication Methods of Porous Metals | 24 |
| 3.2.1. Fabrication Techniques for Closed-Cell Porous Metals | 26 |
| 3.2.2. Fabrication Techniques for Open-Cell Porous Metals..... | 28 |
| 3.2.2.1. Non-Homogeneous Pore Distribution | 28 |
| 3.2.2.1.1. Sintering Metal Powders and Fibers | 28 |
| 3.2.2.1.2. Space Holder Method..... | 29 |
| 3.2.2.1.3. Replication | 29 |
| 3.2.2.1.4. Combustion Synthesis..... | 30 |
| 3.2.2.2. Homogeneous Pore Distribution | 31 |

| | |
|--|--------|
| 3.2.2.2.1. Orderly Oriented Wire Mesh | 31 |
| 3.2.2.2.2. Vapor Deposition | 31 |
| 3.2.2.2.3. Ferromagnetic Fiber Array..... | 32 |
| 3.2.2.2.4. Rapid Prototyping | 32 |
| 3.2.2.3. Functionally Graded Pore Distribution..... | 33 |
| 3.2.2.3.1. Electro Discharge Compaction | 33 |
| 3.3. Processing of Ti and Ti6Al4V Foams | 34 |
| 3.3.1. Sintering of Powder Compacts..... | 35 |
| 3.3.2. Hollow Sphere Sintering | 36 |
| 3.3.3. Space Holder Method..... | 37 |
| 3.3.4. Sintering of Powders Deposited on a Fugitive Scaffold | 38 |
| 3.3.5. Powder Densification in Presence of Expansion of Trapped Gas Bubbles. | 39 |
| CHAPTER 4. MATERIALS AND METHODS | 41 |
| 4.1. Materials | 41 |
| 4.2. Preparation of Foams | 44 |
| 4.3. Equipment | 48 |
| 4.4. Designing Spinal Cages | 48 |
| CHAPTER 5. RESULTS AND DISCUSSIONS | 51 |
| 5.1. Materials | 51 |
| 5.2. Microstructure of Ti6Al4V Powders | 52 |
| 5.3. Porosity | 58 |
| 5.4. Compression Tests | 64 |
| 5.4.1. Stress-Strain Curves of Ti6Al4V Foam Samples..... | 64 |
| 5.4.2 Failure Mechanism of Foams..... | 71 |
| 5.5. Design of the Spinal Cages | 76 |
| 5.6. Comparative Analysis..... | 79 |
| CHAPTER 6. CONCLUSION | 82 |
| REFERENCES | 84 |

APPENDICES

APPENDIX A. ASTM F1580-1 STANDARD 90

APPENDIX B. TECHNICAL DRAWINGS AND SOLID MODELS OF
DESIGNED SPINAL CAGES 94

LIST OF TABLES

| <u>Table</u> | <u>Page</u> |
|---|--------------------|
| Table 2.1. A literature survey of methods for determining the elastic modulus of trabecular bone material and the resulting estimate values | 7 |
| Table 2.2. Spinal disc replacement devices. | 17 |
| Table 2.3. Spinal cages for bone ingrowth. | 19 |
| Table 3.1. The comparison of bone fusion over post-surgery recovery time. | 22 |
| Table 3.2. The fabrication methods of metallic porous structures and classifications based on the resulting pores structure. | 25 |
| Table 3.3. Comparison of Elastic moduli of metallic implant materials with human cortical bone (in GPA) | 34 |
| Table 4.1. ASTM standard for Ti6Al4V powder and chemical composition of used powders..... | 42 |
| Table 4.2. Mixture weight of Ti6Al4V, Ammonium bi Carbonate powders and PVA solution for fabrication of 1 cm ³ foam structure. | 46 |
| Table 5.1. Wt.% oxygen content of as received powder and foam samples sintered between 1200 and 1350 °C..... | 58 |
| Table 5.2. Mean percent porosity of foams as function of sintering temperature. | 59 |
| Table 5.3. Average elastic modulus of 60% porous foams as function of sintering temperature. | 66 |
| Table 5.4. Mean elastic modulus of 1300 °C sintered foams as function of Vol. % porosity and compression strain rate. | 71 |
| Table 5.5. Comparison of Ti6Al4V foams to the other porous structured biomedical materials. | 81 |

LIST OF FIGURES

| <u>Figure</u> | <u>Page</u> |
|--|--------------------|
| Figure 2.1. Schematic of bone structure. | 5 |
| Figure 2.2. Radiological picture of cortical and cancellous bone..... | 6 |
| Figure 2.3. Primary compression trabeculae and tensile trabeculae..... | 6 |
| Figure 2.4. Cortical bone cross-section structure showing osteons, haversian canals and surrounding cement..... | 8 |
| Figure 2.5. Volkmann’s canal connecting Haversian canals between osteons..... | 8 |
| Figure 2.6. Major phases of bone fracture healing; a) Hematoma Formation b) Fibrocartilaginous Callus Formation c) Bony Callus Formation d) Remodeling | 10 |
| Figure 2.7. Human skeletal system..... | 11 |
| Figure 2.8. Examples of bone types; a) humerus (long bone), b) wrist bones (short bone), c) sternum (flat bone), d) vertebrae (irregular bone), e) patella (sesamoid bone)..... | 11 |
| Figure 2.9. Human spine and its regions..... | 13 |
| Figure 2.10. Structure of vertebrae | 14 |
| Figure 2.11. Intervertebral disc diseases..... | 16 |
| Figure 2.12. Interbody spinal cage implantation | 18 |
| Figure 3.1. Photography of a) Biorthex - ActiPore interbody fusion device with 230±130 µm pores, 65±5% porosity in Ø11x22 mm dimensions, b) Sulzer – BAK hollow threaded Ti6Al4V fusion cage in Ø11x22 mm dimensions..... | 22 |
| Figure 3.2. Light-microscope micrographs of porous a) ActiPore sample, b) BAK Spinal Cage sample transverse section over post surgery recovery time: 1) 3 months, 2) 6 months, and 3) 12 months..... | 23 |
| Figure 3.3. Soft tissue fiber orientation in the presence of porous a) spinal device, b) solid spinal cage at 3 months of post-instrumentation..... | 24 |
| Figure 3.4. The foam casting process employed by CYMAT; the process is composed of melting and holding furnaces, the foaming box, and foaming equipment, and a twin-belt caster..... | 26 |

| | | |
|--------------|--|----|
| Figure 3.5. | ALPORAS foam processing..... | 26 |
| Figure 3.6. | ALULIGHT and FOAMINAL foam processing..... | 27 |
| Figure 3.7. | Schematic of plasma spraying process | 28 |
| Figure 3.8. | Schematic of biocompatible porous Ti foam processing using space holder | 29 |
| Figure 3.9. | Schematic of three steps of replication method of foam processing | 30 |
| Figure 3.10. | Schematic of combustion synthesis process..... | 30 |
| Figure 3.11. | Schematic of chemical vapor deposition process which involves the use of an intermediate reticulated vitreous carbon substrate..... | 31 |
| Figure 3.12. | Schematic representation of a bonded array of randomly-oriented magnetic fibers deformation in a magnetic field..... | 32 |
| Figure 3.13. | Schematic of three dimensional printing (sintering) process | 33 |
| Figure 3.14. | Schematic of FAST process | 34 |
| Figure 3.15. | Schematic of solid-state processing of Ti and Ti6Al4V foams; a) powder compact sintering, b) hollow sphere sintering, c) space holder method, d) sintering of powders deposited on scaffold, e) powder densification in presence of gas, and expansion of trap. | 35 |
| Figure 3.16. | Schematic of solid hollow sphere processing..... | 37 |
| Figure 3.17. | Sintering of hollow sphere structures | 37 |
| Figure 3.18. | Schematic of space holder method of Ti foam processing..... | 38 |
| Figure 3.19. | SEM micrograph of reticulated Ti6Al4V foam produced by sintering of powders deposited on a fugitive scaffold..... | 39 |
| Figure 3.20. | Schematic of foaming process, where titanium powders are compacted by hot isostatic pressing in the presence of argon and the resulting high-pressure argon bubbles then expand under low-pressure argon atmosphere at high temperature by Murray and Dunand | 40 |
| Figure 4.1. | Crucible Research Ti6Al4V powders as received..... | 41 |
| Figure 4.2. | Powder particle size vs. distribution; a) Powder 1 and b) Powder 2 | 42 |
| Figure 4.3. | SEM micrographs showing the particles in a) Powder 1 and b) Powder 2..... | 43 |
| Figure 4.4. | SEM micrographs of irregular ammonium bi carbonate space holder particles..... | 44 |
| Figure 4.5. | Preparation route for Ti6Al4V foams using space holder method..... | 45 |

| | | |
|--------------|---|----|
| Figure 4.6. | Heating profile of the furnace at a sintering temperature of 1200 °C | 46 |
| Figure 4.7. | a) Water-jet cut foam sample sintered at 1350 °C (40 x 40 x 15 mm), b) cylindrical compression test sample (10 x 15 mm) and c) direct molding sample | 47 |
| Figure 4.8. | Designing route of Ti6Al4V spinal cages | 49 |
| Figure 4.9. | Vertebra sections; 1. vertebral disc, 2. spinous, 3. articular, 4. transverse, 5. foramen, 6. pedicle, 7. vertebral disc wall..... | 50 |
| Figure 5.1. | TGA and DTG curves of a) Ammonium bi carbonate, b) Urea and c) PVA | 51 |
| Figure 5.2. | SEM images of epoxy mounted and polished as-received powders a) Powder 1 and b) Powder 2 | 53 |
| Figure 5.3. | Magnified SEM images showing fine needle like α -phases for a) Powder 1 and b) Powder 2 | 54 |
| Figure 5.4. | XRD spectra of sintered a) Powder 1 and b) Powder 2 foams and as- received powder..... | 55 |
| Figure 5.5. | SEM micrographs of sintered samples at sintering temperature a) 1200 °C and b) 1350 °C for 2h..... | 56 |
| Figure 5.6. | Light optical micrographs of sintered samples at sintering temperature a) 1200 °C and, b) 1350 °C for 2h..... | 57 |
| Figure 5.7. | Pseudo-binary Ti-6Al-4V Diagram..... | 57 |
| Figure 5.8. | Pictures of a) sintered foam (1300 °C) and b) green compact. | 60 |
| Figure 5.9. | SEM micrograph of typical water jet cut surface of a Ti6Al4V foam | 61 |
| Figure 5.10. | Optical micrograph of Powder 2 foam cell structure (sintered at 1300 °C)..... | 61 |
| Figure 5.11. | Optical micrographs showing Ti6Al4V particles in the cell walls: a) Powder 2 foam sintered at 1200 °C, b) Powder 2 foam sintered at 1350 °C and c) Powder 1 foam sintered at 1350 °C..... | 62 |
| Figure 5.12. | Optical micrographs showing Ti6Al4V foam cell walls a) Powder 2 green compact, b) Powder 2 foam sintered at 1200 °C and c) Powder 2 foam sintered at 1350 °C | 63 |
| Figure 5.13. | Compression stress-strain curves of three Powder 2 foam samples sintered at 1350 °C | 64 |
| Figure 5.14. | Typical stress-strain curves of 60% porous Powder 1 foams sintered at different temperatures (strain rate: 10^{-3} s^{-1}) | 65 |

| | |
|--|----|
| Figure 5.15. Typical stress-strain curves of 60% porous Powder 2 foams sintered at different temperatures (strain rate: 10^{-3} s^{-1}) | 66 |
| Figure 5.16. Variation of yield strength of 60% porous foams as a function of sintering temperature | 67 |
| Figure 5.17. Variation of compressive strength of 60% porous foams as a function of sintering temperature | 67 |
| Figure 5.18. Stress-strain curves of 50, 60 and 70 % porous Powder 2 foams sintered at 1300 °C (strain rate: 10^{-3} s^{-1})..... | 68 |
| Figure 5.19. Variation of yield strength of foams as a function of porosity..... | 68 |
| Figure 5.20. Variation of compressive strength of foams as a function of porosity..... | 69 |
| Figure 5.21. Stress-strain curves of 50, 60 and 70 % porous Powder 2 foams sintered at 1300 °C (strain rate: 10^{-1} s^{-1})..... | 70 |
| Figure 5.22. Variation of elastic modulus of foams sintered at 1300 °C as a function of porosity. | 70 |
| Figure 5.23. Compression stress strain curve of 60% porous Powder 2 foam sintered at 1350 °C showing deformation regions | 72 |
| Figure 5.24. Deformed samples of Powder 2 foams sintered at 1350 °C; strains a) 0.12, b) 0.18, c) 0.26 and d) 0.4..... | 72 |
| Figure 5.25. Optical micrographs showing; a) development of contacts between non-contacting particles, b) relative movement of bonded particles, c) crack propagation in bonding regions and d) separation of bonded particles..... | 73 |
| Figure 5.26. SEM micrograph of failed and separated sections of Powder 2 foam sample sintered at 1350 °C, showing debonded particles | 74 |
| Figure 5.27. SEM micrograph of failed and separated sections of Powder 2 foam sample sintered at 1350 °C, a) the different fracture modes in region A and B, b) brittle fracture in region A and c) ductile fracture in region B | 75 |
| Figure 5.28. Draft of C7 coded spinal cage indicated in blue color | 76 |
| Figure 5.29. a) Defined sketch of C7 spinal cage and b) verification of dimensions..... | 77 |
| Figure 5.30. L4-L5 (Lumbar 4 th and 5 th) spinal cage designs in thickness of a) 6 mm, b) 8 mm and c) 10 mm | 77 |
| Figure 5.31. C7 coded spinal cage a) 3D model and b) processed sample..... | 78 |

Figure 5.32. Spinal cage samples of a) direct molding and b) water jet cutting
method 79

Figure 5.33. Edge sections of a sample which cut through water jet..... 79

CHAPTER 1

INTRODUCTION

The replacement of tissues and complete organs damaged by disease or trauma is a challenge for materials science for the last couple of decades. There have been significant advances in the biomaterials science and biotechnology resulted in wide range of applications in orthopedic and dental implant and prosthesis applications for repair or replacement of natural tissues. Researches in this field lead to development of new biocompatible materials. Materials in applications include wide range of choices that fall into four different groups: metals, ceramics, polymers and composites. In the case of skeletal system, biomaterials must possess adequate mechanical, morphological and physico-chemical properties to achieve a high degree of bio-compatibility and bio-functionality. For these purposes, metals have a particular importance of their load-bearing ability (Agrawal 1998).

Despite of their relatively high cost and complex route of production, the bulk form of titanium and some titanium based alloys including Ti6Al4V have been widely used in orthopedics and dentistry due to their good biocompatibility, high strength-to-weight ratios, relative low elastic modulus, high fatigue strength, and excellent corrosion resistance as compared with widely used 316L stainless steel and Co-Cr-Mo alloys (Okazaki, et al. 1998, Okazaki, et al. 2001, Long and Rack 1998). Unfortunately, most bulk metallic implant materials in use, including titanium and its alloys, suffer from problems of interfacial stability with host tissues, biomedical mismatch of elastic moduli, production of wear debris and maintenance of a stable blood supply (Song, et al. 1999). Nevertheless, the porous implant components based on biocompatible metallic materials (e.g., Ti and Ti6Al4V) are known to promote interactions between bone and the surrounding tissue (Pillar 1987). Pores facilitate the bone tissue formation by allowing the migration and proliferation of osteoblasts and mesenchymal cells by the help of transportation of body fluid through three-dimensional interconnected array of pores (Weiner and Wagner 1998). In addition, a porous surface provides mechanical

interlocking between the implant and surrounding bone tissue, enhancing mechanical stability at the interface which has fatal importance for bone growth. Furthermore, relatively low elastic moduli of porous metals compared to the bulk forms is expected to reduce the extent of stress shielding which causes the well-known implant loosening and prolong the implant life-time (Long and Rack 1998).

Bone is one of the few organs capable of self-regeneration following injury. For a best replacement of bone, implants must have two most critical characteristics of natural bone tissues which are being capable of self-repairing and modifying their structure and properties in response to environmental input such as mechanical load or body fluid flow. Since these features belong to cells, best replacement of bone could be possible only by providing an artificial porous scaffold, or matrix, which imitates the body's own extracellular matrix, onto which cells attach, migrate, multiply and function. These porous biomaterials, including the Ti6Al4V open cell foams, provide better environment and hence assist the healing process. Ti6Al4V open cell foam structured implants are better substitute for replacing defected bone, especially spinal disc disorders, since healing time and condition mostly depend on the level of locking of upper and lower vertebra segments.

Implant matrix must be designed to satisfy several requirements. First, material must be biocompatible and bioactive. Ti and Ti6Al4V are known to satisfy these requirements (ASTM F136-82, ASTM F1580-1). The porous structure must also be highly porous to provide sufficient space for the attachment and proliferation of new bone tissues and transport of the body fluids. The minimum pore size convenient for bone formation was reported to be larger than 100 μm (Hulbert 1970) while the tendency of fibrous tissue formation was shown to increase above the pore size of 1 mm (Boby and Miller 1994). With these upper and lower size limits, the optimum pore size range for bone formation was reported 200-500 μm . Finally, matrix material must resist handling during the implantation and in vivo loading.

Open cell structured Ti and Ti6Al4V foams and compacts, potentially to be used in biomedical applications, were previously prepared using powder metallurgical processes, known as direct sintering and space holder methods. Additionally, other powder metallurgical techniques are available including hollow sphere sintering, sintering of powders deposited on fugitive scaffold and powder densifications in presence of gas bubbles as well (Dunand 2004). Space holder method is commonly chosen due to its simplicity, effectiveness and capability of manufacturing matrixes

which have adequate strength and optimum, almost uniform pore size and porosity. Space holder method allows the preparation of foams with wider range of porosity (40-80%) and pore size. Furthermore, the sintering process allows either direct net shape manufacturing of implants or manufacturing in a simple geometrical shape following its cutting through water jet to extract the finer dimensional tolerances of the implant.

The ultimate goal of this experimental project was to manufacture the Ti6Al4V porous spinal gages using space holder method. Foams were prepared using commercially available biocompatible ASTM 1580-1 certificated Ti6Al4V powders with two different powder size distributions. The designing efforts of the spinal cages were based on the measurements taken from the segments of human vertebral system. The prepared foams were further implanted to one year old male sheep and found to be successful in bone growing inside the pores. In addition to this preliminary implantation, detailed investigations are certainly needed to verify the effect of porous structure on the bone in-growth properties.

CHAPTER 2

SKELETAL SYSTEM AND BONE

2.1. Bone Structure

Bones are rigid organs that form parts of the endoskeleton and vertebrates. They function to move, support and protect the various organs of the body, produce red and white blood cells and store minerals. As bones have variety of shapes and complex internal and external structure, they are lightweight, strong and hard materials. Bone structure is a highly organized and specialized connective tissue. It is important to understand bone complex structure in details to comprehend how complex process of bone healing occurs in fractures heal and implant fixation. Bone homeostasis is contributed by three types of cells consisting osteoblasts, osteoclasts and osteocytes. Osteoblasts are bone-forming cells, osteoclasts cells resorb or break down bone and osteocytes are mature bone cells. Equilibrium between osteoblasts and osteoclasts maintains bone tissue. The structure of bone is schematically shown in Figure 2.1.

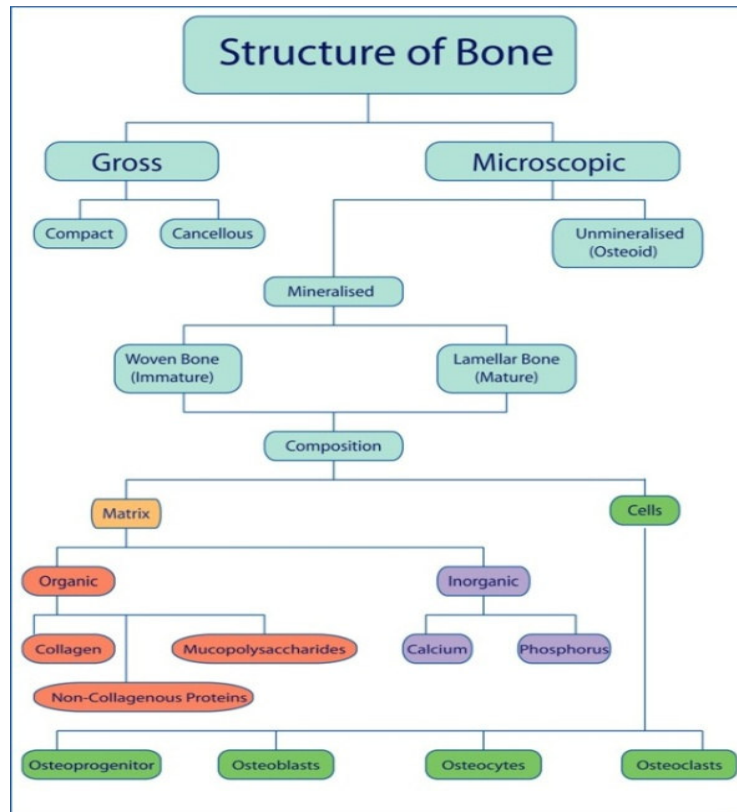


Figure 2.1. Schematic of bone structure.
(Marieb 1998)

At macroscopic scale bone has two segments with different properties. These segments are covered by periosteum which is a protective shell. Outer dense cortex is called cortical (compact) bone or dense bone (Figure 2.2). The cortical bone resists bending, has a porosity ranging between 5% and 10% and usually found along the exterior shaft section of long bones. Cancellous bone (spongy and trabecular) is seen in the interior of mature bones (Figure 2.2). Spongy structure gives resistance against compression forces. It has relatively high porosity levels, ranging between 75% and 95%. This kind of bones usually found in cuboidal (vertebrae segments) and flat bones (e.g. pelvis) and at end of the long bones (e.g. femur). The non-mineralized spaces within trabecular bone contain bone marrow, which is a tissue composed of blood vessels, nerves, and various types of cells. Bone elements place or displace themselves in the direction of functional pressure according to the Wolff's Law as shown in Figure 2.3. Cortical bone accounts for about 80% of the total skeletal mass while cancellous bone constitutes 70% of the skeletal volume (Nather, et al. 1998).

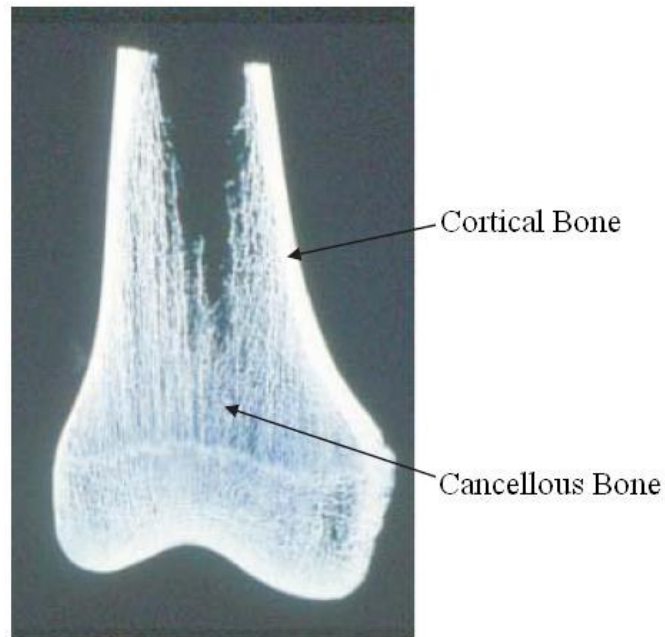


Figure 2.2. Radiological picture of cortical and cancellous bone.
(Source: Nather, et al. 1998)

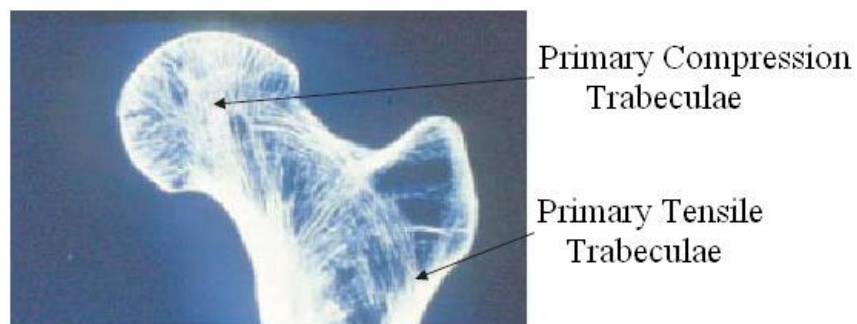


Figure 2.3. Primary compression trabeculae and tensile trabeculae.
(Source: Nather, et al. 1998)

A literature survey of measured and estimated values of the modulus trabecular bone material shows that moduli values range from 1 to 20 GPa (Rho, et al. 1998). Rho, et al. summarized former researches shown in Table 2.1.

Table 2.1. A literature survey of methods for determining the elastic modulus of trabecular bone material and the resulting estimate values. (Source: Rho, et al. 1998)

| Source | Test method | Elastic modulus (GPa) |
|---------------------------|---|--|
| Wolff (1892) | Hypothesis | 17–20 (assumption) |
| Runkle and Pugh (1975) | Buckling | 8.69 ± 3.17 (dry) |
| Townsend et al. (1975) | Inelastic buckling | 11.38 (wet) |
| Williams and Lewis (1982) | Back-calculating from finite element models | 1.30 |
| Ashman and Rho (1988) | Ultrasound test method | 12.7 ± 2.0 (wet) |
| Ryan and Williams (1989) | Tensile testing | 0.76 ± 0.39 |
| Hodgskinson et al. (1989) | Micro hardness | 15 (estimation) |
| Kuhn et al. (1989) | Three-point bending | 3.81 (wet) |
| Mente and Lewis (1989) | Cantilever bending with finite element analysis | 7.8 ± 5.4 (dry) |
| Choi et al. (1990) | Four-point bending | 5.35 ± 1.36 (wet) |
| Rho et al. (1993) | Tensile testing | 10.4 ± 3.5 (dry) |
| | Ultrasound test method | 14.8 ± 1.4 (wet) |
| Rho et al. (1997) | Nanoindentation | 19.6 ± 3.5 (dry): longitudinal 15.0 ± 3.0 (dry): transverse |

Microscopic structure of bone tissue consists of two main types. Primary bone tissue (non-lamellar, coarse fibered, woven or immature bone) is characterized by the presence of randomly oriented coarse collagen fibers clearly visible under polarization microscopy. Non-lamellar bone is seen in the bones of fetuses and young children. It is the osseous tissue first deposited on the calcified cartilage matrix in endochondral ossification. It is also the first tissue appearing in the healing of the fractured bone. Secondary bone tissue (lamellar bone) is known as mature bone. Mature bone characterized by the presence of collagen fibres arranged in parallel layers or sheets (lamellae) readily apparent when viewed under polarization microscope. Lamellar bone is present in both structured types of adult bone; cortical (compact) bone and cancellous (spongy or trabecular) bone.

At the tissue level, major differences can be identified within the cortical and cancellous bone structures. Cortical bone is composed of repeating units called osteons or Haversian systems (Figure 2.4.). The osteons are cylindrical, about 200-250 µm in diameter, arranged roughly parallel to the centerline axis of the bone. The central cavity

inside an osteon is known as the Haversian canal. Haversian canals are typically 40-50 μm in diameter run along the axis of the bone. Haversian system or osteons have concentric layers of mineralized collagen fibers (lamellae), which deposited around Haversian canals containing blood vessels and nerves servicing the bone. Short transverse canals connecting the Haversian canals are called Volkmann's canals (Figure 2.5). These canals also contain blood vessels and nerves.

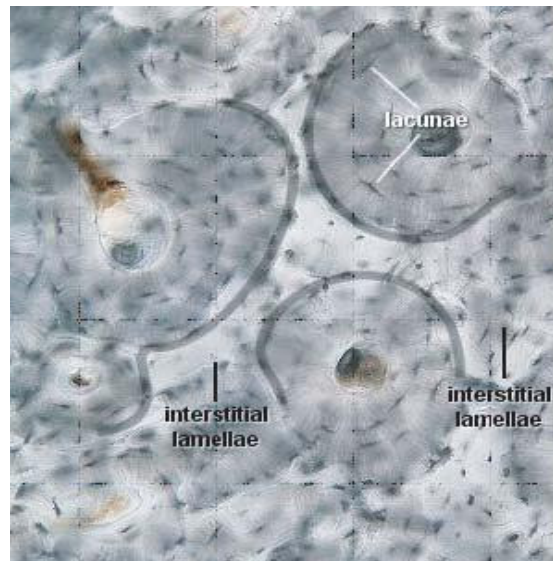


Figure 2.4. Cortical bone cross-section structure showing osteons, haversian canals and surrounding cement. (Source: Nather, et al. 1998)

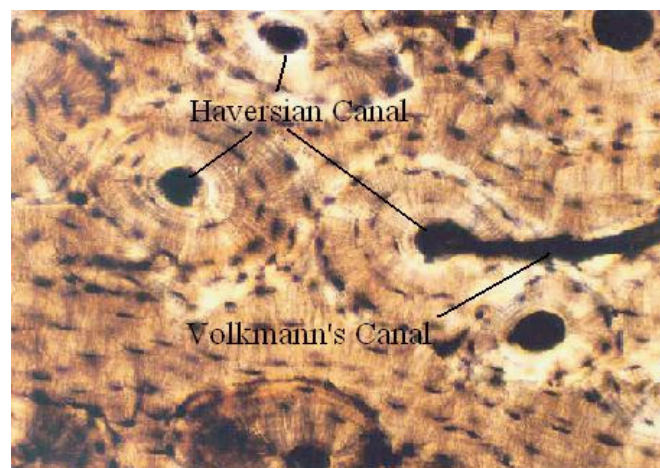


Figure 2.5. Volkmann's canal connecting Haversian canals between osteons. (Source: Nather, et al. 1998)

2.2. Bone Formation (Ossification)

There are two kinds of bone formation processes; intramembranous ossification and endochondral ossification. In both cases, pre-existing connective tissue transforms to bone. In Intramembranous ossification, some mesenchyme cells are transformed into osteoblasts and start forming the bone. This is an ossification process that transforms membrane into bone. Additionally, bone is formed around the edge of this centre until the entire membrane is ossified. In endochondral ossification, a hyaline cartilage model of the bone is ossified.

2.3. Bone Fracture Healing

Fracture healing is a complex process that undergoes four major phases. The main steps of healing of bone tissue are schematically shown in Figure 2.6. When a bone fractures, the blood vessels in the bone, periosteum and surrounding tissues are also damaged. This results in a mass of clotted blood, or hematoma, forming at the fracture site (Figure 2.6 a)). Capillaries grow into the hematoma and phagocytic cells consume the cellular debris. Fibroblasts and osteoblasts also migrate into the hematoma from the periosteum and endosteum. Some fibroblasts and osteoblasts change and start to produce cartilage. Some fibroblasts produce collagen fibers that link the broken bones together, while some osteoblasts start producing spongy bone (Figure 2.6 b)). The entire mass of soft tissues being produced is called fibrocartilaginous callus and serves to splint the fractured bone together (Figure 2.6 b)). Osteoblasts and osteoclasts continue to migrate into the fibrocartilaginous callus and convert the existing callus to a bony callus made up of spongy bone (Figure 2.6 c)). The bony callus forms 3-4 weeks after a fracture occurs and firmly binds the bone together in 3-4 months. During the bony callus formation, and for the next several months, the bony callus is remodeled (Figure 2.6 d)). Excess bone in the medullary cavity and on the diaphysis is removed and compact bone is deposited to reinforce the fracture area.

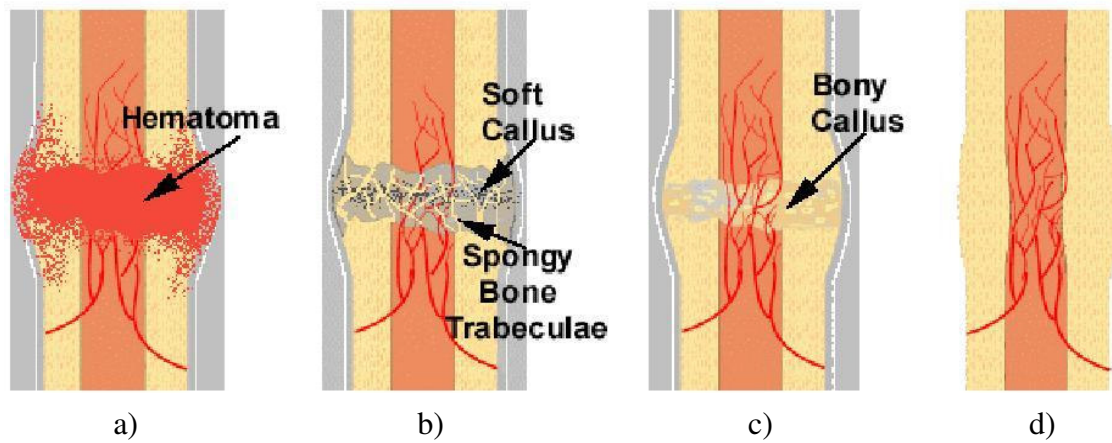


Figure 2.6. Major phases of bone fracture healing; a) Hematoma Formation b) Fibrocartilaginous Callus Formation c) Bony Callus Formation d) Remodeling. (Source: British Columbia 2003)

2.4. Skeletal System

All bones in the body are referred to collectively as the skeletal system. Main functions of the skeletal system are to protect some organs and support and move the body. Figure 2.7 shows the bones of the adult human skeletal system and their positions. There are totally 206 bones in the adult human body and about 270 in an infant (Mader 2005).

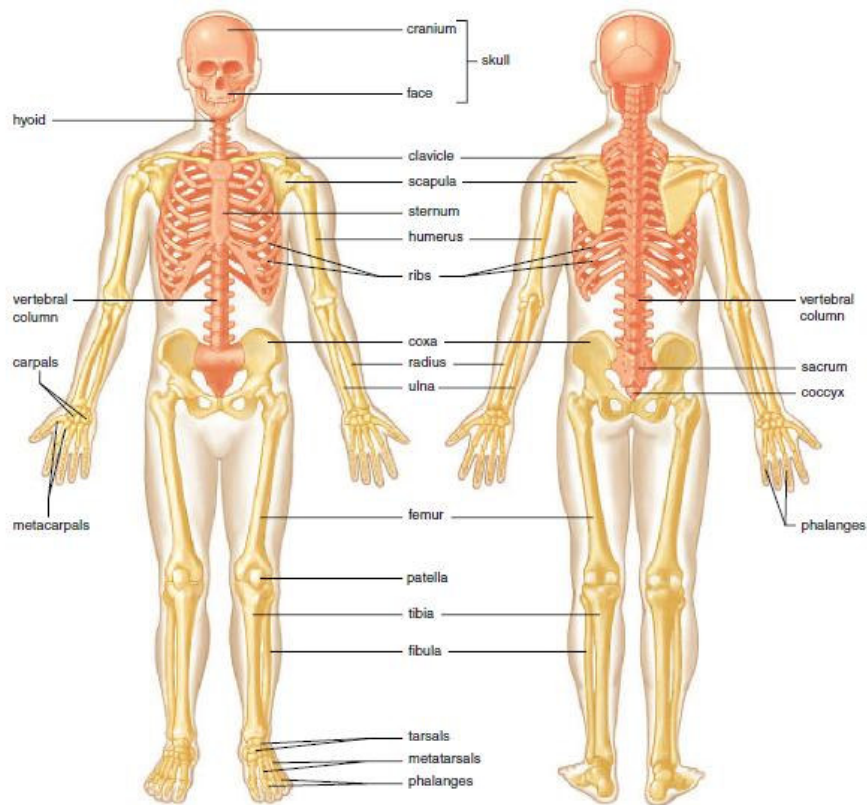


Figure 2.7. Human skeletal system.
(Source: Mader 2005)

2.5. Bone Types in Human Skeletal System

There are five types of bones in the human skeleton. These are long, short, flat, irregular and sesamoid (Figure 2.8.).

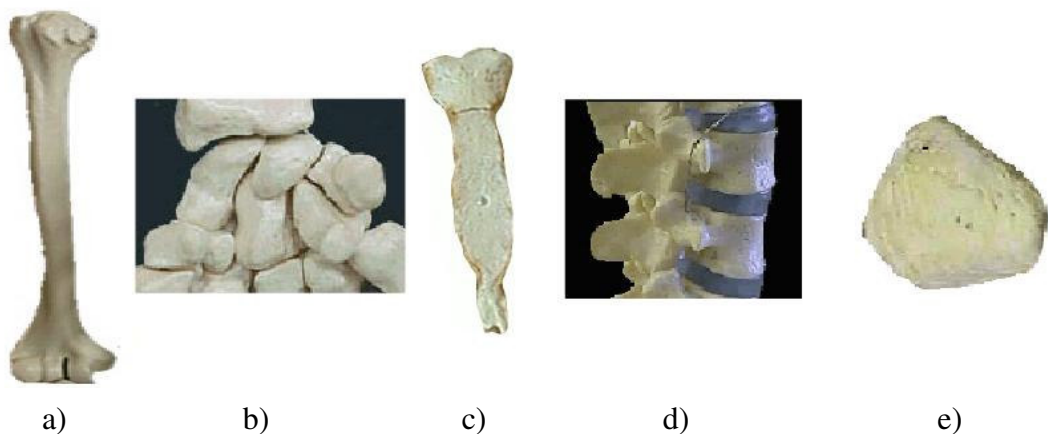


Figure 2.8. Examples of bone types; a) humerus (long bone), b) wrist bones (short bone), c) sternum (flat bone), d) vertebrae (irregular bone), e) patella (sesamoid bone). (Source: British Columbia 2003)

Long bones are characterized by their length. Their length is greater than the width of the bone. They are curved for strength to resist the stresses caused by weight. Long bones possess primarily compact bone in their shafts and spongy bone in their epiphyses. The femur and tibia are well known examples of this type bones.

Short bones are roughly cube-shaped and have a thin layer of compact bone surrounding the interior spongy bone. The bones of wrist and ankle are good examples of short bones.

Flat bones are thin and generally curved with two parallel layers of compact bones sandwiching a layer of spongy bone. They protect soft structures and form sites for muscles attachment. The sternum and bones of skull are the examples of flat bones.

Irregular bones possess complex shapes that do not fit any of the other categories. They consist of thin layers of compact bone surrounding a spongy interior. The bones of the spine and hips are irregular bone types.

Sesamoid bones develop in tendons to protect the tendons from excessive wear and tear. Examples of this type of bones are the patella and the pisiform.

2.6. Vertebral Column (Spine)

The vertebral column extends from the skull to the pelvis. It consists of a series of separate bones, the vertebrae, separated by pads of fibro cartilage called inter vertebral discs (Figure 2.9). The vertebrae column is located in the middorsal region and forms the vertical axis. The skull rests on the superior end of the vertebrae column, which also supports the rib cage and serves as a point of attachment for pelvic girdle. It also protects the spinal cord, which passes through a vertebral canal formed by vertebrae.

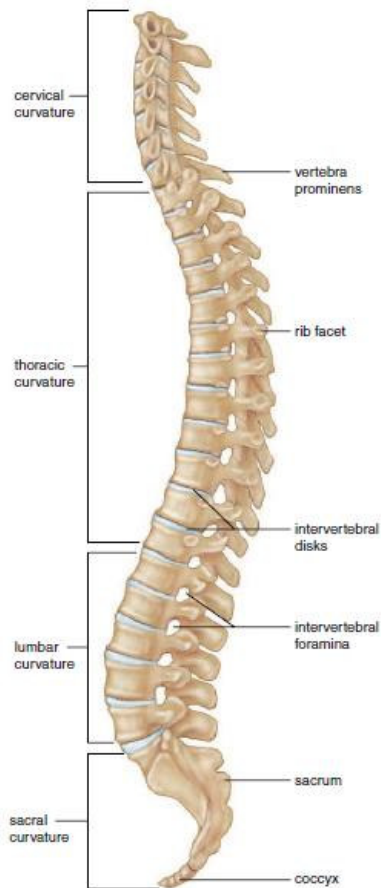


Figure 2.9. Human spine and its regions.
(Source: Mader 2005)

The vertebrae segments are named according to their location. They are labeled from top to the bottom; seven cervical (neck) vertebrae, twelve thoracic (chest) vertebrae, five lumbar (lower back) vertebrae, five sacral vertebrae fused from the sacrum, and three to five coccygeal vertebra fused into one coccyx (tail bone) (Mader 2005).

2.6.1. Intervertebral Discs

The fibriocartilaginous intervertebral discs, located between the vertebra, act as a cushion (Figure 2.10). They prevent the vertebrae from grinding against one another and absorb shock caused by such movements as running, jumping, and walking. The discs also allow the motion between the vertebrae so that a person can bend forward,

backward and from side to side. Unfortunately, these discs become weakened with age and can slip or rupture.

2.6.2. Vertebrae

Figure 2.10 shows a typical vertebra and its sections. Body is anteriorly (front side of body) placed while vertebral arch is posteriorly (back side of body) placed. The vertebral arch forms the wall of the vertebral foramen. The foramen becomes a canal through in which the spinal cord passes.

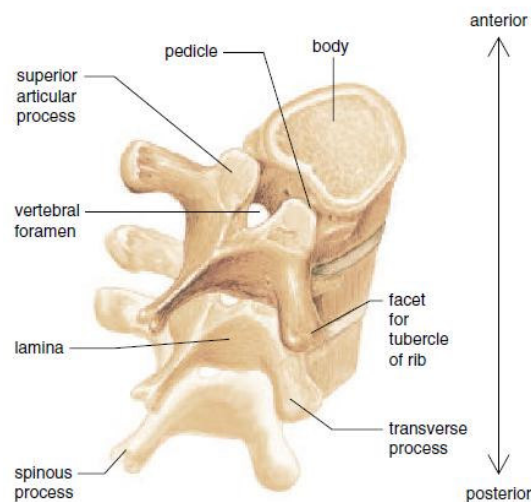


Figure 2.10. Structure of vertebrae.
(Source: Mader 2005)

The vertebral spinous process (spine) exists where two thin plates of bone called laminae meet. A transverse process is located where a pedicle joints the lamina. These processes serve for the attachment of muscles and ligaments. Articular processes serve for joining the vertebrae. Intervertebral discs are placed between the body parts of two vertebrae. Since each vertebra slightly differs from one other, the geometry of intervertebral discs also changes. By increasing body load from top to bottom, intervertebral discs get larger in area to carry more weight.

In the cervical region the spines are short and tend to have a split. The thoracic spines are long, slender and project downward. The lumbar spines are massive, square

and project posteriorly. The transverse processes of thoracic vertebrae have articular facets for connecting the ribs.

2.7. Vertebral Disc Diseases

There are five major disc diseases in the human vertebrae as depicted in Figure 2.11. Vertebral disc diseases result from the thinning or bulging of disc, drying out and collapsing of the disc when it loses its ability to cushion, to act as shock absorber and to prevent grinding against one other. Degenerated disc and thinning disc are natural process of growing older. By aging, inter vertebral discs lose their flexibility, elasticity and the ability of shock absorbing. The ligament tissues surrounding the disc (annulus fibrosis) become brittle and easily torn. Resulting from this, gel-like centre of disc (nucleus pulposus) starts to dry out and shrink. Disc bulging occurs when vertebrae is exposed to shock or some other injury beyond its limits. Resulting from the shock passage, disc protrudes through the out of its normal place pressure to the nerve cord. Herniated disc occurs when small part of the disc's soft, gel-like core is forced through a weak part of the outer disc. Both bulging and herniated discs cause back pain, numbness and tingling (Valentine 2009). Disc degeneration with osteophyte formation is related to any sequential and consequential changes in bone formation due to aging, degeneration, mechanical instability and disease (Rothman, et al. 1982). Calcification and new bone formation can also occur in response to mechanical damage in joints or in the attachment point of ligaments and tendons. This degeneration prevents the natural movements of joints (Nathan 1994)

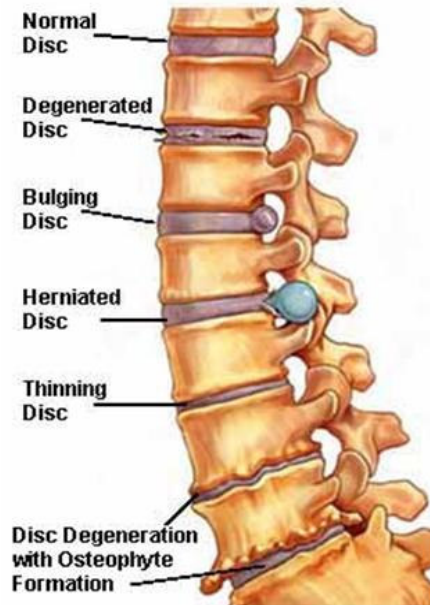


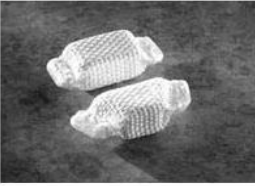





Figure 2.11. Intervertebral disc diseases.
 (Source: Rothman, et al. 1982, Weinstein 1992)

2.8. Spinal Surgery

Spinal surgery term includes healing and/or replacement of degenerated vertebral disc. In disc bulging and herniated disc cases, the problematic sections are removed from vertebral canal. But in higher level degenerations, the disc must be supported with artificial implants. Earlier prosthetic devices had been designed to carry excessive load on the disordered disc surface in case of disc replacements. Their major aim was to carry the load so the fixation of the prosthesis was taken into account in former spinal disc replacement implants. Table 2.1 tabulates some earlier vertebral disc devices.

To overcome the disadvantages of former spinal disc replacement devices, spinal cages have been designed and still the most commonly used devices in spinal surgery. They are filled with bone graft and inserted into the empty space created by a discectomy (disc removal) (Figure 2.12) and very similar to a tiny birdcage. Bone graft is packed around the cage following the implantation. Like instrumentation and fusion, the bone graft grows into and around the cage and creates a stable construct. Since, bone graft is surrounded with a hard solid material, the implant loosening is frequently observed in post surgery period.

Table 2.2. Spinal disc replacement devices.

| Spinal Disc Device | Property |
|---|--|
|  | <p>Hydrogel disc replacements primarily have hydraulic properties. Hydrogel prostheses are used to replace the nucleus while retaining the annulus fibrosis.</p> |
| <p>PDN Prosthetic Disc Nucleus</p> | |
|  | <p>Acroflex disc consisted of a hexene-based polyolefin rubber core vulcanized to two titanium endplates.</p> |
| <p>Acroflex Disc</p> | |
|  | <p>Articulating Discs designed with a polyethylene core and metal end plates. The metal endplates have two vertical wings and the surfaces which contact the endplates are plasma-sprayed with titanium.</p> |
| <p>Articulating Discs</p> | |
|  | <p>The Charité consists of a biconvex ultra high molecular weight polyethylene spacer. This core spacer interfaces with two separate endplates which are made of casted cobalt-chromium-molybdenum alloy, each with three ventral and dorsal teeth.</p> |
| <p>Link SB Charité Disc</p> | |
|  | <p>The Bristol Disc is a ball and socket type device constructed of stainless steel. It is secured to the vertebral bodies with screws</p> |
| <p>The Bristol Disc</p> | |
|  | <p>The Bryan Cervical Disc is designed based on a proprietary, low friction, wear resistant, elastic nucleus. This nucleus is located between and articulates with anatomically shaped titanium plates (shells) that are fitted to the vertebral body endplates.</p> |
| <p>Bryan Cervical Disc Prosthesis</p> | |

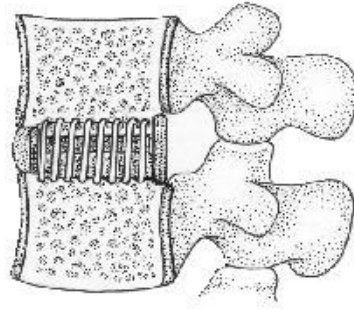


Figure 2.12. Interbody spinal cage implantation.
(Source: Eidelson 2002)

Currently, there are numbers of available interbody fusion devices made from different materials with various shapes in the market and Table 2.2 lists the currently used spinal cages in spinal surgery. The devices listed in Table 2.2 are designed to meet the mechanical requirements of posterior lumbar interbody fusion and uses autologous cancellous bone. However, the moduli of elasticity of the used materials are far greater than that of human cortical bone; therefore, stress shielding leading to the implant loosening may easily occur.

Table 2.3. Spinal cages for bone ingrowth.

| Spinal Disc Device | Property |
|---|---|
|  <p data-bbox="354 568 564 602">BAK, Spine-Tech</p> | Cylindrical threaded Ti6Al4V interbody cage. |
|  <p data-bbox="408 824 504 857">Inter Fix</p> | Cylindrical threaded cortical bone dowel. |
|  <p data-bbox="360 1077 552 1111">MD11 and MDIV</p> | Vertical interbody rings or boxes. |
|  <p data-bbox="379 1339 536 1373">KIMBA Cage</p> | KIMBA Cage is made of ECF PEEK-OPTIMA® polymer with icotec's Composite Flow Molding process. |
|  <p data-bbox="296 1615 616 1648">JAGUAR Lumbar I/F CAGE</p> | The JAGUAR Lumbar I/F CAGE System is a carbon fiber reinforced polymer implant designed to separate the mechanical and biologic functions of posterior lumbar interbody fusion. |

CHAPTER 3

POROUS BIOMATERIALS: MANUFACTURING AND BONE INGROWTH PROPERTIES

3.1. Bone Ingrowth into Porous Implants

The use of porous coated orthopedic implants and complete or semi porous bone substitutes aims at increasing implant bone ingrowth performance. The employment of porous orthopedic implants involves initial penetration of undifferentiated mesenchymal cells (mesenchymal cells are multipotent stem cells that can differentiate osteoblasts, chondrocytes, myocytes, adipocytes) (Chen, et al. 2004) into porous spaces followed by the formation of woven new bone in the intramembranous pathway and bone remodeling process. Major parameters of formation of new bone include implant material-bone apposition, viability of the surrounding bone and the stability of the porous implant-bone interface. Porosity level, pore size and the implant material have significant effects on the porous implant performance (Itala, et al. 2001).

In order to achieve bone ingrowth (osseointegration) into porous implant surface and inner pores, the implant must have adequate porosity. The percentage of porosity needed for bone ingrowth has been reported to be ranging between 35 to 70%. Cook et al. showed the bone ingrowth of 35 to 40% porous implants implanted to mongrel dogs (Cook, et al. 1985). Sumner and Turner showed the bone formation in 50% porous Ti implants made of wires (Sumner, et al. 1990, Turner, et al. 1989). Cameron and Pillar investigated the rate of bone growth in 65% dense cobalt based implants (Cameron 1976). Hulbert reported ingrowth of natural bone in a 65% porous ceramic matrix (Hulbert 1970). Hofmann showed human cancellous bone ingrowth into 55% Ti6Al4V core and Ti coated implants (Hofmann, et al. 1997). The recent successful investigations of the patented ActiPore by a research group in Ste-Justine Hospital and Biorthex have shown the rapid bone formation in 65±5% porous TiN(Nitinol) implants (Likibi, et al. 2004).

Research has also been performed to determine optimum parameters of the bone formation in porous implant surfaces. Few investigations were also on the effect of interconnected pore size (Hulbert 1970, Cameron, et al. 1976, Boby, et al. 1980, Martens, et al. 1980, Clemow, et al. 1981, Boby, et al. 1982, Cook, et al. 1985, Schliephake, et al. 1991, Bloebaum, et al. 1994, Hofmann, et al. 1997).

Experimental results based on the animal implantation using porous materials have shown that the pore sizes affected bone ingrowth. In an investigation performed by Boby, Pillar, Cameron and Weatherly, bone growth was observed into porous surface down to 50 μ m pore size and a porous cobalt based porous implant with pore size ranging between 50 and 400 μ m reached the maximum fixation strength after 8 weeks of implantation (Boby, et al. 1980). On the contrary, Hulbert et al reported that the minimum pore size must have been between 75 and 100 μ m to regenerate significant level of mineralized natural bone (Hulbert 1970). Russian researchers Melikyan and Itin implanted sintered porous titanium specimens of 100-300 μ m in pore size to rabbits and reported successful growth of bone tissue in to the implant (Melikyan and Itin 2002). In another study on rabbits by E. Barth et al., an optimum pore size of 400 μ m was found for bone ingrowth (Barth, et al. 1986). A Japanese research group reported the optimum pore size for growth of osteoblasts and vascularization was approximately in the range of 300-400 μ m. This result was obtained by implanting 106-212, 212-300, 300-400, 400-500 and 500-600 μ m pore size hydroxyapatites implants to rats (Tsuruga, et al. 1997). An American research group declared the similar results for optimum size of pores by expanding the limits of pores size, 200-500 μ m and implanting porous surface coated Ti6Al4V specimens into the femoral medullary canal of dogs for six months (Clemow, et al. 1981). Boby et al. showed that higher bone and implant interlocking strength occurred when porous tantalum implants with averaging 430 μ m and 650 μ m had employed instead of other porous materials with less volumetric pore size (Boby, et al. 1999).

Conversely, when the pore size increased to 1mm, the formation of fibrous tissue was found to increase (Itala, et al. 2001). Cameron, Pillar and Macnab reported a gap of 1.5 mm between the bone and the implant was bridged by new bone within four weeks.

Several different porous implants are currently in the market and used in the implantation. Part of them is the solid implant coated with a porous layer on the surface (Plasma Spray Coating by Biomet, CoCr Beads by Howmedics, Osteonics, J&J, Depuy, and Ti Fiber Mesh by Zimmer). Novel porous implants are however made of complete

porous structure. Trabecular Metal produced by Zimmer, CSTi produced by Centerpulse and Nitinol (TiNi) produced by Biorthex offer higher bone ingrowth proved by the clinical observations. Among them a spinal product called ActiPore which made of TiNi and produced by Biorthex has the best clinical results proven by the several scientific investigations (Prymak, et al. 2005, Assad, et al. 2003 Assad, et al. 2003, Rhalmi, et al. 1999). Comparative studies with two types of metallic lumbar fusion implants, ungrafted porous nitinol with 230 ± 130 μm pore size and $\%65\pm 5$ porosity and hollow threaded Ti6Al4V fusion cage with iliac crest bone chips (Figure 3.1) showed the superiority of the porous implant to the conventional cages. Both devices were implanted to sheep lumbar region in order to evaluate bridging osseointegration, and structural change induced in the peripheral tissue mass after 3, 6, and 12 months post-implantation. Table 3.1 tabulates the comparative clinical results of porous nitinol and typical conventional spinal fusion device.

Table 3.1. The comparison of bone fusion over post-surgery recovery time.
(Source: Likibi, et al. 2004)

| | 3 months | 6 months | 12 months | Total |
|-------------|----------|----------|-----------|-------|
| ActiPore | 5/6 | 6/6 | 4/4 | 15/16 |
| Spinal Cage | 1/6 | 0/6 | 3/4 | 4/16 |

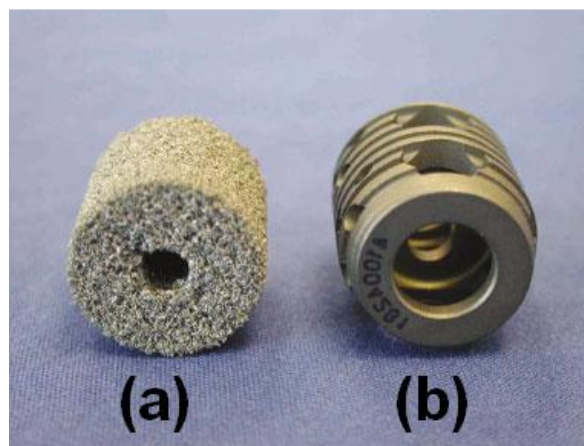


Figure 3.1. Photography of a) Biorthex - ActiPore interbody fusion device with 230 ± 130 μm pores, $65\pm 5\%$ porosity in $\text{Ø}11\times 22$ mm dimensions, b) Sulzer – BAK hollow threaded Ti6Al4V fusion cage in $\text{Ø}11\times 22$ mm dimensions. (Source: Assad, et al. 2003)

Table 3.1 proves the early bone formation in porous implants. Open interconnected pore matrix allowed new bone formation much earlier than the fusion cage implant. This early formation resulted in better fixation of implant in post surgery period. Assad et al. analyzed the bone formation progression in both porous and fusion cages. Figure 3.2 shows the bone formation progression in these spinal lumbar devices. Blue sections in the microscopic images in Figure 3.2 show fibrous tissue formation. The fibrous tissue formation near the implant-bone contact area was higher in spinal cage. This study also proves the hypothesis of tendency to formation of fibrous tissue on smooth surfaced implant and fractured bone contact area. Since porous implants had rough surface, the tendency of fibrous tissue formations was limited in early stage of implantation and after 12 months all pores were filled with bone. Preventing fibrous tissue formation parallel to the implant surface resulted in better fixation and much lower possibility of implant loosening.

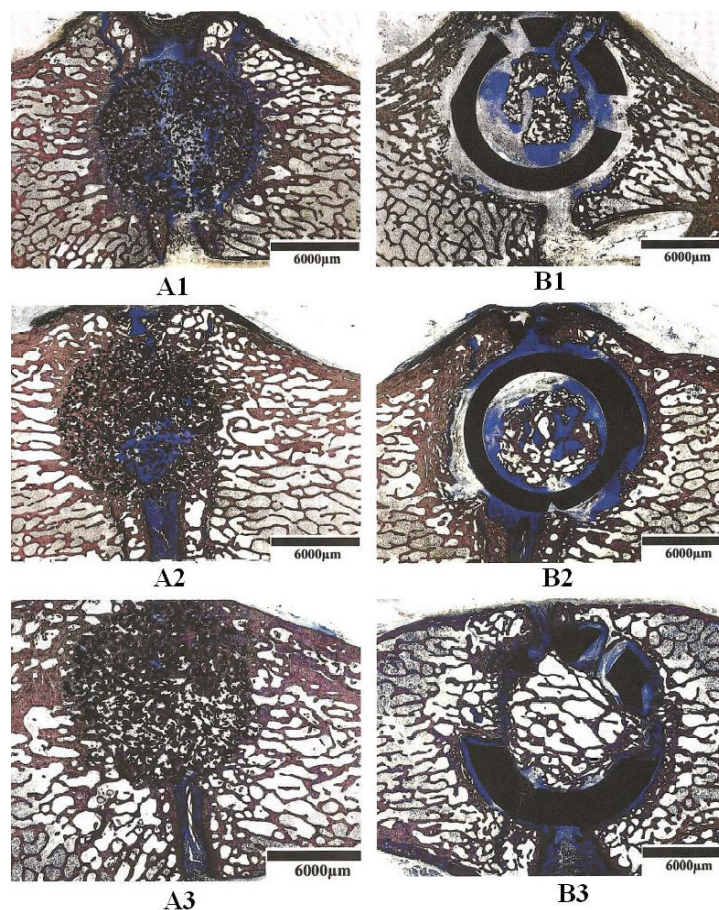


Figure 3.2. Light-microscope micrographs of porous a) ActiPore sample, b) BAK Spinal Cage sample transverse section over post surgery recovery time: 1) 3 months, 2) 6 months, and 3) 12 months. (Source: Assad, et al. 2003)

Figure 3.3 shows macro images of implant material-bone contact surface and soft tissue formation in early stages of the healing. Orientations of fibrous tissues were parallel to the spinal cage surface, while they were perpendicular to the porous implant surface. The perpendicular orientation of fibrous tissues resulted in better fixation.



Figure 3.3. Soft tissue fiber orientation in the presence of porous a) spinal device, b) solid spinal cage at 3 months of post-instrumentation. (Black lines designate implant surface and white lines designates fiber orientation.) (Source: Likibi, et al. 2004)

3.2. Fabrication Methods of Porous Metals

In the past, stability of implants was primarily achieved using screws and bone cement. However, more recently improved fixation can be achieved by bone tissue growing into and through the porous matrix of metal. This effect bonds the implant to the host bone. Another potentially valuable property of porous materials is their low elastic modulus. Besides controlling the optimum body fluid transportation and bone growth parameters, the elastic moduli can even be tolerated to match the modulus of bone closer than solid metals. Modulated elastic modulus reduces the problems associated with stress shielding (Robertson, et al. 1976, Head, et al. 1995).

Although the use of porous metals in orthopedic implantations was considered relatively a new approach, the fabrication of porous structures have been actively searched since 1943 when the B. Sosnik attempted to introduce pores into aluminum by adding mercury (Simancik 2002). One of the earliest attempts of biomedical application of porous metals was conducted by Weber and White in 1972 (Ryan, et al. 2006). In early of 70's, numerous investigations on porous materials of ceramics (Eugene, et al.

1975), polymers (Spector, et al. 1978, Klawitter, et al. 1976, Cestero, et al. 1975, Sauer et al. 1974) and metals (Hirschhorn 1971, Galante, et al. 1971, Hahn 1970) were performed. Despite excellent corrosion resistance, porous ceramic structures cannot be employed in load bearing instrumentation due to their intrinsic brittleness. Likewise, porous polymeric materials cannot sustain the mechanical forces in orthopedic surgery. These limitations led the researchers to focus on porous metals. Metals have superior fracture and fatigue resistance besides their moderate corrosion resistance.

Major classifications of the metallic porous structures are open-cell and closed-cell foams. In open-cell structure, individual cells are interconnected while in closed-cell foam structure, each pore is completely enclosed by a thin wall. The fabrication methods of open and closed-cell foams are listed in Table 3.2. Closed-cell foams are usually formed by a random foaming process, in which the size, shape and localization of pores depend on the fabrication parameters.

Table 3.2. The fabrication methods of metallic porous structures and classifications based on the resulting pores structure.

| Fabrication Methods | | | | |
|---|-----------------------------|--|--|---|
| Closed-cell | | Open-cell | | |
| Random Pore Size | Graded Pore Size | Non-Homogenous | Homogeneous | Functionally Graded |
| Gas injection into the metal melts (Korner and Singer 2000) | Plasma spraying (Hahn 1970) | Sintered metal powders (Oh, et al. 2003) | Orderly oriented wire mesh (Ducheyne and Martens 1986) | Rapid prototyping (Thieme, et al. 2001) |
| Decomposition of foaming agents (Banhart 2001) | | Sintered metal fibers (Martell, et al. 1993) | Vapor deposition (Bobyne, et al. 1999) | Electro discharge compaction (Okazaki, et al. 1991) |
| | | Space holder method (Bram, et al. 2000) | Ferromagnetic fiber array (Markaki and Trevor 2005) | |
| | | Replication (Li, et al. 2002) | Rapid prototyping (Thieme, et al. 2001) | |
| | | Combustion synthesis (Li, et al. 2000) | | |
| | | Plasma spraying (Hahn 1970) | | |

3.2.1. Fabrication Techniques for Closed-Cell Porous Metals

Closed-cell foams are mostly employed in load bearing applications. In particular, the lowered structural stiffness brought about by the introduction of voids allows the reduction of their bulk stiffness. At the present, there are numbers of methods used to process closed-cell foams. It is possible to summarize them in two general routes; forming the foam from a melt and powder metallurgy. In melting process, self foaming structures are manufactured either by gas injection through the melt (Cymat / Hydro) (Figure 3.4), or by the addition of gas forming elements into the liquid metal (Alporas) (Figure 3.5) (Korner and Singer 2000). These methods have been generally used for fabrication of Al, Zn and Mg foams. In powder metallurgy techniques, foam structures are obtained either by sintering hollow spheres or by melting of powder compacts that contain a gas blowing agent such as TiH_2 (Alulight / Foaminal) showed in Figure 3.6 (Banhart 2001). This technique has been known to yield a relative homogenous structure and enables fabrication of foam of high melting temperature metals and alloys. Fatigue strength of the resulting foam can be modified by changing the mixing strategy.

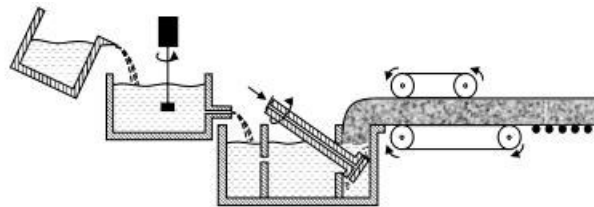


Figure 3.4. The foam casting process employed by CYMAT; the process is composed of melting and holding furnaces, the foaming box, and foaming equipment, and a twin-belt caster. (Source: Korner and Singer 2000)

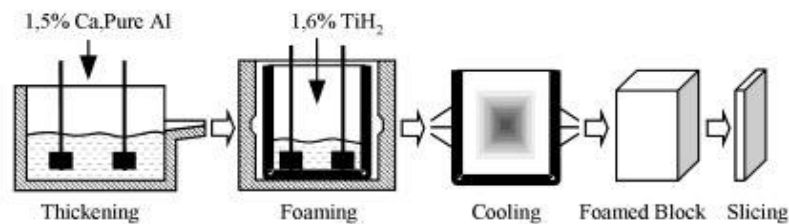


Figure 3.5. ALPORAS foam processing
(Source: Korner and Singer 2000)

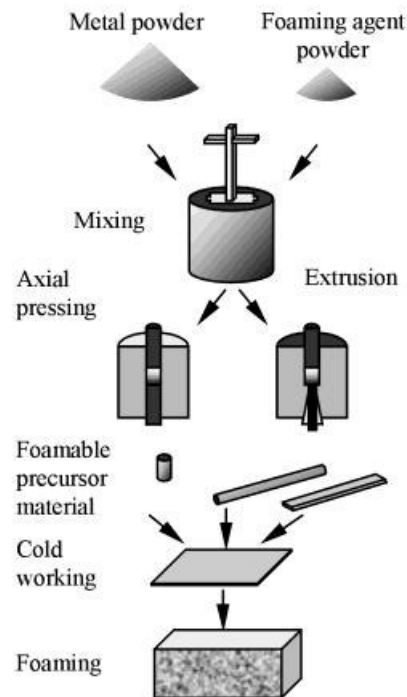


Figure 3.6. ALULIGHT and FOAMINAL foam processing.
 (Source: Korner and Singer 2000)

A Common technique employed for producing porous structures or porous coatings is the plasma spraying (Hahn 1970). This method can be used for fabrication of rough solid surface textures, porous surface coatings on solid cores and fully porous structures. A schematic description of plasma spraying process is shown in Figure 3.7. An electric arc is generated between two water-cooled electrodes in a gun. The arc heats the gas up to 20,000 °C, partially ionizing it and forming a plasma jet. This plasma jet is used as carrier and the powder of metal for the coating is injected into the plasma stream. Porous structure with varying degrees of porosity can be created on the substrate by adjusting the spraying parameters. Hahn and Palich first described titanium plasma-sprayed coatings for fabrication of porous coating implants (Hahn 1970). This process generally results in irregular pores and lower pore densities, but allows the processing graded materials with a denser core and more porous outer shell.

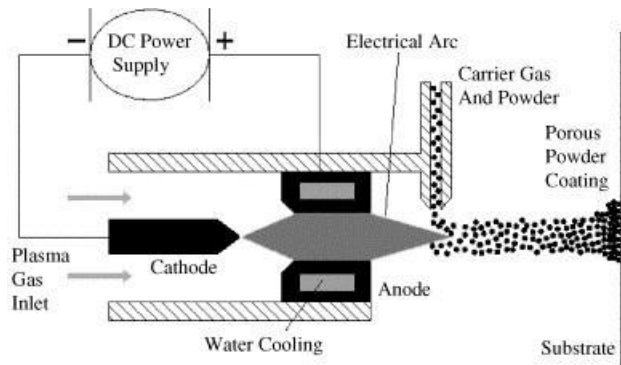


Figure 3.7. Schematic of plasma spraying process.
(Source: Ryan, et al. 2006)

3.2.2. Fabrication Techniques for Open-Cell Porous Metals

Open-cell foams are used for functional purposes. The main groups include non-homogeneous, homogenous and functionally graded open-cell pores.

3.2.2.1. Non-Homogeneous Pore Distribution

3.2.2.1.1. Sintering Metal Powders and Fibers

Simplest fabrication method for non-homogenous open cell structures is the sintering of metal powders or fibers. This technique is based on powder metallurgy, which is a mature metal forming technology used in the fabrication of both porous coated and fully porous metallic implants. In this method, metal powder is packed in a mold. A binder material is often added for efficient packing of the particles and also for holding the particles together. The resultant green compact is finally sintered in an atmosphere controlled or vacuum furnace. The porosity level is limited but it can be controlled modifying compact powder density and sintering temperature and time. For spherical powders, the final porosity is limited to 50% percent. The pores results from the empty spaces between the powder particles and they are irregular. Examples of powder sintering porous structures include Co-Cr alloy (Cook, et al. 1985), commercially available pure Ti (Oh et al. 2003), Ti6Al4V alloy (Clemow, et al. 1981), and NiTi (Rhalmi, et al. 1999). The powder size used is ranged between 50 μm and

1mm. The porosity level of porous structure, formed by fiber sintering, is limited to 30-50% (Galante and Rostoker 1973).

3.2.2.1.2. Space Holder Method

The space holder method is a fabrication method similar to the fabrication of powder compacts. Space holder method however allows fabrication of highly porous structures. Figure 3.8 shows the fabrication routes of space holder method. The routes include mixing, compaction and sintering stages as in the case of powder compact sintering. At an intermediate stage, the space holder is removed before the sintering of the powder compact at a high temperature. An ideal space holder material should be completely decomposed relatively low temperatures. It should also be noted that the size of the metal powder should be smaller than the average powder size of space holder material. Main pores are formed in the area left by the space holder material. The smaller pores are found in between the metal particles. This method provides a foamed structure with a close to homogenous pore structure and high levels of porosity up to 70-80% (Wen, et al. 2002).

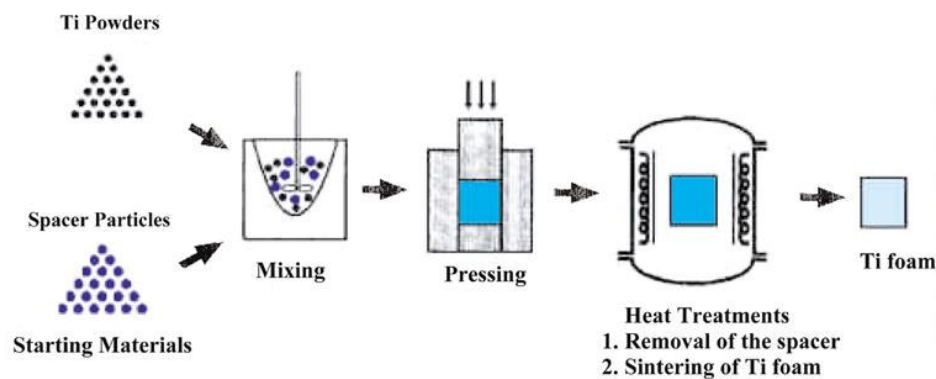


Figure 3.8. Schematic of biocompatible porous Ti foam processing using space holder. (Source: Wen, Yamada et al. 2002)

3.2.2.1.3. Replication

This process includes pattern preparation, infiltration and pattern removal steps as depicted in Figure 3.9. The method enables production of highly porous structures. Li et al. utilized this method to produce porous titanium and titanium alloy structures (Li,

et al. 2002). Three types of pores are found in these foams, in order to increase size primary porosity at the surface of hollow struts, secondary porosity at the core of the hollow struts previously occupied by pattern material and open tertiary porosity between struts. It is possible to produce materials up to 80% porosity using this method.

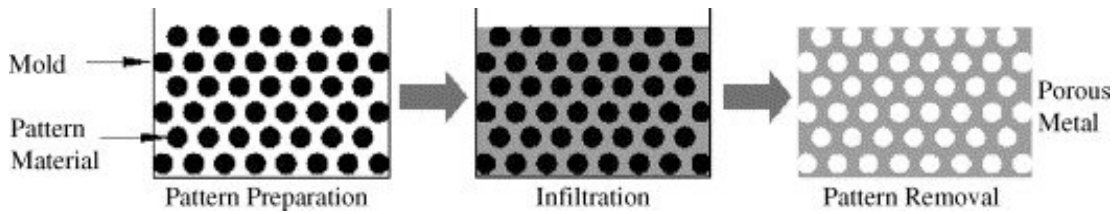


Figure 3.9. Schematic of three steps of replication method of foam processing (Source: Ryan, et al. 2006)

3.2.2.1.4. Combustion Synthesis

Combustion synthesis is becoming popular for the production of high purity, porous alloys in particular nickel titanium alloys. In this method, particle fusion is obtained through an extremely rapid self-sustained exothermic reaction driven by the large heat released in the synthesis (Figure 3.10). The reactants in the form of powders are dry mixed and cold pressed. The reaction can then be started under two different regimes. These regimes are thermal explosion in which the reactants are gradually heated until reactions take place simultaneously throughout whole sample and self-propagating high thermal synthesis step which is pre-ignited spreading exothermic reactions.

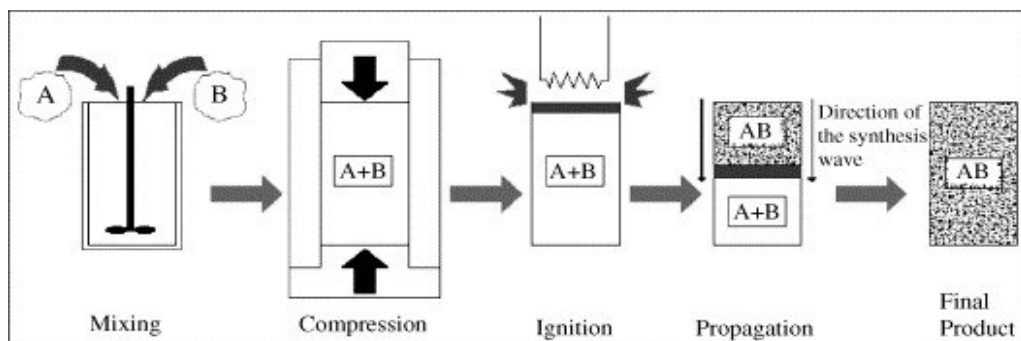


Figure 3.10 Schematic of combustion synthesis process. (Source: Ryan, et al. 2006)

3.2.2.2. Homogeneous Pore Distribution

3.2.2.2.1. Orderly Oriented Wire Mesh

Orderly oriented wire mesh coatings were first presented by P. Ducheynea and M. Martensb in 1985 (Ducheyne and Martens 1986). This coating technique is used to form large, uniform pore sizes for tissue ingrowth. Mesh wire sintering technique is very much similar to the fiber metal sintering as both of them made of small-diameter metal fibers. Main difference is rather than cutting the wires to short lengths for compaction in dies, the continuous wire lengths are woven into a regular meshwork and sintered under pressure. Wire thickness and geometrical orientation of the wires determine the porosity level and pore size.

3.2.2.2.2. Vapor Deposition

This is a relatively recent technique and used for the processing metallic materials with porosity up to 75-85% volume fractions. Well known example is the Trabecular Metal, a patented product of Zimmer biomedical company. Fabrication technique is generally labeled as chemical vapor deposition and involves depositing a solid material on a substrate (i.e. medical grade polyurethane foam) by activating the reactants in the gaseous phase where they react chemically (Figure 3.11).

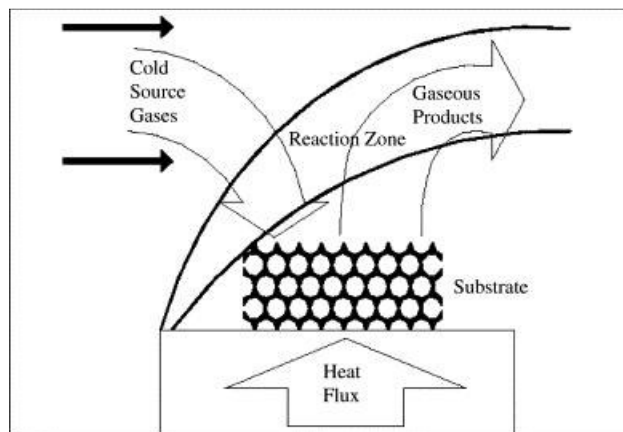


Figure 3.11. Schematic of chemical vapor deposition process which involves the use of an intermediate reticulated vitreous carbon substrate. (Source: Ryan, et al. 2006)

3.2.2.2.3. Ferromagnetic Fiber Array

Markaki et al. developed a new production method for porous orthopedic implant materials. It was suggested that bone growth could be stimulated in vivo by magneto-mechanical mechanism that involves the transmission of stresses and strains to growing bone with small local deflections within a porous ferromagnetic material. For the bone ingrowth, the strain level of at least 0.1% is required. Utilizing this fact, the implant surface was coated with an outer layer of highly porous ferromagnetic biocompatible stainless steel fibers. By the application of the magnetic field, the surface of the implant is deformed elastically as result of the ferromagnetic fiber alignment in the magnetic field as depicted in Figure 3.12 (Markaki and Trevor 2005).

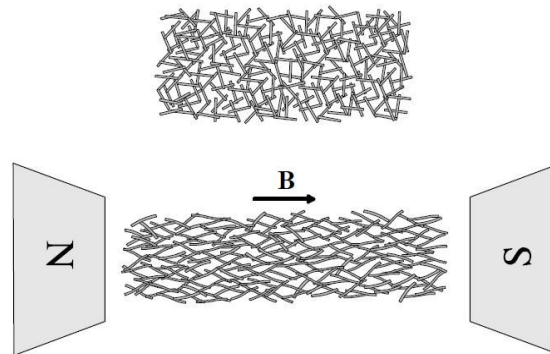


Figure 3.12. Schematic representation of a bonded array of randomly-oriented magnetic fibers deformation in a magnetic field. (Source: Markaki and Traver 2005)

3.2.2.2.4. Rapid Prototyping

This process is one of the novel fabrication methods. It is based on the technique of three dimensional printing. It allows manufacturing porous structures with precise control of size, shape and distribution of pores. Figure 3.13 shows the basics of three-dimensional printing technique. Three dimensional printing can be beneficial in the fabrication of prototypes. This method can produce filler structures with high accuracy for the fabrication of porous metals. Parts or objects are created in a cavity that contains a powder bed support by the moving piston. Each layer is filled with an object material. The process continues with a heat treatment (sintering) to bond the particles.

Since rapid prototyping method allows precise control of parameters, both homogeneous and functionally graded porous material can be fabricated using this method. However it is an expensive method for fabricating high quantities.

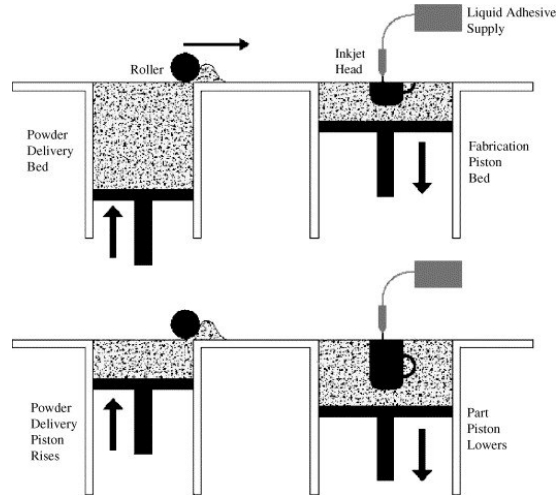


Figure 3.13. Schematic of three dimensional printing (sintering) process.
(Source: Ryan, et al. 2006)

3.2.2.3. Functionally Graded Pore Distribution

3.2.2.3.1. Electro Discharge Compaction

This method is also known as electrical field-assisted powder consolidation, since the application of an external current assists the powder consolidation. Some patented applications of this technique are filed assisted consolidation technique (FAST), spark plasma sintering (SPS), plasma activated sintering (PAS) and electrical discharge compaction (EDC). Common to all, an electrical discharge with rapid heating and pressure are used to achieve fast sintering of metal powders. Figure 3.26 shows the schematic of FAST process. The process is simple, based on the uniaxial compression, applying pulsed and steady currents in a vacuum or gas controlled environment.

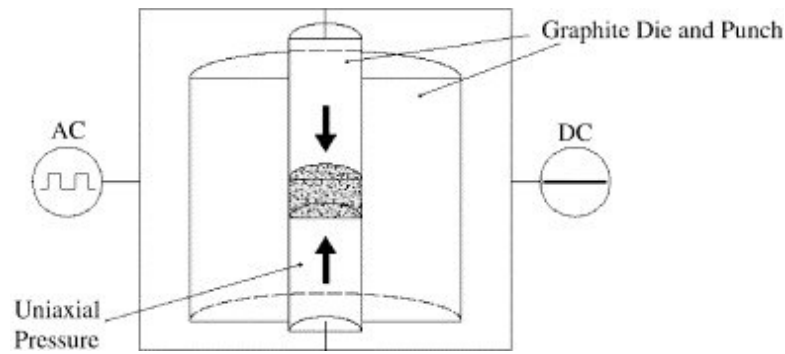


Figure 3.14. Schematic of FAST process.
(Source: Ryan, et al. 2006)

3.3. Processing of Ti and Ti6Al4V Foams

A major problem of conventional implant metals is the elastic mismatch with bone. The elastic moduli of biomedical implants in the market are tabulated in Table 3.3. Ti and Ti6Al4V have elastic moduli lower than other bio-metals but higher than that of bone.

Table 3.3. Comparison of Elastic moduli of metallic implant materials with human cortical bone (in GPA)

| Ti, annealed | Ti6Al4V, Annealed | Co29Cr5Mo, Cast | Stainless steel ASTM 316L | Cortical bone |
|--------------|-------------------|-----------------|---------------------------|---------------|
| 112 | 115 | 200 | 210 | 1-20 |

One of the disadvantages of Ti is the chemical affinity with the atmospheric gases such as oxygen and nitrogen. This makes Ti difficult to process at high temperatures. Titanium and titanium based alloy are therefore requires special forming process. Casting of bulk titanium objects requires high-vacuum and high-temperature processing. As a result, titanium and titanium alloy foaming processes are limited to powder metallurgy manufacturing methods. Utilization of powder metallurgy enables production of bulk titanium objects at much lower temperatures and under less stringent chemical reactivity constraints.

In Figure 3.15 the main solid state fabrication processes available for fabrication Ti and Ti6Al4V foams are shown. These processes are summarized in the next sections.

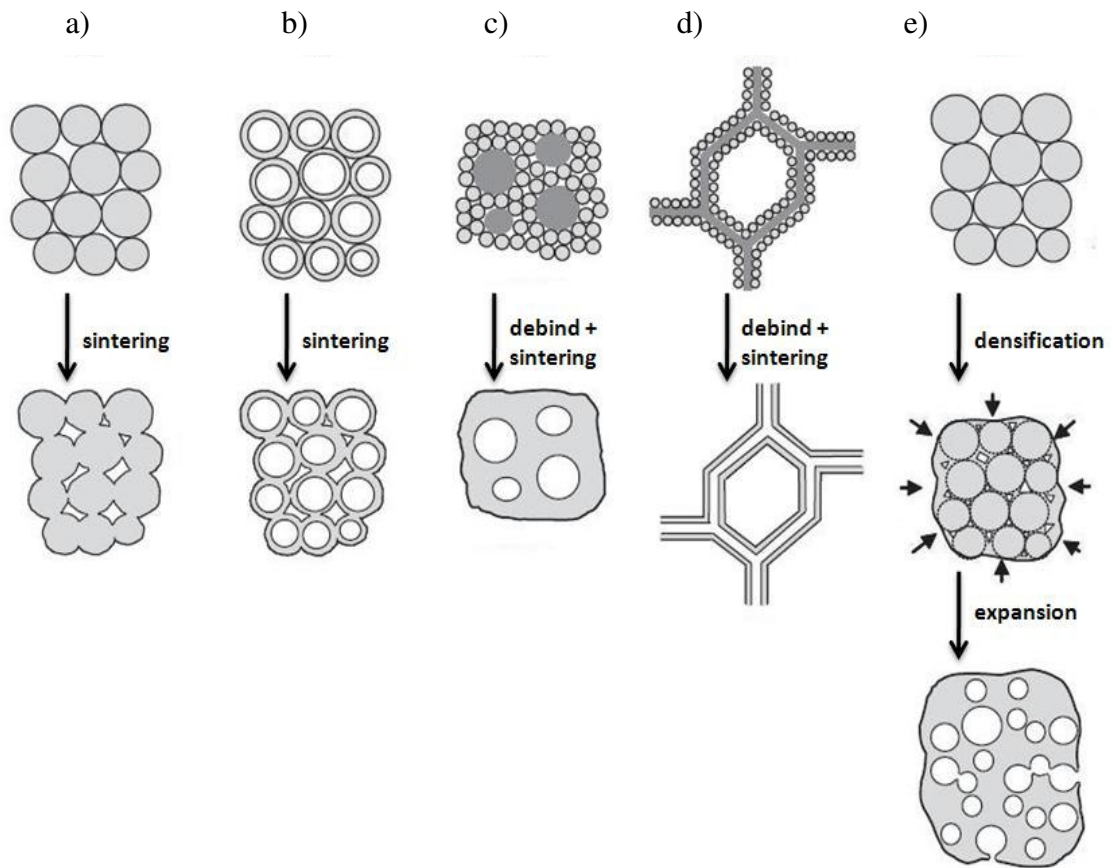


Figure 3.15. Schematic of solid-state processing of Ti and Ti6Al4V foams; a) powder compact sintering, b) hollow sphere sintering, c) space holder method, d) sintering of powders deposited on scaffold, e) powder densification in presence of gas, and expansion of trap.

3.3.1. Sintering of Powder Compacts.

Sintering of powder compacts is the simplest technique of foam processing. It is based on the partial sintering of porous perform of powders. Cirincione et al. investigated the compressive strength of sintered Ti6Al4V powder compacts sintered at 1000 ° C from 0.5 to 24 hours (Dunand 2004). The final densities attained were reported to be between 41 and 55% and a compressive strength of 55MPa for 49% porous foam. Oh et al. investigated sintered Ti powder compacts with a porosity range of 5-37%. Young modulus and compressive strength was found to decrease linearly with increasing porosity. 30% porous Ti compacts were found to have elastic modulus and bending strength close to those of human cortical bone. Thieme et al. investigated spherical titanium powder compact sintering with the particle size between 180 and 1000 μm (Thieme, et al. 2001). Sintering was performed at temperatures between 1150-

1500 °C with 1 to 6 h sintering durations in a high vacuum furnace. The resultant compacts were reported to have elastic moduli of 5-35 GPa and porosity levels of 35-60%. Quasi-static and high strain rate compression behavior of sintered Ti6Al4V powder compacts was investigated (Guden, et al. 2005). Cold compacted powders in a range of 74 to 250 μm satisfying ASTM-1 1580-1 standard were sintered at 1200°C for 2 h under argon gas atmosphere. The compressive strength of the compacts with 37±1% porosity and 63 μm pores size was found to increase from 240MPa at quasi-static to 300MPa at high strain rates. By utilization spark plasma sintering, Kon, Hirakata and Assaoka fabricated CP-Ti and Ti6Al4V foams with mean porosity of 30%. The method allowed lower sintering temperature (560-700°C) and times (3-20min) at relatively high pressures (20-30MPa). Ti and Ti6Al4V foams produced using this method, were reported to have compressive strengths of 233±11 MPa and 113±8 MPa, respectively. The limitation of the powder sintering approach is that pore size and shape are dictated by titanium powder size and shape. For spherical powders, the porosity is limited to at most 50% and shape of the pores is highly non-spherical.

3.3.2. Hollow Sphere Sintering

The pores in this method are resulted from the inner space of the porous powders and as well as the space between the powders due to partial sintering (Augustin and Hungerbach 2009). The method is composed of two steps. In the first the hollow spheres are formed (Figure 3.16). In the second, the hollow spheres are sintered (Figure 3.17). In hollow sphere processing, polystyrene spheres are placed into a mixing device and then and Ti6Al4V powders with a binder solution were sprayed on the polystyrene spheres. After that green spheres coated with powder are heat treated to remove polystyrene core. In the second stage, the resulting spheres are molded and sintered at relatively high temperature (Augustin and Hungerbach 2009). In this method, the final porosity may increase to %85.

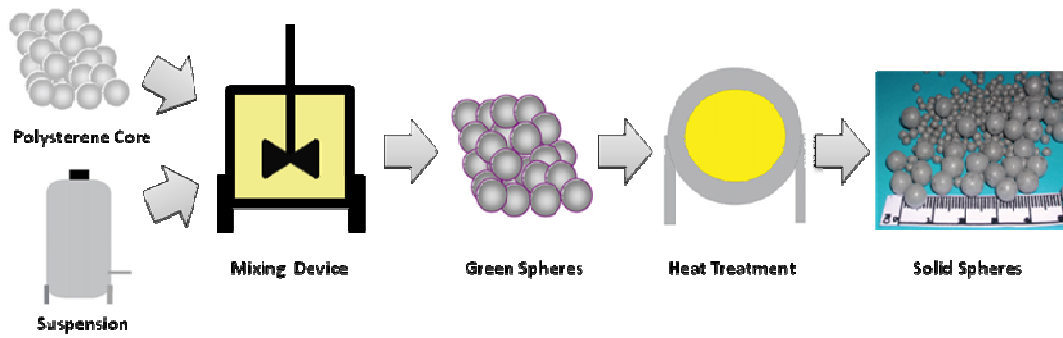


Figure 3.16. Schematic of solid hollow sphere processing.

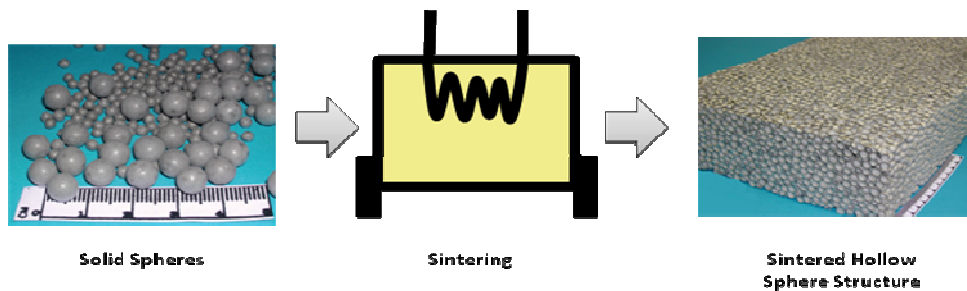


Figure 3.17. Sintering of hollow sphere structures.

3.3.3. Space Holder Method

The use space holding particles results in the formation of secondary pores in the structure and increases porosity dramatically. Space holder is a solid material which can be removed usually at low temperature without excessive contamination of titanium particles. The major steps of the space holder method is shown in Figure 3.18 and composed of mixing, pressing and heat treatment steps. The mixture of Titanium and space-holder powder is pressed to impart enough green strength to prevent collapse upon removal of space holder and in the subsequent sintering process. Adding a binder material also increases the stability of green compacts.

Wheeler et al. used magnesium powders as a space holding material in Ti and Ti6Al4V foam processing. The space holder was removed at 1000 °C and the Ti compacts subsequently were sintered at 1400 °C (Nilles, et al. 1974). Bram et al. and Wen et al. successfully processed Ti foams using ammonium hydrogen carbonate and carbamide particles as spacer holding materials in a size range of 200 and 600 μm. Green samples were heat treated at 200 °C for 5h and sintered at 1200 °C for 2h (Bram, et al. 2000, Wen et al. 2001). Laptew et al. also used ammonium bi carbonate for

manufacturing of highly porous titanium parts since it decomposes by heating below the 200 °C with no risk of deterioration of titanium (Laptev, et al. 2004).

The most important advantage of the space holder method is the close control of pore size, distribution, volume and geometry. Furthermore, it is a simple method as compared with hollow sphere method and produces fully open pores.

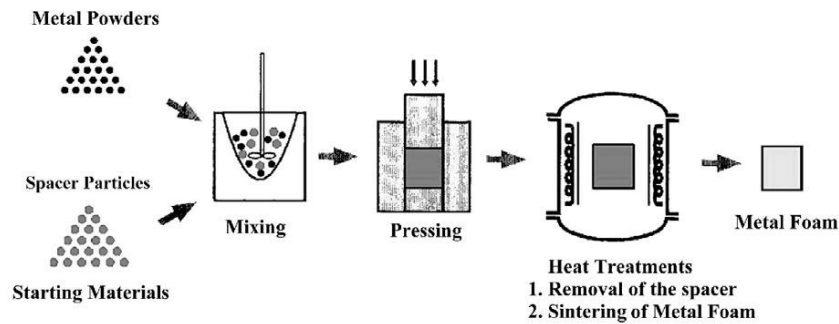


Figure 3.18. Schematic of space holder method of Ti foam processing (Source: Wen, et al. 2001)

3.3.4. Sintering of Powders Deposited on a Fugitive Scaffold

This technique is based on the utilization of fugitive space holding material such as polymer scaffold. The scaffold is repeatedly coated with the mixture of titanium powder and binder material. After removal of the scaffold and binder and subsequent sintering of the powders result in a reticulated open cell foam structure with hollow titanium struts (Figure 3.19). Three types of pores are present in these deposited scaffold type foams which are in order of increasing size: primary porosity within the struts, secondary pores at the core of the struts and open pores between struts. This method allows fabrication of high porous structures like hollow sphere sintering technique with less closed cell porosity (Li, et al. 2002). The compressive strength of Ti6Al4V foams produced by the above method with 90% porosity was reported to be 7-13 MPa by Li et al.

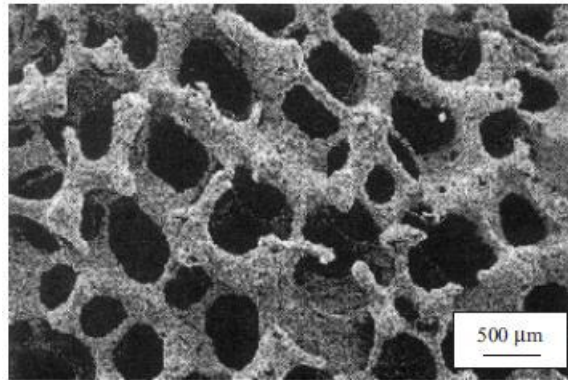


Figure 3.19. SEM micrograph of reticulated Ti6Al4V foam produced by sintering of powders deposited on a fugitive scaffold. (Source: Dunand 2004)

3.3.5. Powder Densification in Presence of Expansion of Trapped Gas Bubbles.

The basics steps of this process are shown in Figure 3.20. In a first step, powders are packed into a steel canister which is evacuated and backfilled with argon gas. Then, the powders are condensed by hot isostatic pressing. Since argon is neither soluble nor reactive with titanium, the gas is trapped within a continuous titanium matrix. At this step, argon gases are in the form of isolated, micron sized, high pressured bubbles with a low volume fraction less than 1%. Finally, after cooling and removal of steel canister, the titanium matrix is heated to an elevated temperature at ambient pressure. The reduced strength of the titanium matrix at high temperature allows the expansion of the high pressure gas bubbles (Murray and Dunand 2003). The resulting foam structure often has closed cell structure and generally denser than the foams produced by other methods. The porosity level rarely exceeds 50%. In the first four main sintering techniques of titanium powders, the final pore structure is dictated by the pre-sintering structure. However, in powder densification and gas expansion process, pore fractions are more related with the heating process independent of the original powder pre-form.

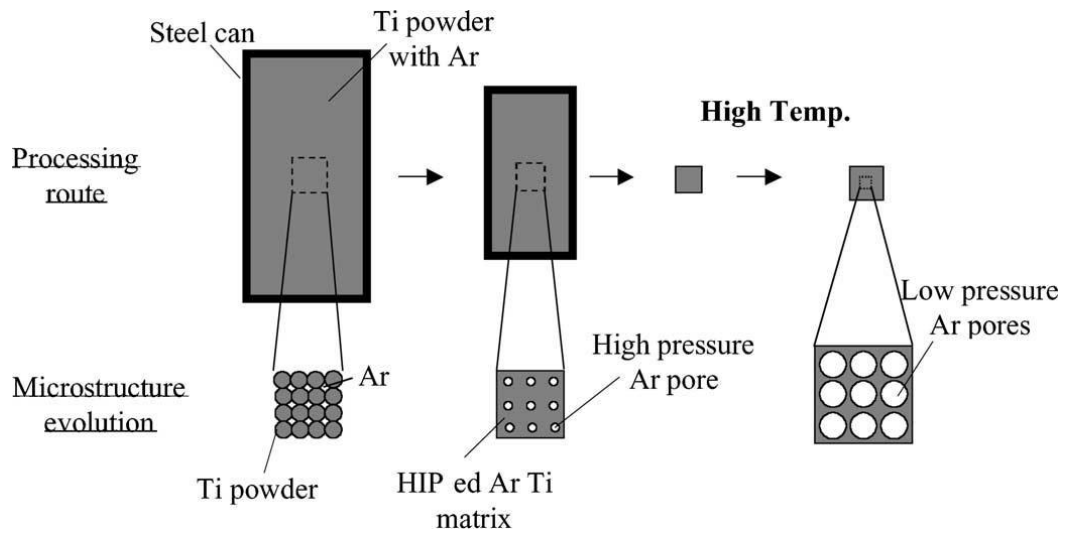


Figure 3.20. Schematic of foaming process, where titanium powders are compacted by hot isostatic pressing in the presence of argon and the resulting high-pressure argon bubbles then expand under low-pressure argon atmosphere at high temperature by Murray and Dunand. (Source: Murray and Dunand 2003)

CHAPTER 4

MATERIALS AND METHODS

4.1. Materials

Two different sizes of commercially available spherical Ti6Al4V powders produced by Crucible Research Corporation Company were used to prepare open cell foams (Figure 4.1). Powders were produced by gas atomization and coded as Powder 1 and Powder 2 according to sieve analysis: Powder 1 had particle size range between 45 and 150 μm and Powder 2 had a particle size range between 30 and 90 μm (Figure 4.2). The chemical compositions of the powders are further tabulated in Table 4.1 and satisfy ASTM 1580-1 standard (Specification for Titanium and Titanium-6 Aluminum-4 Vanadium Alloy Powders for Coatings of Surgical Implants), which is known to be a strict request for the manufacturing orthopedic implant structures. Complete version of ASTM 1580-1 standard was attached in Appendix A.



Figure 4.1. Crucible Research Ti6Al4V powders as received.

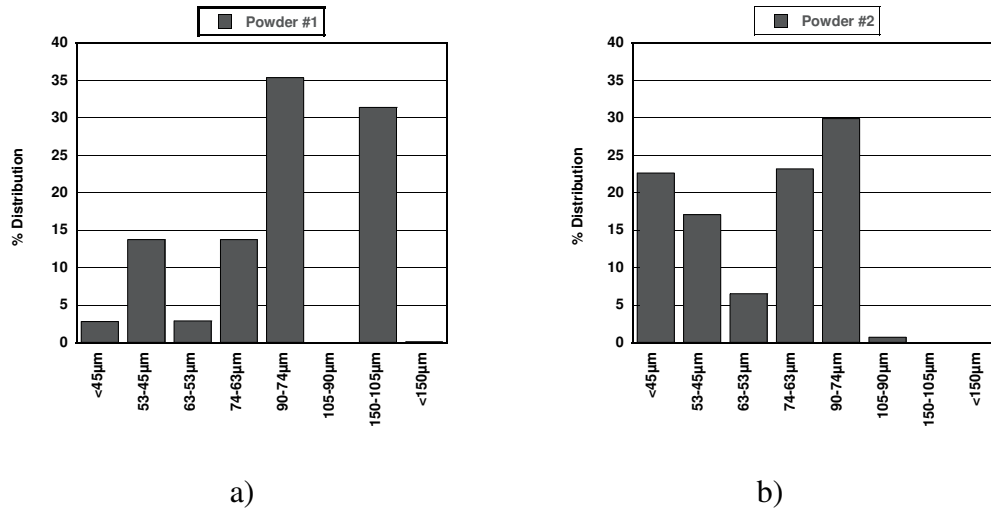
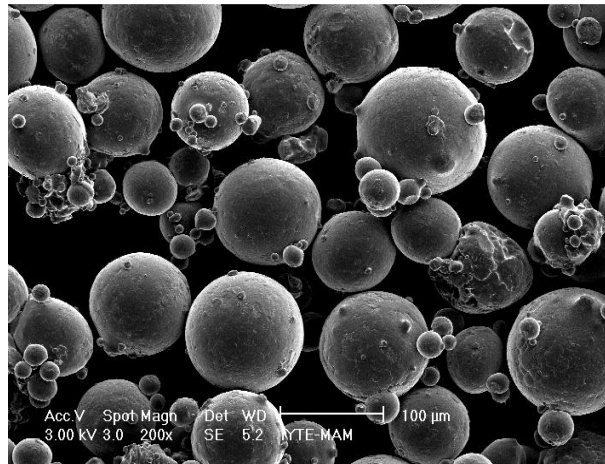


Figure 4.2. Powder particle size vs. distribution; a) Powder 1 and b) Powder 2.

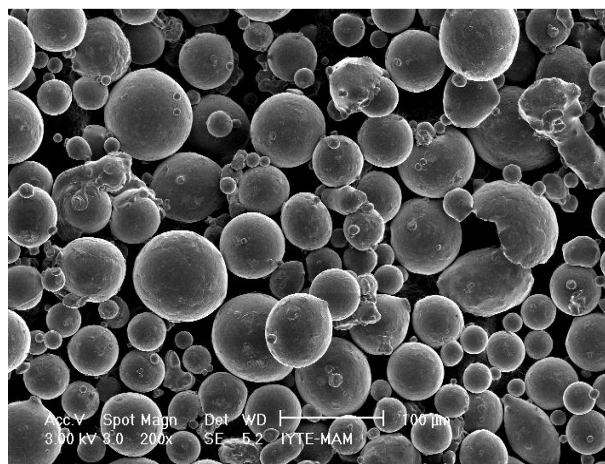
Table 4.1. ASTM standard for Ti6Al4V powder and chemical composition of used powders.

| Element | Al | V | O | Fe | C | H | N | Cu | Sn | Ti |
|---------------------|----------|---------|-------|------|-------|-------|-------|-----|-----|------|
| ASTM F1580-1 | 5.5-6.75 | 3.5-4.5 | 0.2 | 0.3 | 0.08 | 0.015 | 0.05 | 0.1 | 0.1 | Bal. |
| Powder | 6.27 | 4.0 | 0.149 | 0.05 | 0.085 | - | 0.011 | - | - | Bal. |

The scanning electron microscope (SEM) micrographs of the used Ti6Al4V powders are shown in the Figure 4.3 a) and b). Large particles are noted to contain small satellites attached to them resulting from powder atomization process as seen in Figure 4.3 a) and b). Nearly %80 of the particles in Powder 1, while only about %50 of the particles in Powder 2 are larger than 63 μm, showing a significant particle distributions differences between two powders. Since few percentages of relatively small particles are found, the particle distribution of Powder 1 is considered nearly monomodal. On the other hand, the particle of Powder 2 is bimodal, comprising relatively large (90 μm) and small (30-40 μm) particles as seen in Figure 4.3 b). However, it should be noted that the presence of small particles attached to large particles is expected to slightly increase the mean particle size and shift the particle distribution histogram of the powders toward larger sizes.



a)



b)

Figure 4.3. SEM micrographs showing the particles in a) Powder 1 and b) Powder 2

Although different types of space holder materials including urea (carbamide), ammonium bicarbonate and magnesium were used in the literature previously, Ammonium bicarbonate (Aldrich) was chosen as the space holder material in the foam preparation. The selection of the spacer material was based on its chemical properties, the capability to hold spaces of pores at room temperature and to decompose completely at relatively low temperatures so as to avoid the reaction with Ti6Al4V powders. The decomposition reactions of ammonium bicarbonate and urea are as follows;



Ammonium bicarbonate (Aldrich) sieved in a particle size range of 315-500 μm was used as space holder by an amount of 50-70 % of total volume. As received irregular shaped ammonium bicarbonate were sieved in particle range of 315-500 μm (Figure 4.4) to arrange the pore size of the structure.

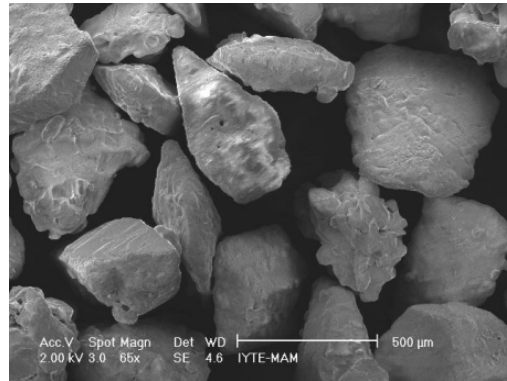


Figure 4.4. SEM micrographs of irregular ammonium bi carbonate space holder particles.

4.2. Preparation of Foams

The processing stages of foam preparation are sequentially shown in Figure 4.5 and started with the homogenous mixing of the ingredients (powder, space holder and binder). Green powder compacts of 40x40x10 mm in size were then compacted at room temperature inside a tool steel die at a pressure of 200 MPa. The compaction pressure imparted enough green strength to prevent the collapse of the compacts upon removal of the space holder and in the subsequent sintering process. Green compacts were then heat treated in incubator at 200 $^{\circ}\text{C}$ for 5 hours to remove the space holder. The resulting porous Ti6Al4V green powder compacts were inserted into an enclosed Ti box on a graphite plate which prevented the bonding between Ti box and Ti6Al4V foams in the sintering process and then sintered in a tightly enclosed horizontal tube furnace under highly purity (99.998) Ar flux (400 cm^3/min) at a temperature between 1200 and 1350 $^{\circ}\text{C}$ for 2 h. The heating profile of the furnace at a sintering temperature of 1200 $^{\circ}\text{C}$ is shown in Figure 4.6. During the cycle under Ar flux, compacts first were kept at 200 $^{\circ}\text{C}$ for 15 minutes to evaporate remaining space holders and then 500 $^{\circ}\text{C}$ for 1/2h in order to allow complete burning-off of the binder as seen in Figure 4.6. Heating rate of furnace were 10 $^{\circ}\text{C}/\text{min}$. In the cooling process, the compacts were also kept at 1000 $^{\circ}\text{C}$

for the formation of Widmanstätten structure. This process ended with the natural cooling of the compacts in the furnace.

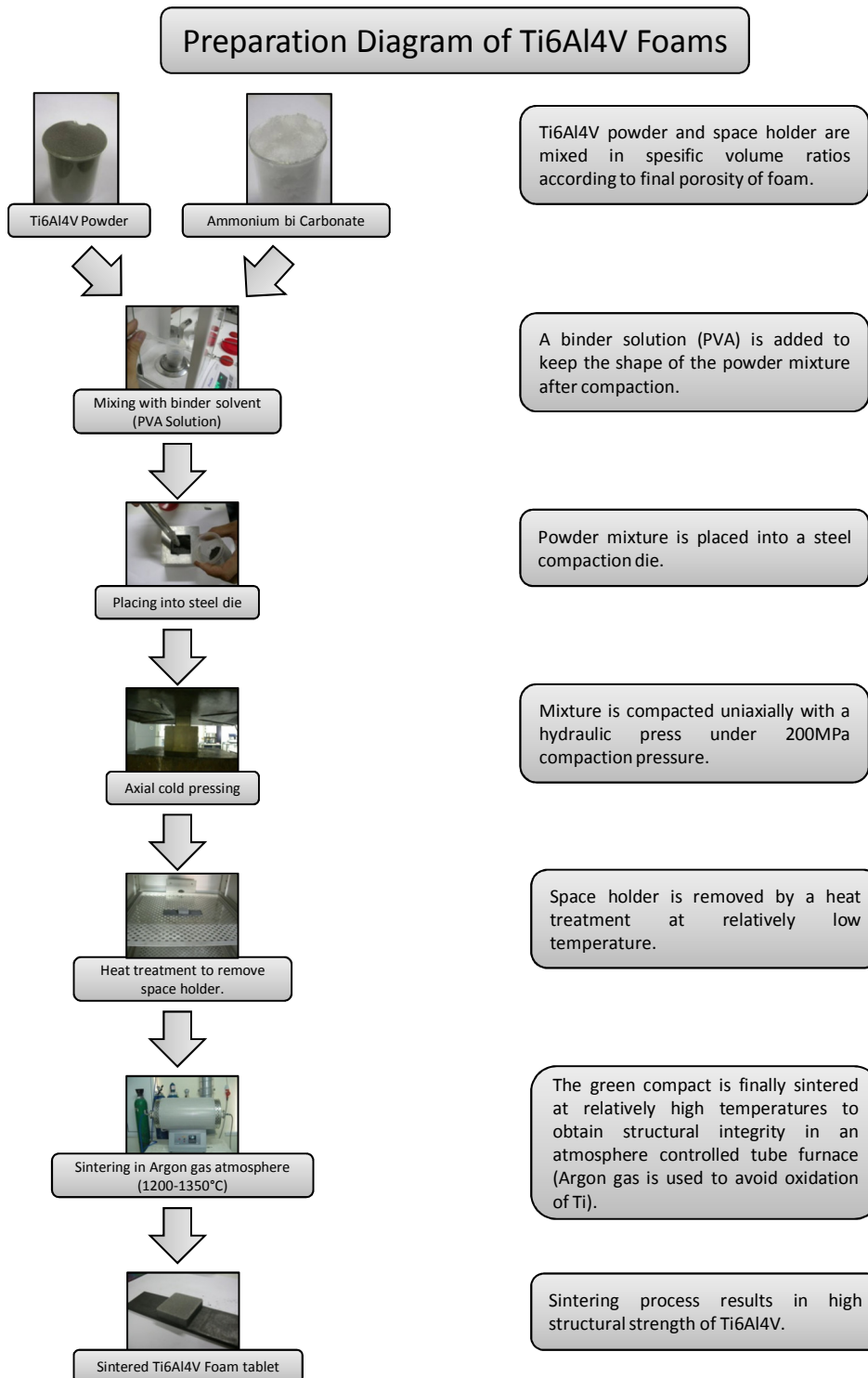


Figure 4.5. Preparation route for Ti6Al4V foams using space holder method.

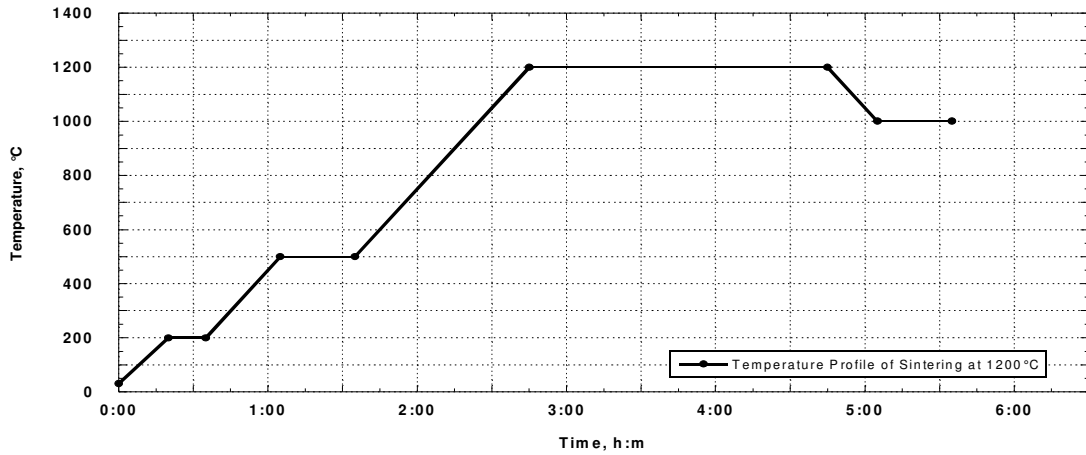


Figure 4.6. Heating profile of the furnace at a sintering temperature of 1200 °C.

The weights of powders and the corresponding binder solution used in the preparation of foams are tabulated in Table 4.2 for a 1 cm³ foam structure. In Table 4.2, the following equations were used to calculate the weights of Ti6Al4V and space holder weights respectively,

$$\text{Weight of Ti6Al4V Powder} = \frac{\text{Final Volume of Foam} \times (100 - \text{Porosity}) \times \text{Density of Ti6Al4V}}{100} \quad (4.3)$$

$$\text{Weight of Amm. bi Car. Powder} = \frac{\text{Final Volume of Foam} \times \text{Porosity} \times \text{Density of Amm. bi Car}}{100} \quad (4.4)$$

$$\text{Density of Ti6Al4V Powder} = 4.42 \text{ g/cm}^3$$

$$\text{Density of Amm. bi Car. Powder} = 1.59 \text{ g/cm}^3$$

Table 4.2. Mixture weight of Ti6Al4V, Ammonium bi Carbonate powders and PVA solution for fabrication of 1 cm³ foam structure.

| Porosity | Weight of Ti6Al4V (gr) | Weight of Amm.bi Car. (gr) | Weight of PVA Solution (gr) |
|----------|------------------------|----------------------------|-----------------------------|
| 50% | 2,21 | 0,79 | 0,08 |
| 60% | 1,77 | 0,95 | 0,07 |
| 70% | 1,33 | 1,11 | 0,06 |

The compression test samples were prepared by water jet cutting of the prepared foam plates through the normal to the plate thickness as shown in Figure 4.7 a) and b). Few of the samples were also prepared in cylindrical die using the above process stages and process parameters. A cylindrical sample prepared using cylindrical die is shown in Figure 4.7 c).

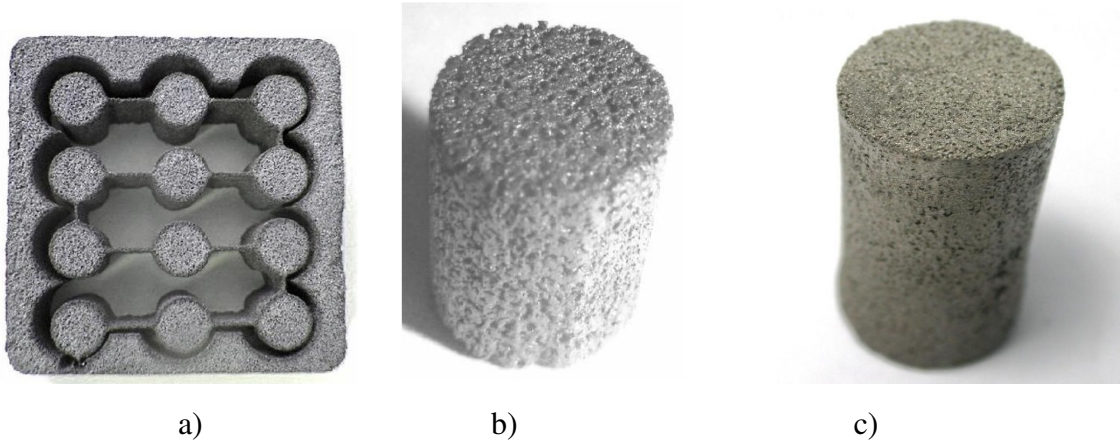


Figure 4.7. a) Water-jet cut foam sample sintered at 1350 °C (40 x 40 x 15 mm), b) cylindrical compression test sample (10 x 15 mm) and c) direct molding sample.

The percent porosity of the sintered Ti6Al4V foams was measured using the Archimedes' method after coating the foam sample surfaces with a thin layer of paraffin film. Following relations were used to calculate the porosity of the prepared foams;

$$d_{foam} = \frac{m_{air}}{\frac{m_{air} - m_{water}}{d_{water}}} \quad (4.5)$$

$$\% \text{ Porosity of foam} = \left(\frac{d_{Ti6Al4V} - d_{foam}}{d_{Ti6Al4V}} \right) \times 100 \quad (4.6)$$

m_{air} = mass of Ti6Al4 foam in air

m_{water} = mass of Ti6Al4V foam in water (coated with paraffin film)

d_{foam} = density of Ti6Al4V foam

d_{water} = density of distilled water

$d_{Ti6Al4V}$ = density of solid Ti6Al4V

4.3. Equipment

Thermo-Gravimetric Analyses (TGA) of the space holder and binder were performed using a Perkin Elmer Diamond Thermo-Gravimetric Analyzer. The optical microscopic analyses are performed using Nikon Eclipse L150 and Laica. Scan electron microscope observations performed using Philips XL30-SFEG SEM with an Energy Dispersive X-ray (EDX). The polished surfaces cross sections of the epoxy mounted foam samples were etched with Kroll's reagent (3 cm³ of HF and 6 cm³ of HNO₃ in 100 mL of H₂O). A Philips X'pert X-ray diffraction (XRD) instrument with Cu-K α radiation was used for the phase determination. The quasi-static compression tests were conducted using a displacement controlled SHIMADZU AG-IX 300K universal tension-compression test machine with a cross-head speed of 0.9 mm/min and 90mm/min, corresponding to strain rate of 10⁻³ and 10⁻¹ s⁻¹. At least three compression tests were performed for each foam sample prepared using two different powders at different sintering temperatures and porosities.

Designing of the spinal cages were performed by using a computer image analysis program, Adobe Photoshop, SolidWork 3D design software and AutoCAD computer drawing software.

4.4. Designing Spinal Cages

The design steps of spinal cages preparation are sequentially shown in Figure 4.8. Initially, the images of an adult human vertebra segments were supplied by Dr. Ömer Akçalı, in 9 Eylül University, Medicine Faculty. The vertebra segments were then labeled C, T and L according to their positions on the spine (C - Cervical, T - Thoracic and L - Lumbar). Also numbers were given as indicating their position on vertebrae array from top to bottom.

Designing Diagram of Ti6Al4V Spinal Cages

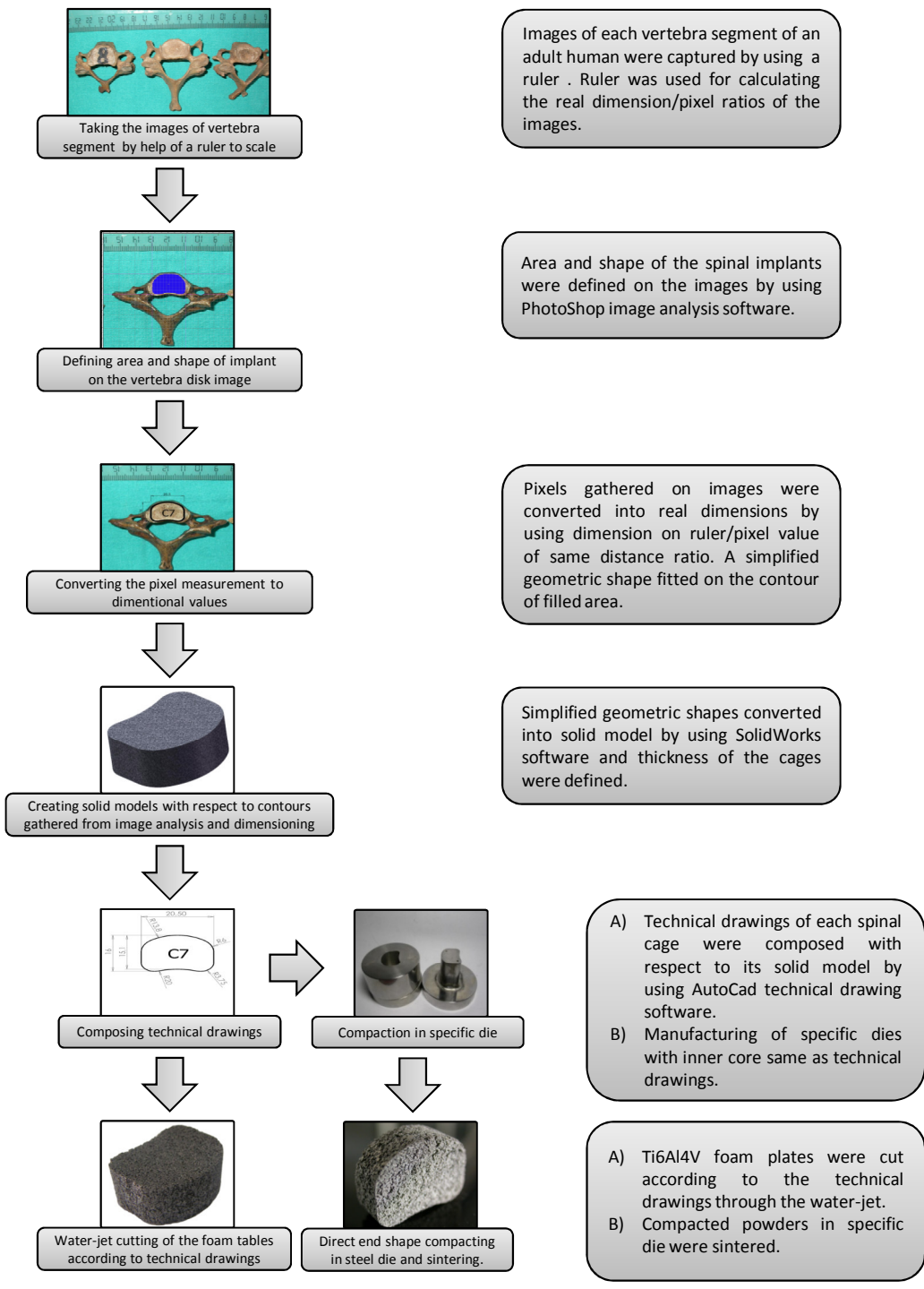


Figure 4.8. Designing route of Ti6Al4V spinal cages.

Figure 4.9 shows the sections of a vertebra segment. Since nerves pass through the foramen canal, restrictions should be taken into account in the design of spinal cages. The implant fixation had major importance between two vertebra segments, usage of vertebral disc walls as a border to minimize the implant movement, and leaving a safe distance between implant and posterior canal to keep nerves damaged by implant during surgery and also post surgery period. The images of each vertebra segment with a reference ruler were taken to perpendicular on the disc surface. This ruler was used in the calculation of distance/pixel ratio in the images. Preliminary spinal cage designs were done on the vertebral disc sections using Adobe Photoshop software by filling the disc region with blue color. Dimensional conversions of the blue areas were done using real distance-pixel ratio and converted into defined contours. Based on these contours, solid model of each segment was created using SolidWorks design software. The thickness of the cages was decided based on the consultation with Dr. Ömer Akçalı. 2D technical drawings of each spinal cage were composed using AutoCad drawing software. At the final stages of designing of spinal cages, 40 x 40 mm Ti6Al4V foam plates in different thicknesses were cut as in the design drawings through water-jet and spinal cages extracted from simple geometry of foam.

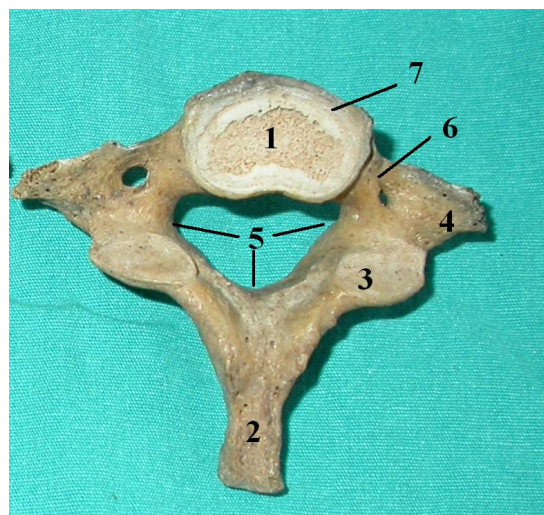


Figure 4.9. Vertebra sections; 1. vertebral disc, 2. spinous, 3. articular, 4. transverse, 5. foramen, 6. pedicle, 7. vertebral disc wall.

CHAPTER 5

RESULTS AND DISCUSSIONS

5.1. Materials

The TGA and DTG curves of ammonium bicarbonate, urea and PVA solution are shown in Figure 5.1, respectively.

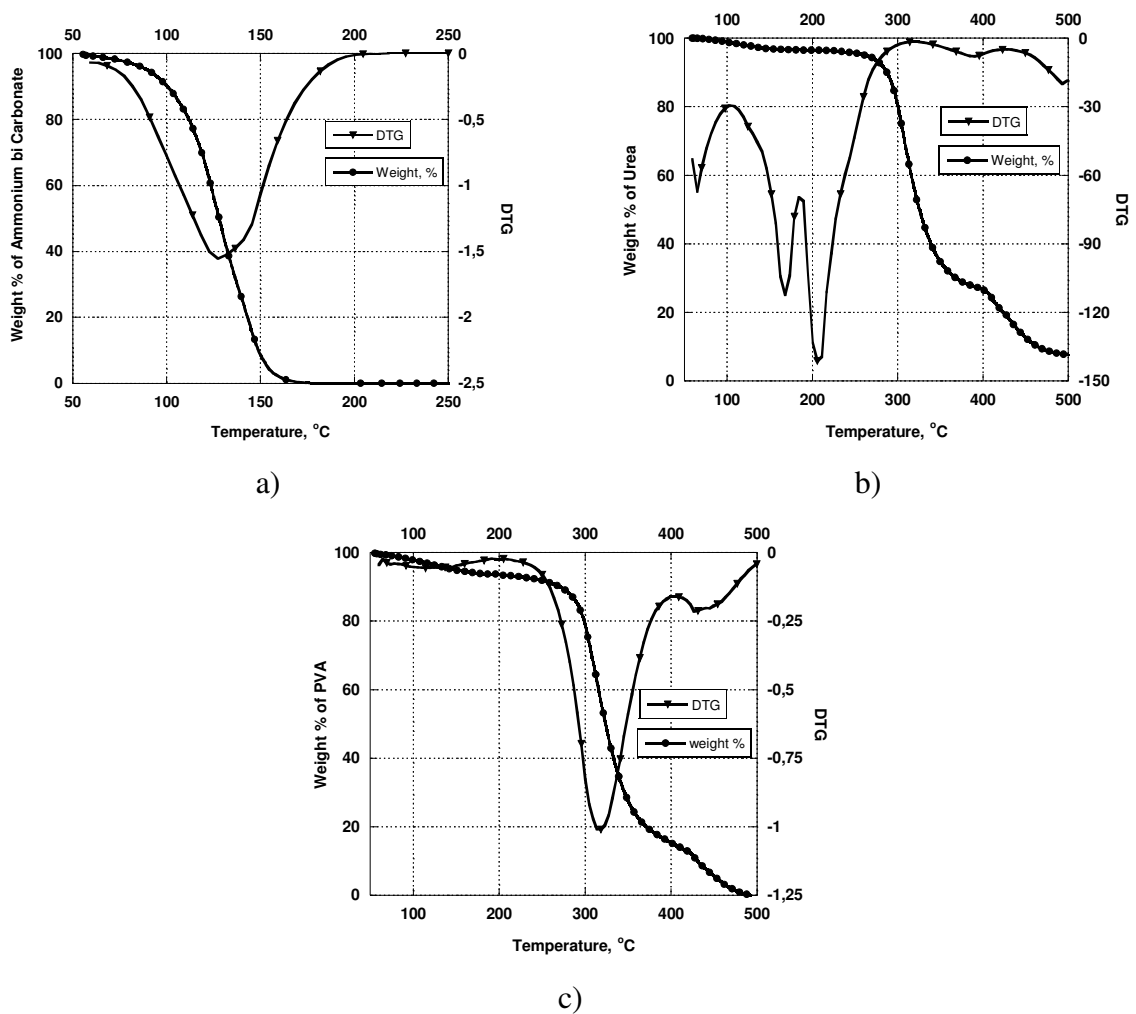
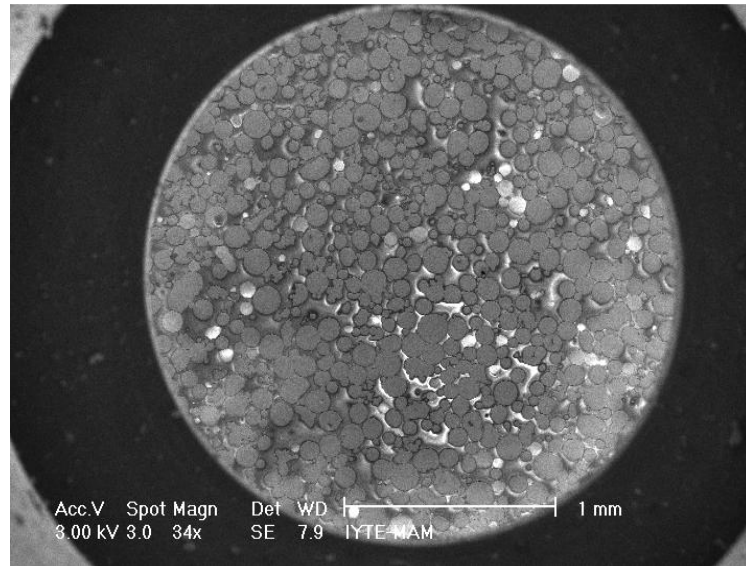


Figure 5.1. TGA and DTG curves of a) Ammonium bi carbonate, b) Urea and c) PVA.

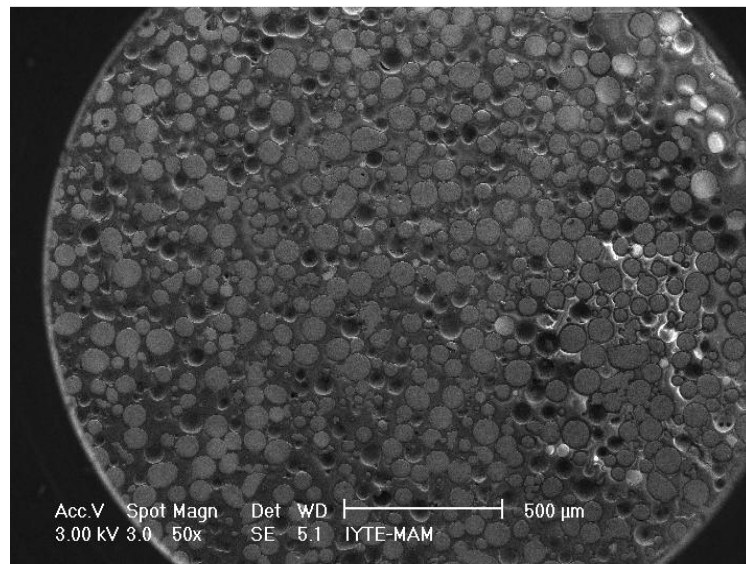
As is seen in Figure 5.1 a), ammonium bicarbonate decomposition started above 50 °C and continued up to 175 °C. 130 °C was critical temperature for decomposition of ammonium bicarbonate since DTG curve made a peak. This showed maximum decomposition rate of ammonium bicarbonate. PVA decomposition was however completed at a much higher temperature, 480 °C (Figure 5.1 c)). The space holder and binder removal temperatures in foam preparation were selected just above the complete decomposition temperatures, 200 and 500 °C, respectively. For comparison, the TGA curve of urea (carbamide), which is commonly used as space holder, was also shown in Figure 5.1 b). The decomposition of urea as seen in Figure 5.1 b) was not completed until about 600 °C. It was noted previously that the reaction between Ti powder and the cracking products of the space holder must be avoided in the temperature range of 300-600 °C in order to prevent the formation of interstitial solid solutions with carbon, oxygen and nitrogen, which is detrimental for the ductility (Bram, et al. 2000).

5.2. Microstructure of Ti6Al4V Powders

Figure 5.2 shows SEM images of epoxy mounted and polished cross sections of Powder 1 and Powder 2. The microstructure of the as-received powders was determined using these epoxy mounted, polished and etched samples. As shown in Figure 5.3 a) and b) the microstructure of as-received powder was composed of needle-like α phase, referred as acicular alpha (α). Ti6Al4V powders were produced by gas atomization process in which the liquid metal is forced through an orifice at a sufficiently high velocity to ensure turbulent flow. Then spreading particles are cooled rapidly to obtain powder material. Since melted Ti6Al4V phase was cooled by quenching, resulting powders structure transformed into martensitic structure. Because of the rapid cooling, the vanadium atoms were trapped in needle like α -phase.

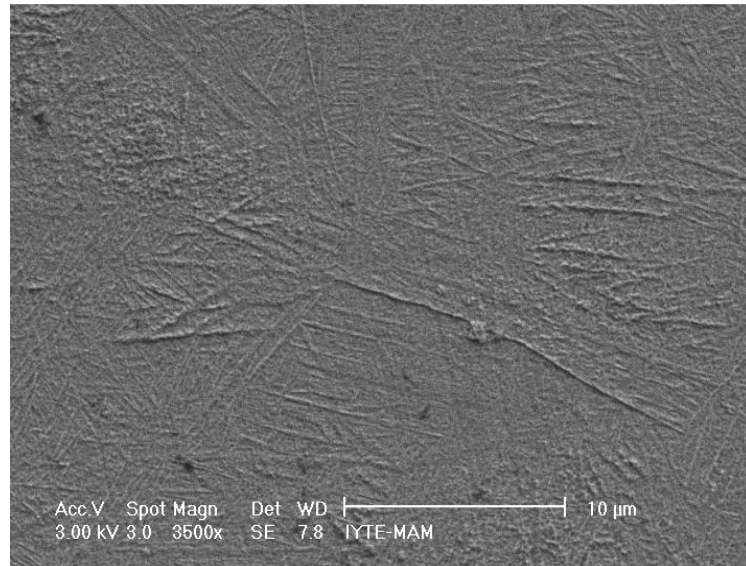


a)

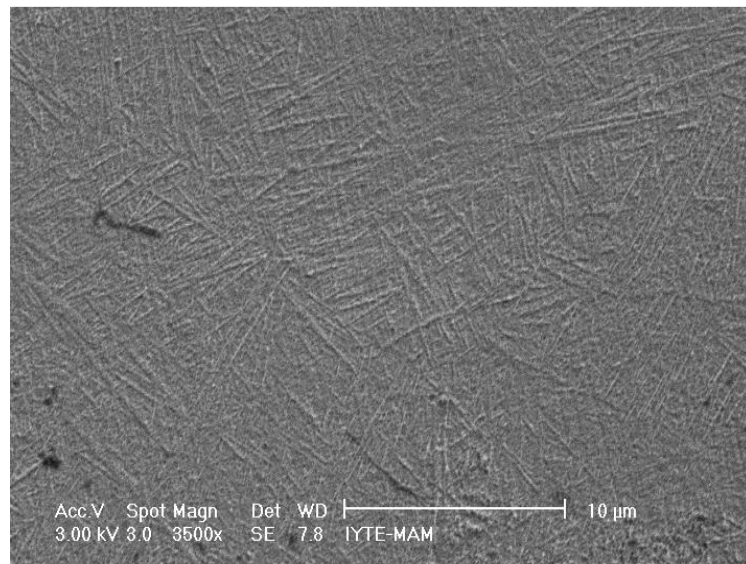


b)

Figure 5.2. SEM images of epoxy mounted and polished as-received powders a) Powder 1 and b) Powder 2.



a)



b)

Figure 5.3. Magnified SEM images showing fine needle like α -phases for a) Powder 1 and b) Powder 2.

The XRD spectra of the as-received Powder 1 and Powder 2 particles and prepared foams sintered at 1200, 1250, 1300 and 1350 °C are shown sequentially in Figure 5.4 a) and b), respectively. The microstructure of the powders transformed from fully needle-like α -phase into Widmanstätten microstructure of colonies of β lathes (bcc and rich in V) and α platelets (hcp and rich in Al) after sintering above 1000 °C. Figure 5.5 a) and b) show Widmanstätten structure of SEM micrographs of foams particles sintered at 1200 and 1350 °C, respectively.

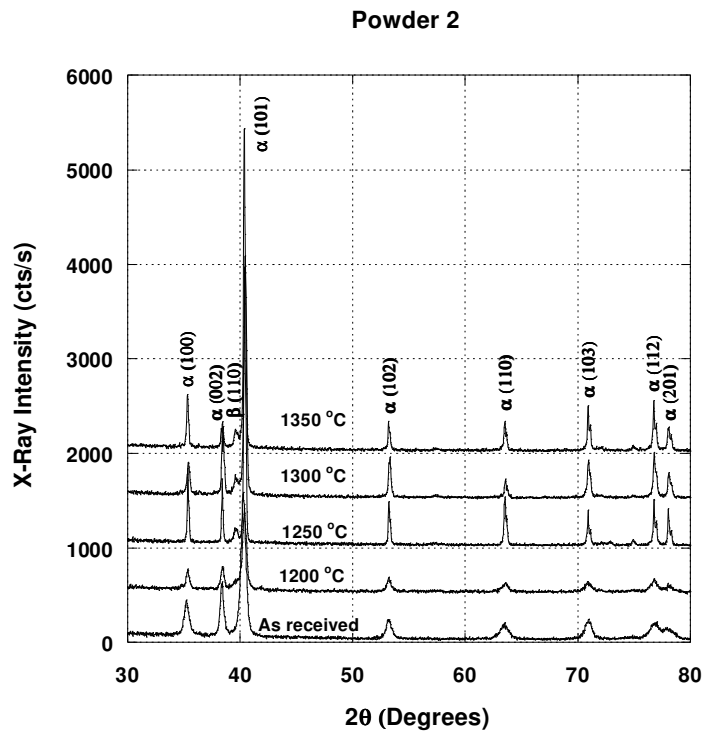
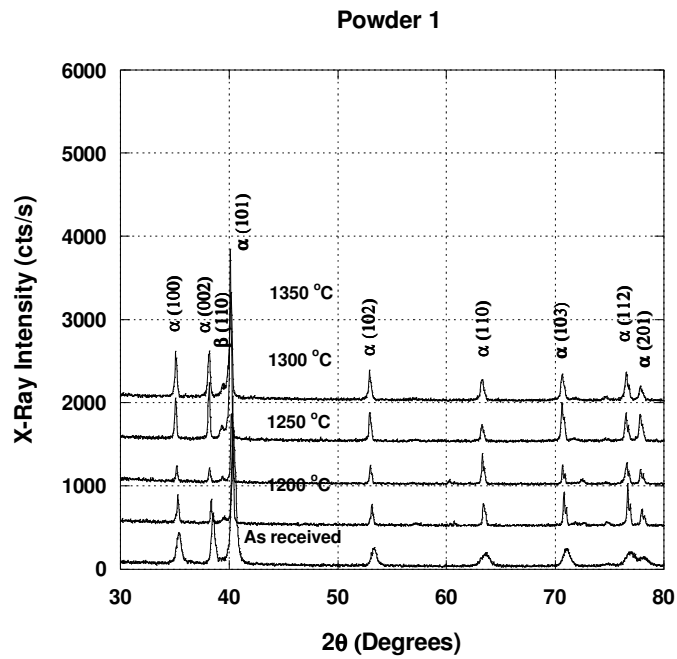
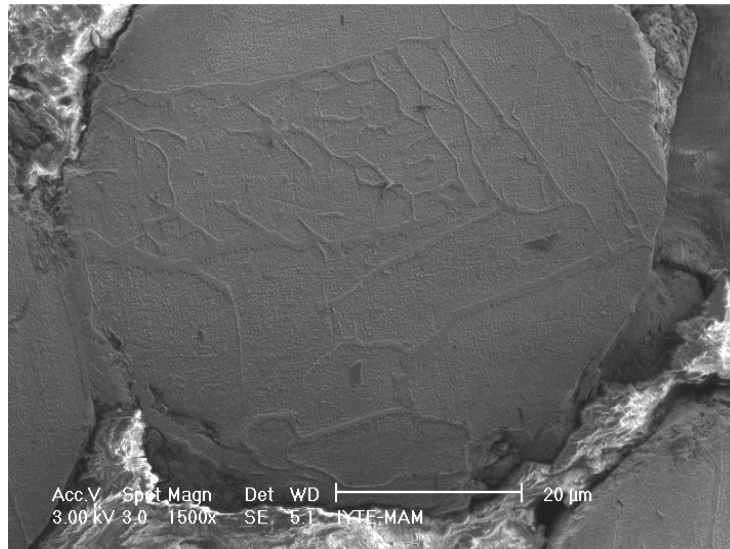
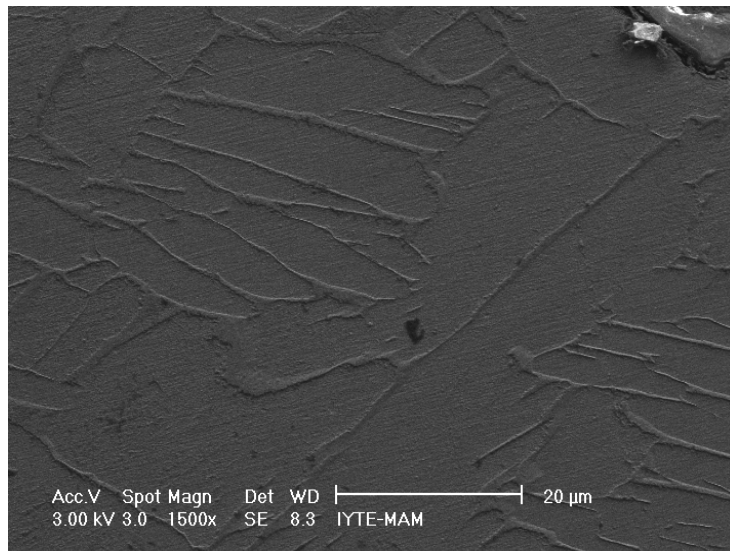


Figure 5.4. XRD spectra of sintered a) Powder 1 and b) Powder 2 foams and as-received powder.



a)



b)

Figure 5.5. SEM micrographs of sintered samples at sintering temperature a) 1200 °C and b) 1350 °C for 2h.

The corresponding optical microscope images of the prepared foams are also shown in Figure 5.6 a) and b). The thickness of β -phases were measured nearly 0.5 - 1 μm . Ratio of formation of α -phases were observed as increasing at and near the inter particle bond region (sintering bonds). The SEM and optical microscope observations showed that the size of β -phases slightly increased at increasing sintering temperatures. Sintering at higher temperatures resulted in higher rate of diffusion of vanadium atoms out of the crystal structure. The schematic of the Ti6AlV phase diagram was further shown in Figure 5.7. At 4 wt% V, above 1066 °C the structure transforms into β -phase

(bcc). The slow cooling in the furnace results in the development of the Widmanstätten microstructure ($\beta \rightarrow \alpha + \beta$), while quenching results in martensitic transformation ($\beta \rightarrow \alpha'$).

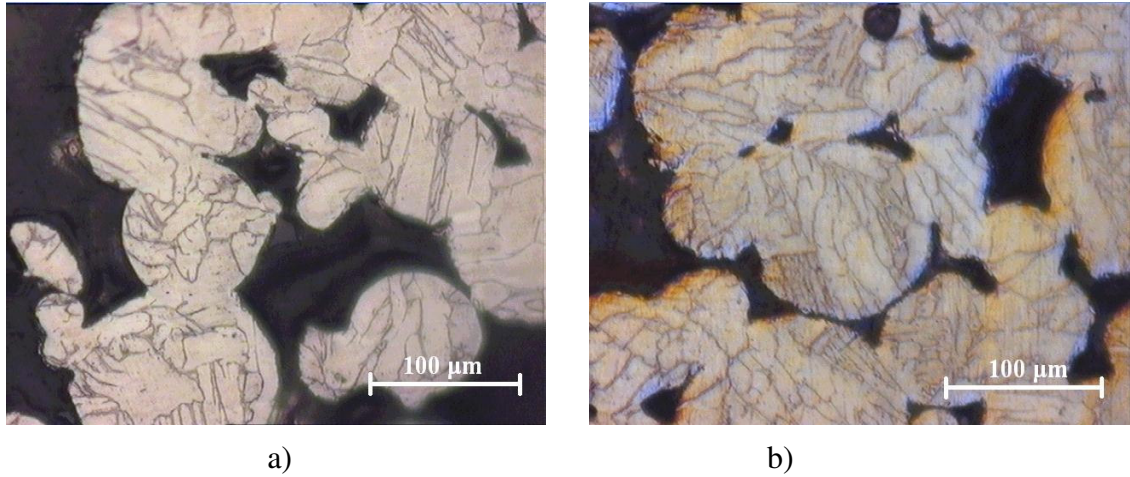


Figure 5.6. Light optical micrographs of sintered samples at sintering temperature a) 1200 °C and, b) 1350 °C for 2h.

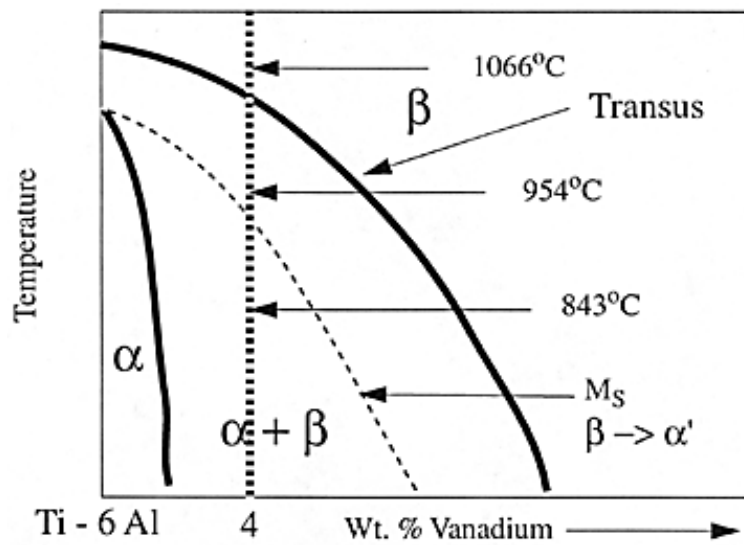


Figure 5.7. Pseudo-binary Ti-6Al-4V Diagram

Table 5.1 tabulates the oxygen contents of Powder 2 foams sintered between 1200 and 1350 °C temperatures. Table 5.1 clearly shows the increasing tendency of the oxidation of the powder surfaces by the increasing sintering temperature. The oxygen content increased 4 to 6 times that of the starting powder. Although sintering was performed under high purity Ar atmosphere, the oxidation of the particle surface took place due to the extreme reactivity of titanium to oxygen. The oxygen content of the foams were determined from the crushed foam samples and therefore the results showed the overall oxygen content of the foams, including a thin TiO₂ formed on the particle surfaces. In order to reduce the level of oxygen content, controlled acid aging of the foam samples were recommended. Acid aging was shown to remove the oxide layer on the surfaces of Ti6Al4V particles.

Table 5.1. Wt.% oxygen content of as received powder and foam samples sintered between 1200 and 1350 °C

| Sintering Temperature (°C) | Oxygen Content (wt.%) |
|----------------------------|-----------------------|
| As Received | 0.149 |
| 1200 | 0.6 ±0.1 |
| 1250 | 0.66 ±0.01 |
| 1300 | 0.67 ±0.01 |
| 1350 | 0.9 ±0.1 |

5.3. Porosity

The percent mean porosities of the prepared foams are tabulated in Table 5.2 as function of sintering temperature and powder type. The porosities of the foams varied between 58.1 and 62.2%. The variations in percent porosities between the foam samples sintered at different temperatures were likely due to the variations of the amount of space holder in relatively small samples used in the porosity measurements. Nevertheless, the final porosities of the foams prepared were quite similar and corresponded nearly to the starting volume percentages of the space holder.

Table 5.2. Mean percent porosity of foams as function of sintering temperature.

| Powder | Temperature (°C) | Density (g/cm ³) | Mean Porosity (%) | Std. Dev. |
|--------|------------------|------------------------------|-------------------|-----------|
| 1 | 1200 | 1,761 | 60.1 | 0.732 |
| | 1250 | 1,799 | 59.3 | 0.716 |
| | 1300 | 1,749 | 60.4 | 0.603 |
| | 1350 | 1,697 | 61.6 | 0.652 |
| 2 | 1200 | 1,714 | 61.2 | 0.856 |
| | 1250 | 1,707 | 61.4 | 0.658 |
| | 1300 | 1,670 | 62.2 | 0.435 |
| | 1350 | 1,850 | 58.1 | 0.596 |

It was found experimentally that the shrinkage was more pronounced in big size green compact sintering. Figure 5.8 a) and b) show 40 x 40 x 20 mm foam compact pictures after and before sintering, respectively. The foam, contained 60% space holder, were compacted at 200MPa and sintered at 1300 °C. The shrinkage was measured nearly 10% of initial volume. As the compaction of big size green compacts in a steel die resulted in a less dense core as compared with the upper and lower regions, larger amounts of shrinkages of the green compacts in the mid sections were naturally expected during sintering. For that reason, sintering bigger size compacts resulted in more dimensions changes, than the sintering of smaller size green compacts.

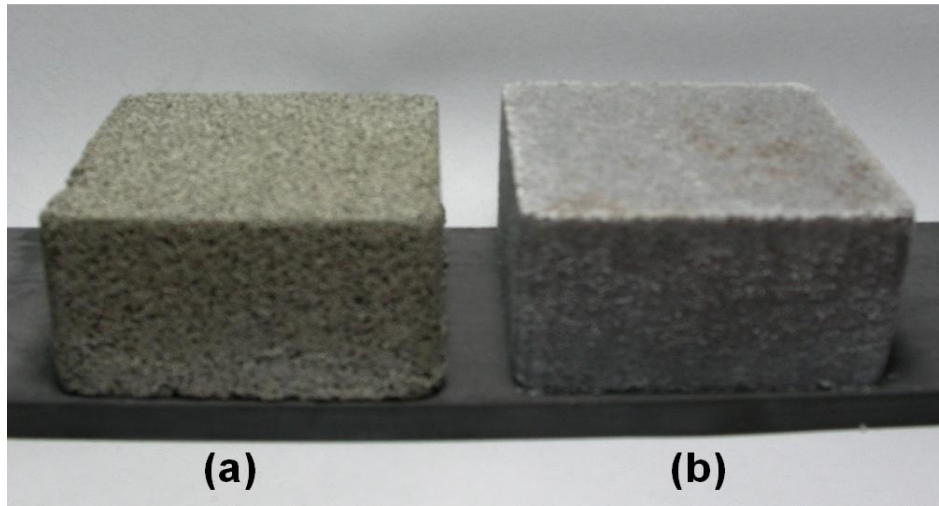


Figure 5.8. Pictures of a) sintered foam (1300 °C) and b) green compact.

Figure 5.9 shows SEM micrograph of a water-jet cut cross section of Ti6Al4V foam surface. The pores after water jet cut were still open, while the surface was smeared. The representative optical micrograph of the resulting cell structure of the prepared foams is shown in Figure 5.10. The cellular structure of foams shown in Figure 5.10 comprises two different pore size ranges. Relatively larger and irregular shaped cells (macro pores) with the sizes of 300-500 μm resulted from the spaces left by the irregular shaped space holder. While, smaller pores of 1-30 μm (micro pores) were found in between the sintered Ti6Al4V particles in the cell walls/cell edges result from the incomplete sintering process.

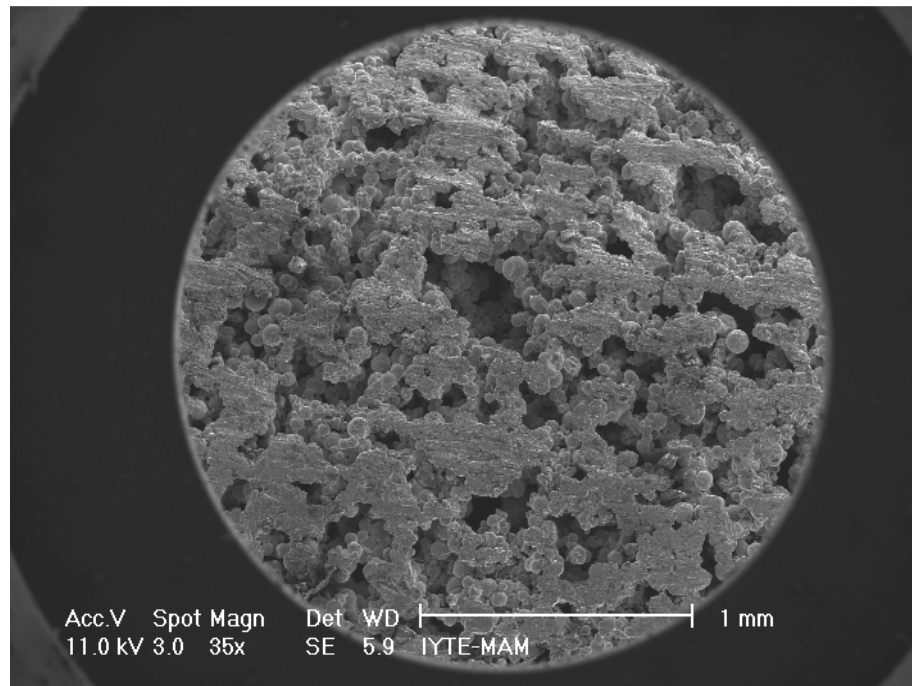


Figure 5.9. SEM micrograph of typical water jet cut surface of a Ti6Al4V foam.

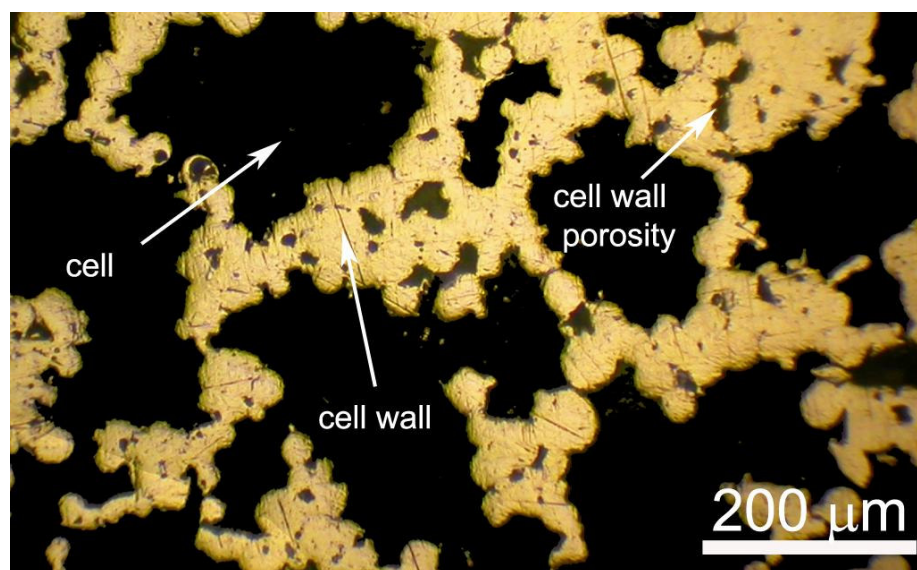


Figure 5.10. Optical micrograph of Powder 2 foam cell structure (sintered at 1300 °C).

Macro pores or cell arrays were specifically fabricated for the ingrowths of the new bone tissues and the transport of the body fluids. The sizes of micro pores were depended on Ti6Al4V powder particle diameter. The use of smaller particles is naturally expected to decreases the sizes of the micro pores. The micrographs in Figures

5.11 a) and b) show Ti6Al4V particles in the cell walls of Powder 2 foam samples sintered at 1200 and 1350 °C, respectively. The effect of sintering temperature on the sintering necks of the powders is clearly seen in these micrographs. At lower sintering temperatures (Figure 5.11 a)), the sintering necks and/or contact areas between the particles were relatively narrower, while at higher sintering temperatures (Figure 5.11 b)), the neck regions became thicker. Similar effects of sintering temperature on the sintering necks of the Powder 1 foams cell walls were also observed. Compared to Powder 2 foam samples (Figure 5.11 b)), Powder 1 foam samples (Figure 5.11 c)), showed relatively fewer number of sintering necks and smaller contact areas between the particles in the cell walls at the same sintering temperature. The cell wall structure of the foams of two different powders will also be found to affect the compression mechanical responses as will be elaborated later. The effects of sintering temperature on the size of the micro pores are shown in Figure 5.12. The increase of sintering temperature reduced the size of the micro pores.

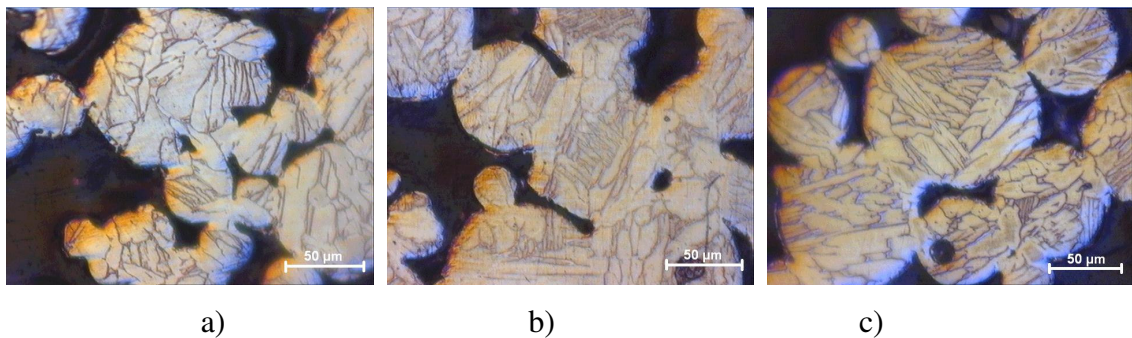


Figure 5.11. Optical micrographs showing Ti6Al4V particles in the cell walls: a) Powder 2 foam sintered at 1200 °C, b) Powder 2 foam sintered at 1350 °C and c) Powder 1 foam sintered at 1350 °C.

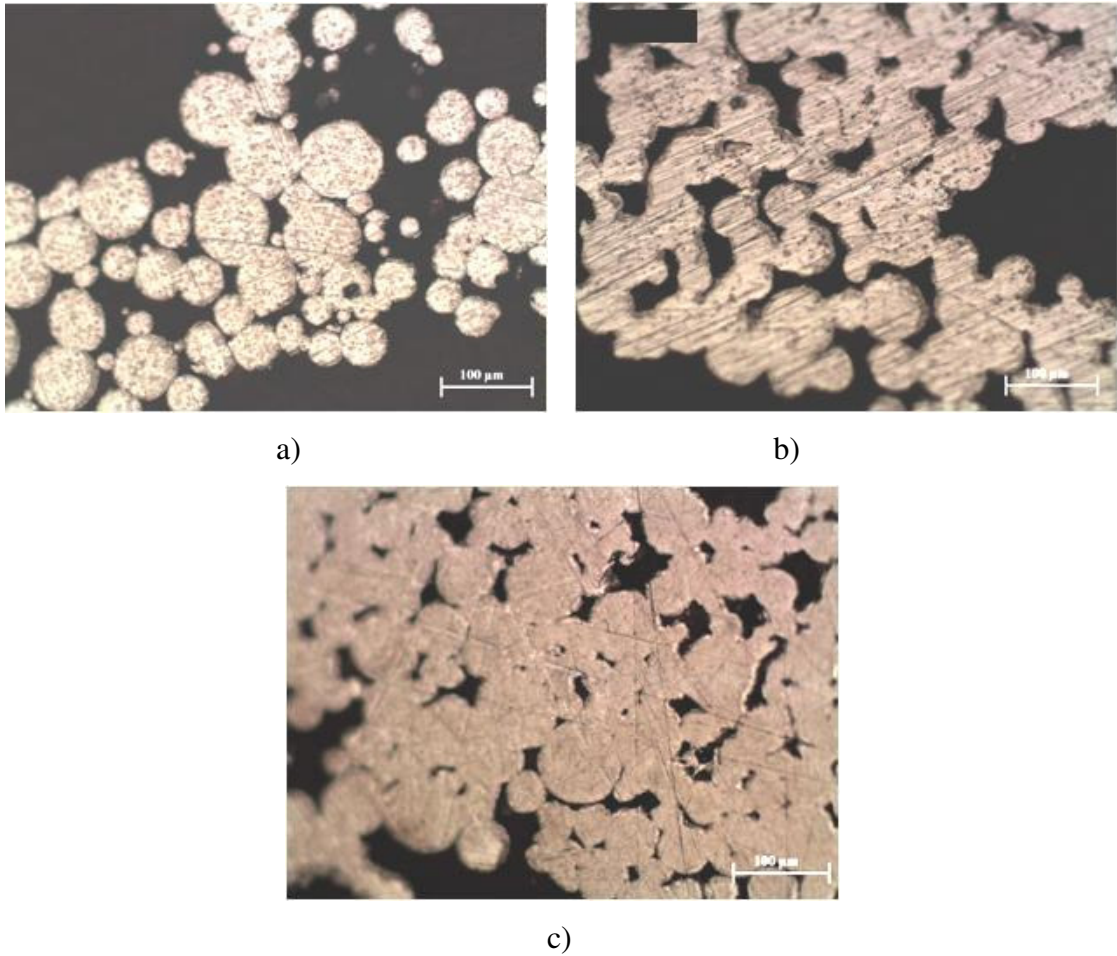


Figure 5.12. Optical micrographs showing Ti6Al4V foam cell walls a) Powder 2 green compact, b) Powder 2 foam sintered at 1200 °C and c) Powder 2 foam sintered at 1350 °C.

In green compacts, powder particles were contacted to each other resulting from the applied pressure in the steel die. The pressure formed indentation at the contact regions (Figure 5.12 a)). The sintering operation at 1200 °C decreased the gaps between the particles (Figure 5.12 b)), while sintering at relatively high temperature further minimized the gaps between particles and hence reduced the size of the micro pores (Figure 5.12 c)).

5.4. Compression Tests

5.4.1. Stress-Strain Curves of Ti6Al4V Foam Samples

Typical stress-strain curves of 60% porous Powder 2 foam sample at a 10^{-3} s^{-1} strain rate are shown in the Figure 5.13. The differences in the stress values between the individual tests were relatively small up to failure strains as seen in the Figure 5.13. Curves of the foams can be considered in three distinct deformation regions masked as I, II and III in the same figure. In region I, foams were elastically deformed up to about proportional limit (yield strength) and elastic modulus and yielding strength were calculated in this part. In the region II, the stress values increased as the strain increased. This inelastic deformation in II region took place under normal and shear forces. The strain values corresponding to maximum stress or compressive strength were taken as failure strain as shown in Figure 5.13.

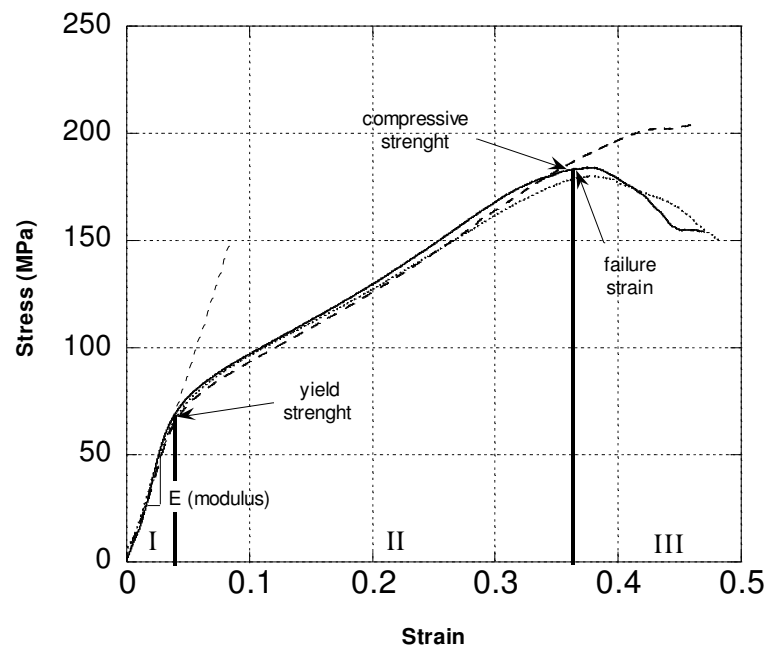


Figure 5.13. Compression stress-strain curves of three Powder 2 foam samples sintered at 1350 °C.

The compression stress-strain curves of Powder 1 and Powder 2 foams were sequentially shown in Figure 5.14 and 5.15 as a function of sintering temperature (1200 to 1350 °C) for 60% porous foams (2h sintering time, 200 MPa compaction pressure).

Powder 1 and Powder 2 foams showed similar trends in compression stress-strain behavior: the initial elastic deformation was followed by an inelastic deformation until maximum stress. The effect of increasing sintering temperature was to increase the elastic modulus, yield and compressive strength, and failure strain of the samples. Average elastic modulus values of foam samples are tabulated in Table 5.3. The elastic modulus values of Powder 1 and Powder 2 foams increased from 0.93 to 1.54 and from 1.49 to 2.5 GPa when the sintering temperature was increased from 1200 to 1350 °C, respectively for 60% porous samples. Figure 5.16 and 5.17 show the variations of yield and compressive strength of foams as a function of sintering temperature. Same with elastic modulus values, the yield strength values of Powder 1 foam increased from 22 to 50 MPa when the sintering temperature increased from 1200 to 1350 °C. The yield strength values of Powder 2 foams increased from 42 to 75 MPa in the same temperature range. Although sintering temperature increased the compressive strength of the foams prepared, the effect was more pronounced in Powder 2 foams. This is partly due to the higher packing ratio of Powder 2, which increased the number of contacts and bonding area between the particles.

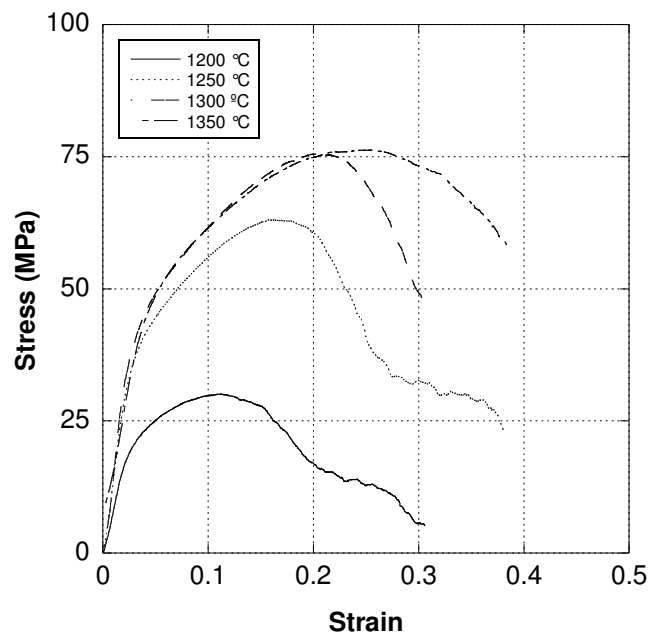


Figure 5.14. Typical stress-strain curves of 60% porous Powder 1 foams sintered at different temperatures (strain rate: 10^{-3} s^{-1}).

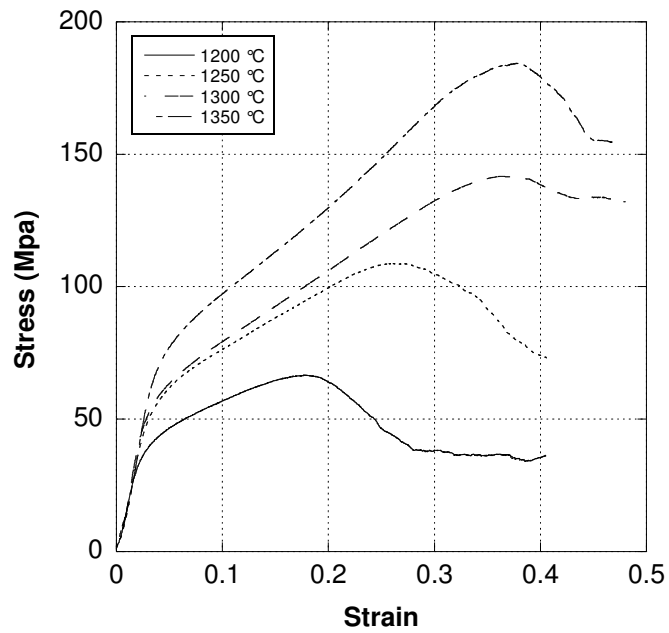


Figure 5.15. Typical stress-strain curves of 60% porous Powder 2 foams sintered at different temperatures (strain rate: 10^{-3} s^{-1}).

Table 5.3. Average elastic modulus of 60% porous foams as function of sintering temperature.

| Powder | Temperature ($^{\circ}\text{C}$) | Mean Modulus (GPa) | Std. Dev. |
|--------|------------------------------------|--------------------|-----------|
| 1 | 1200 | 0.93 | 0.121 |
| | 1250 | 1.11 | 0.121 |
| | 1300 | 1.44 | 0.019 |
| | 1350 | 1.54 | 0.450 |
| 2 | 1200 | 1.49 | 0.048 |
| | 1250 | 1.89 | 0.091 |
| | 1300 | 2.21 | 0.128 |
| | 1350 | 2.50 | 0.005 |

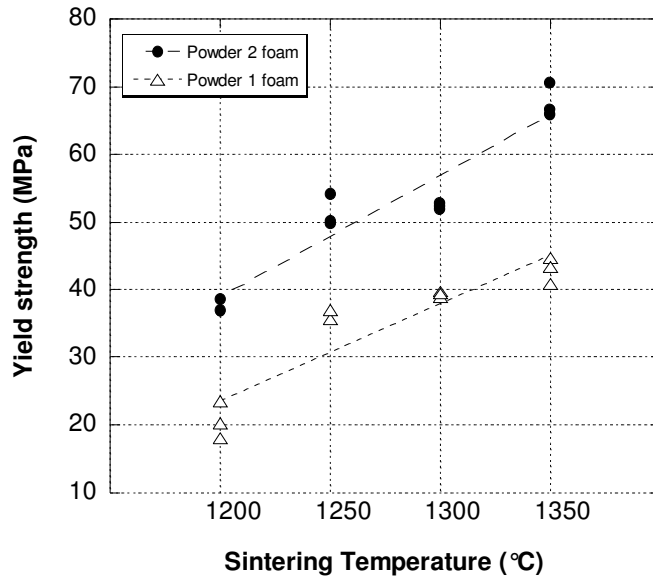


Figure 5.16. Variation of yield strength of 60% porous foams as a function of sintering temperature.

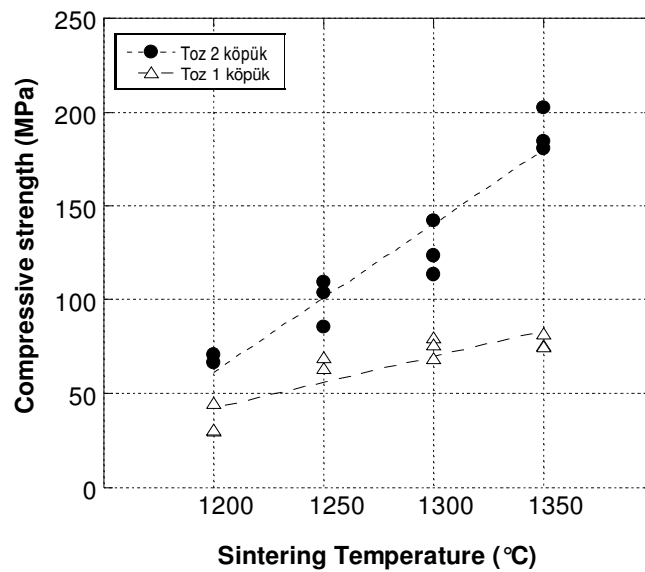


Figure 5.17. Variation of compressive strength of 60% porous foams as a function of sintering temperature.

Figure 5.18 shows the stress-strain curves of foams at different percent porosities sintered at 1300 °C. The elastic modulus, yield and compressive strength of the foams increased with decreasing porosity. Foams with 70% and 60% porosity had mean yield strength of 25 and 55 MPa, respectively, whereas 50% porous foams had

105 MPa (Figure 5.19). The compressive strength of 50% porous foam was higher than 200 MPa, 60 and 70% porous foams had average compressive strength of 130 and 50 MPa at 10^{-3} s^{-1} strain rate, respectively (Figure 5.20).

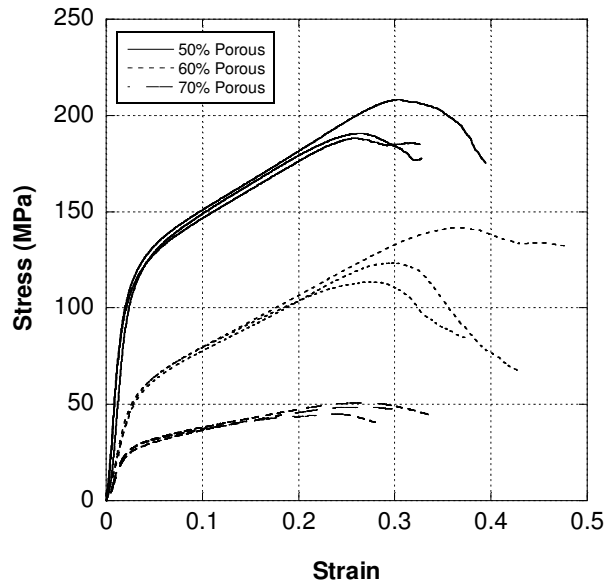


Figure 5.18. Stress-strain curves of 50, 60 and 70 % porous Powder 2 foams sintered at $1300 \text{ }^\circ\text{C}$ (strain rate: 10^{-3} s^{-1}).

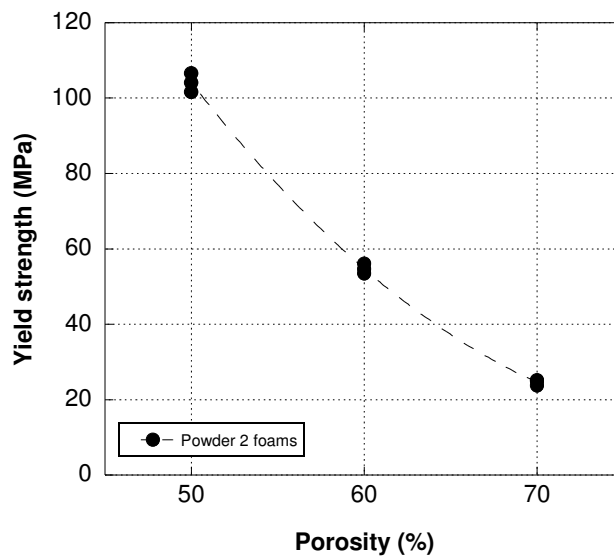


Figure 5.19. Variation of yield strength of foams as a function of porosity.

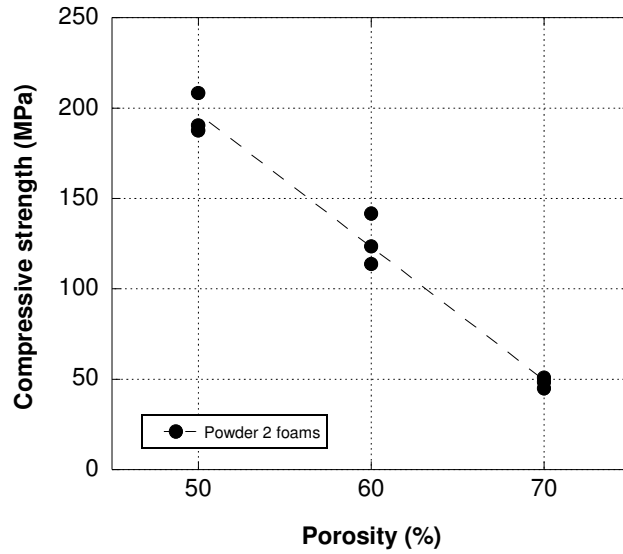


Figure 5.20. Variation of compressive strength of foams as a function of porosity.

Figure 5.21 shows the stress-strain curves of powder 2 foams sintered at 1300°C and tested at a strain rate of 10^{-1} s^{-1} . It was found that increasing strain rate slightly decreased the failure strains of foams, while it increased the elastic modulus of foams (Figure 5.22). At 10^{-3} s^{-1} strain rate 70% and 60% porous foam samples had mean elastic modulus of 1.38 and 2.21 GPa respectively, where as 50% porous foam curves were slightly higher initial slope and had 6.02 GPa elastic modulus. At 10^{-1} s^{-1} strain rate 50, 60 and 70% porous foams had 7.32, 3.84 and 2.09 GPa elastic modulus, respectively. Table 5.4 tabulates the mean elastic modulus and standard deviations of foams for different porosity and strain rate combinations.

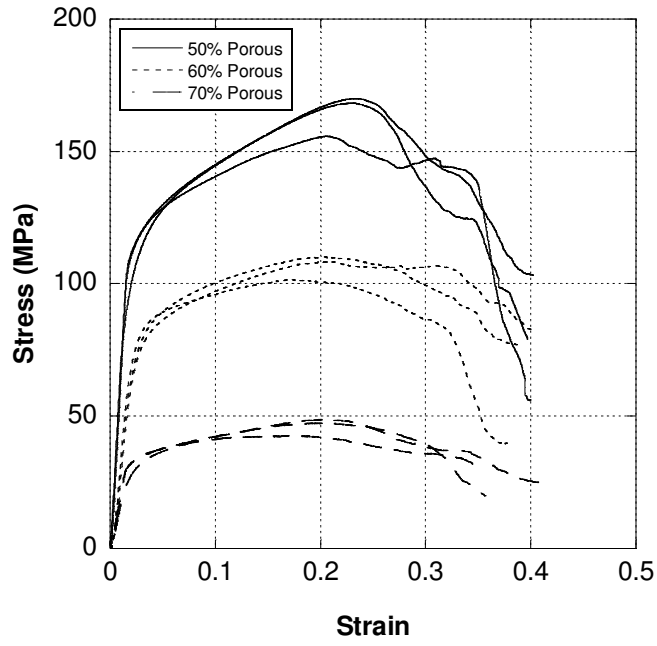


Figure 5.21. Stress-strain curves of 50, 60 and 70 % porous Powder 2 foams sintered at 1300 °C (strain rate: 10^{-1} s^{-1}).

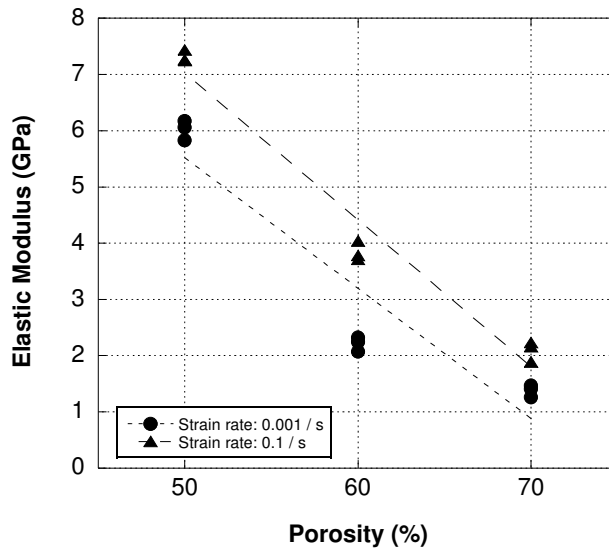


Figure 5.22. Variation of elastic modulus of foams sintered at 1300 °C as a function of porosity.

Table 5.4. Mean elastic modulus of 1300 °C sintered foams as function of Vol. % porosity and compression strain rate.

| Strain Rate ($1/s^{-1}$) | Porosity (Vol.%) | Mean Modulus (GPa) | Std. Dev. |
|----------------------------|------------------|--------------------|-----------|
| 0.001 | 50 | 6.02 | 0.173 |
| | 60 | 2.21 | 0.127 |
| | 70 | 1.38 | 0.108 |
| 0.1 | 50 | 7.32 | 0.107 |
| | 60 | 3.84 | 0.174 |
| | 70 | 2.09 | 0.180 |

5.4.2 Failure Mechanism of Foams

The deformation regions of the tested foams are shown in Figure 5.23. The foams were elastically deformed until about yield strength in the Region I. The plastic deformations of the foams proceeded in region II (Figure 5.23). The foam samples were failed in at and/or before maximum stress or compressive strength. The deformation presumably started to become non-uniform as two conic shear bands began to develop along the diagonal axes of the compact, at 45° to the loading direction (Region III) as shown in Figure 5.24. The failures of foams continued with the separation and/or tearing of the contact zones between the spherical particles (Figure 5.26). The complete failure occurred right after the separation of all bonded particles on the shear bands, starting from the corners of the cylindrical samples (Figure 5.24 d)).

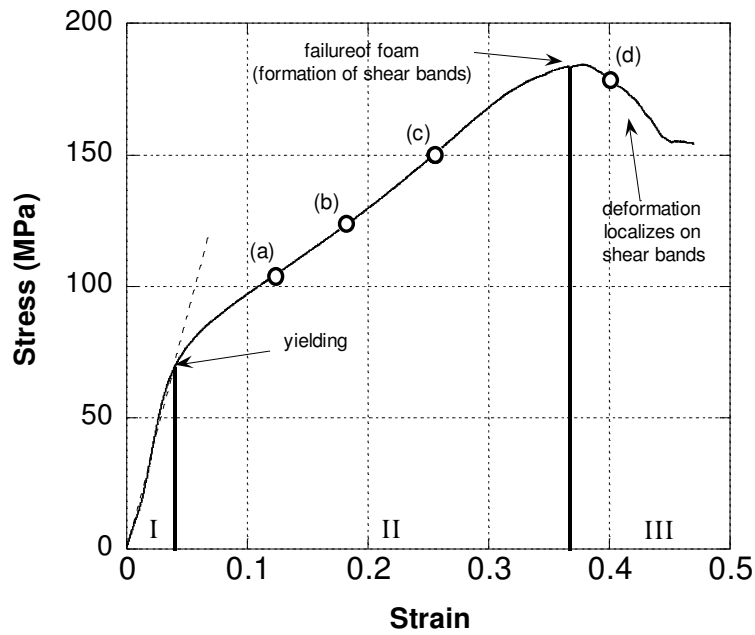


Figure 5.23. Compression stress strain curve of 60% porous Powder 2 foam sintered at 1350 °C showing deformation regions.

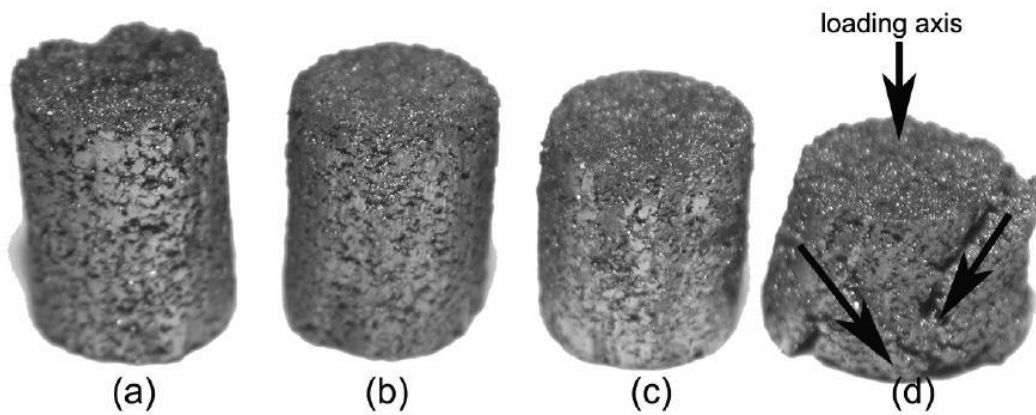


Figure 5.24. Deformed samples of Powder 2 foams sintered at 1350 °C; strains a) 0.12, b) 0.18, c) 0.26 and d) 0.4.

During the compression deformation of the foam structure, some originally non-contacting particles developed contacts with the neighboring particles as marked by arrows in Figure 5.25 a). Under compression the contact area of the particle increased and the spherical particles become elliptical. Particles were also observed to move relative to each other under the action of shear stresses (Figure 5.25 b)). The relative movement of bonding particles produced cracks at the interparticle bonding region

(Figure 5.25 c)), resulting in the separation of the particles at the sintering neck regions and the decreased of the foam strength (Figure 5.25 d)).

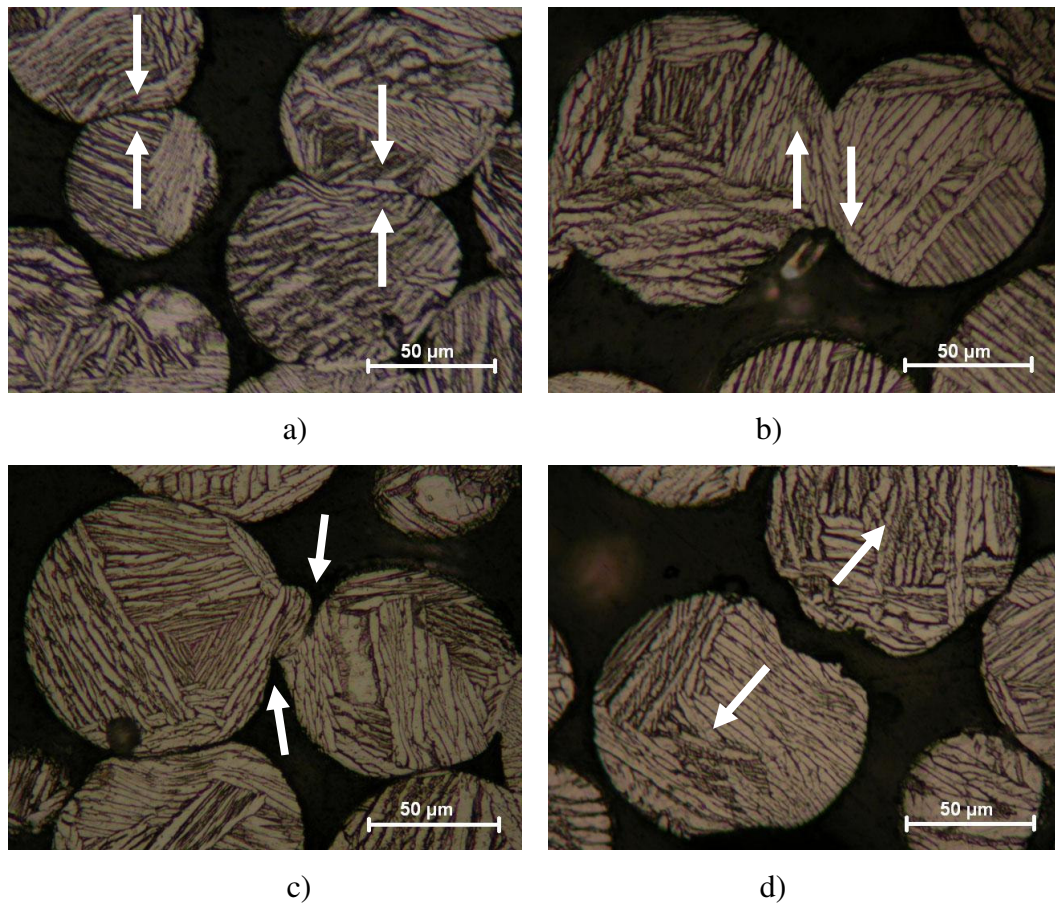


Figure 5.25. Optical micrographs showing; a) development of contacts between non-contacting particles, b) relative movement of bonded particles, c) crack propagation in bonding regions and d) separation of bonded particles.

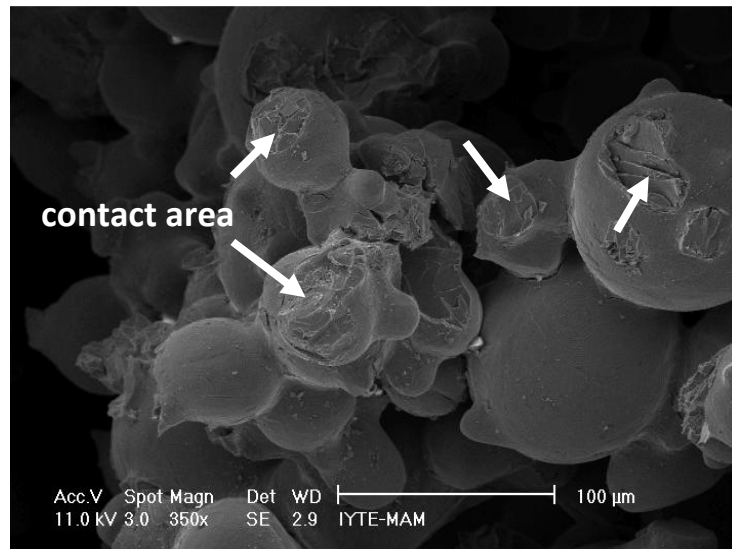
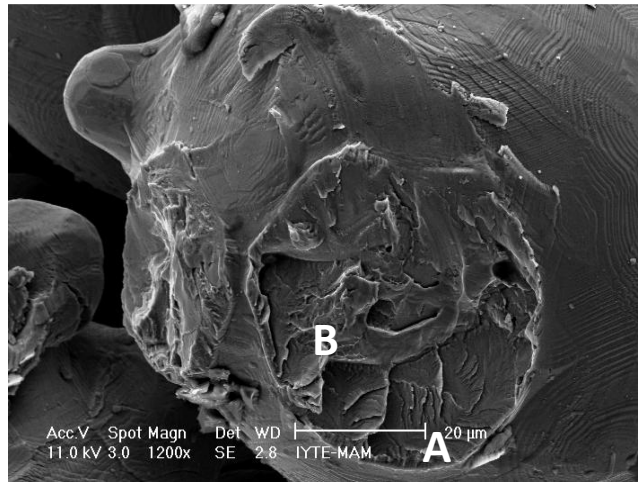
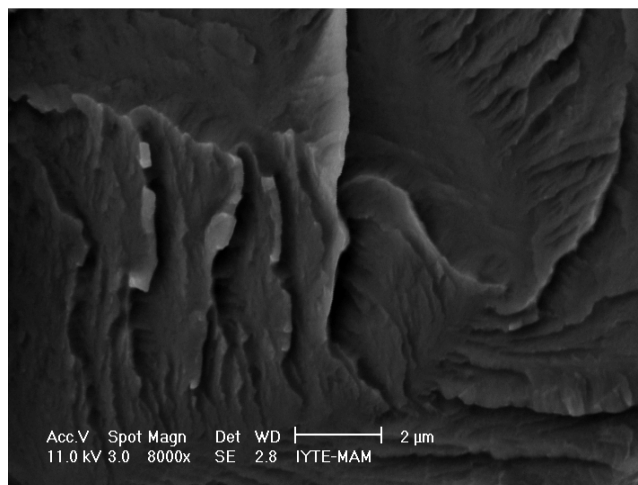


Figure 5.26. SEM micrograph of failed and separated sections of Powder 2 foam sample sintered at 1350 °C, showing debonded particles.

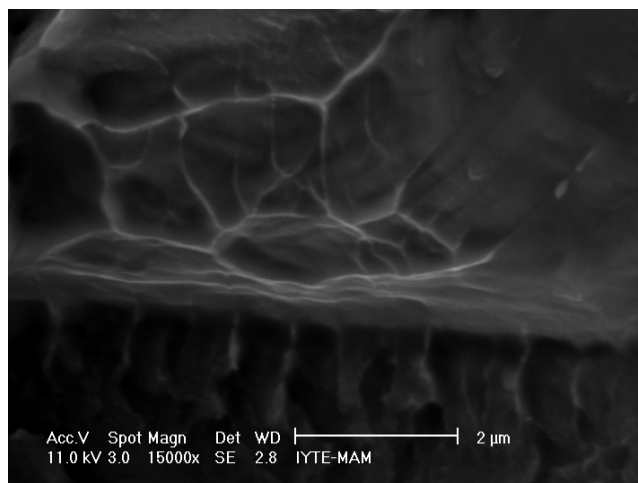
A close inspection on magnified images of debonded Ti6Al4V particles is shown in Figure 5.27 a). Debonded region differentiated two different modes of interparticle separation. In region A of Figure 5.27 a), the fracture was brittle, comprising river patterns (Figure 5.27 b)), while the separation in region B of Figure 27 a) was proceeding with the ductile fracture mode, consisting of dimples (Figure 27 c)).



a)



b)



c)

Figure 5.27. SEM micrograph of failed and separated sections of Powder 2 foam sample sintered at 1350 °C, a) the different fracture modes in region A and B, b) brittle fracture in region A and c) ductile fracture in region B.

5.5. Design of the Spinal Cages

In initial step of design procedure, the restrictions and design basis were decided. Images of vertebra segment with a reference ruler were taken to perpendicular on the disc surface and used as major design inputs. By the help of the ruler, calculations of real distance-pixel on the image ratios were performed. By using image processor software, place and rough drafts of spinal cage designs were done on the vertebral disc sections. The disc region of the vertebrae was colored with blue as seen in Figure 5.28. Dimensional conversions of the blue areas were calculated using real distance-pixel ratio of the corresponding image and they converted into defined drawing contours (Figure 5.29 a) and b)). According to contours solid models of each segment were created using 3D design software. By using computer drawing software 2D technical drawings of each spinal cage were composed. Solid models and technical drawings of each spinal cage were attached in the appendix B.

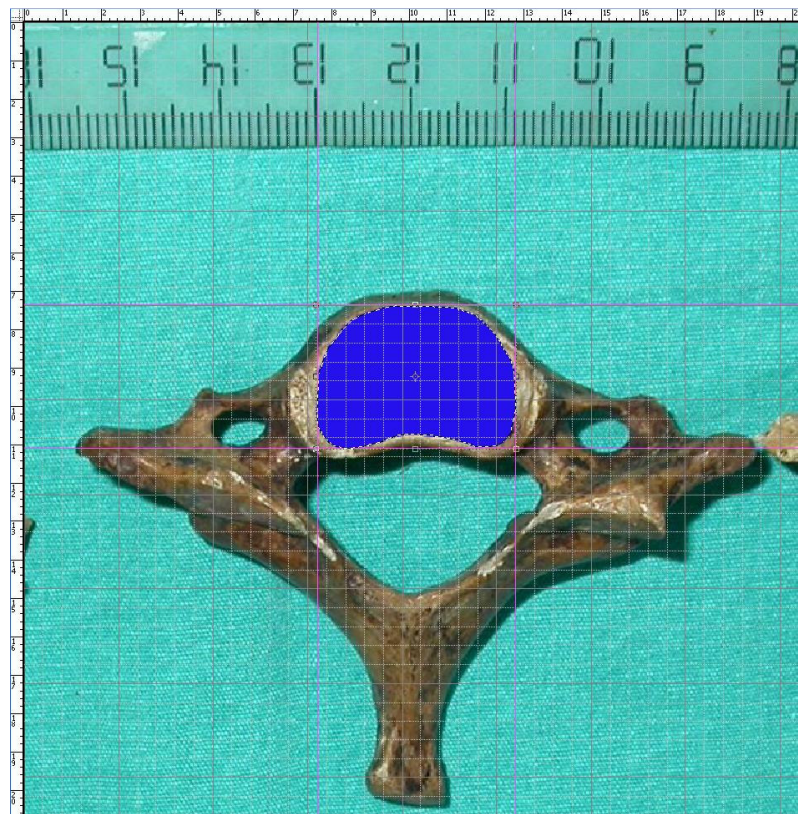


Figure 5.28. Draft of C7 coded spinal cage indicated in blue color. (Big grids indicates 10×10 mm and smaller grids indicates 2×2 mm squares)

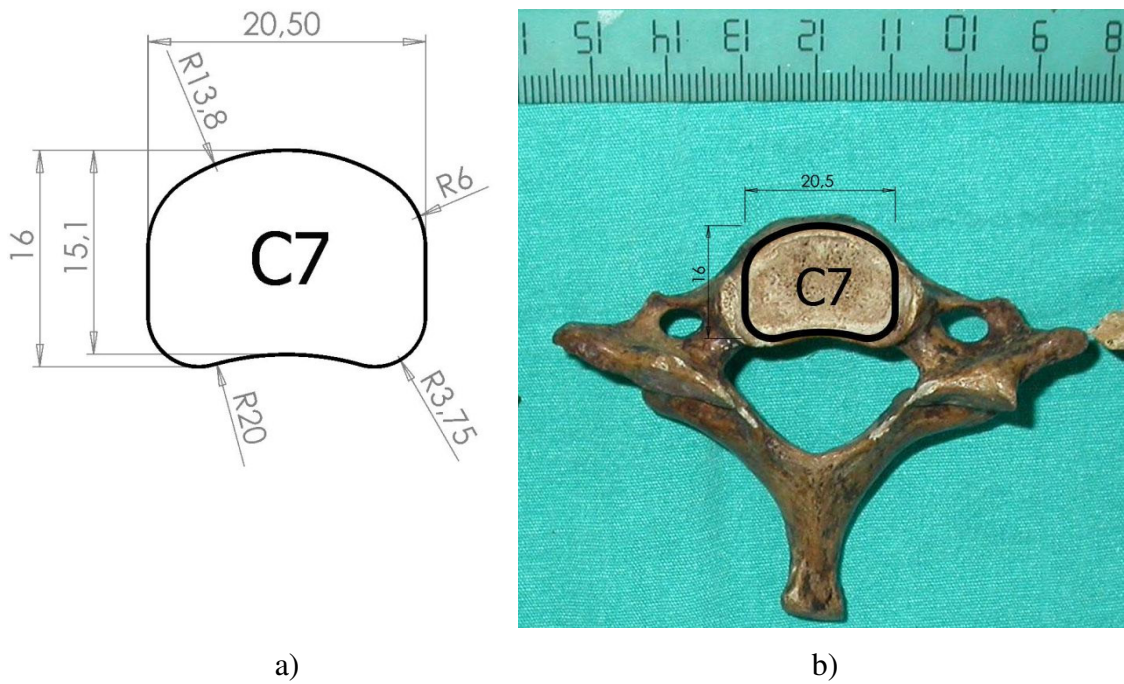


Figure 5.29. a) Defined sketch of C7 spinal cage and b) verification of dimensions.

Some consecutive segments were found to be very much similar in shape, so some cage designs were combined to be valid for more than one vertebra segment. For example; lumbar 4th and 5th (L4-L5) segments has the same design but the thickness of the cages vary (Figure 5.30).

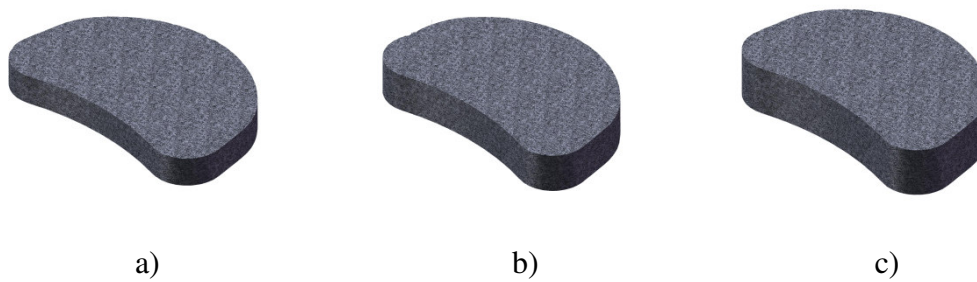


Figure 5.30. L4-L5 (Lumbar 4th and 5th) spinal cage designs in thickness of a) 6 mm, b) 8 mm and c) 10 mm.

In the final stage of designing of spinal cages, 40 x 40 mm Ti6Al4V foam plates were cut in respect of design drawings by water-jet and spinal cages extracted from simple geometry foam (Figure 5.31). Manufacturing bigger Ti6Al4V foams structures and cutting them would increase efficiency of this process since mounting of the small sample size to the water jet machine was time consuming. Cost of manufacturing big steel die and necessity of high capacity compression machine which was able to apply more than 300 kN precisely limited the producing of foam plates in 40 x 40 mm dimensions.



Figure 5.31. C7 coded spinal cage a) 3D model and b) processed sample.

The alternative way of preparation of spinal cages was using specific steel compaction die in net shape for each design. This method requires higher compaction die investment and also results in higher dimensional tolerances in final shape, as sintering operation slightly changes the dimensions compared to the green compacts. Figure 5.32 a) and b) show fabricated spinal cages by near net shape sintering technique and water-jet cut methods. It was noted that samples cut through water jet had stronger edges which eliminates the risk of crumbling of powder particles near the sharp edges (Figure 5.33).

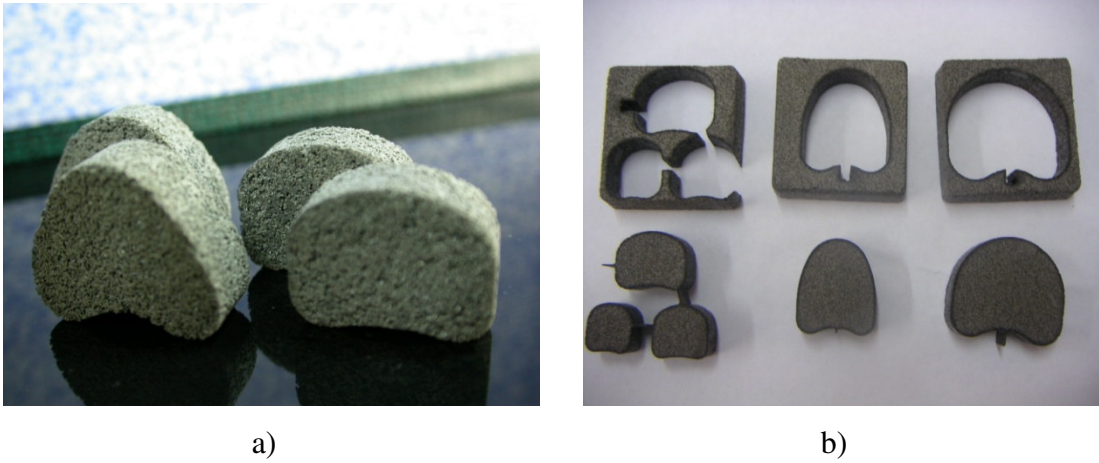


Figure 5.32. Spinal cage samples of a) direct molding and b) water jet cutting method.

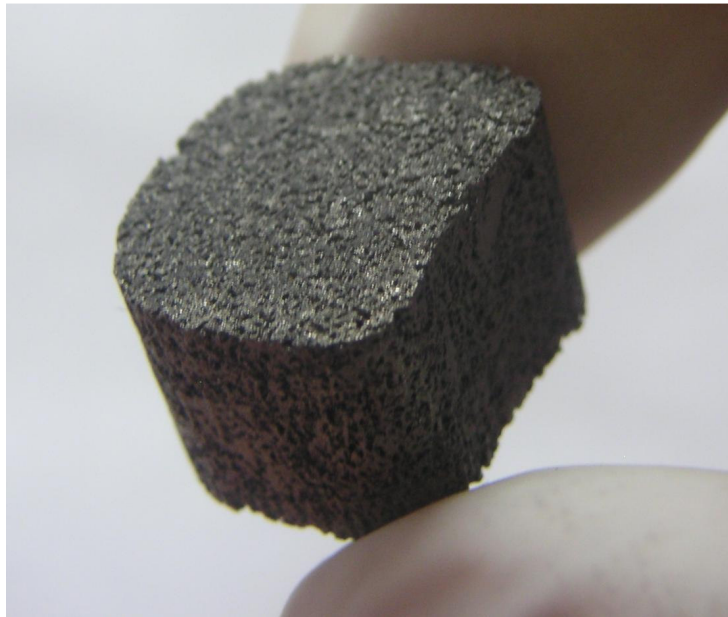


Figure 5.33. Edge sections of a sample which cut through water jet.

5.6. Comparative Analysis

In the present study, processing parameters of Ti6Al4V structure by space holder method and its effects on the compression behavior were investigated considering the similar researches in the literature and products in the biomedical market. To obtain efficient bone ingrowth into the cell structure, optimum pore size and


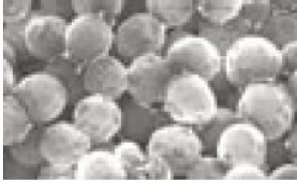



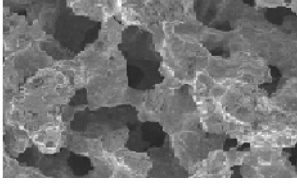
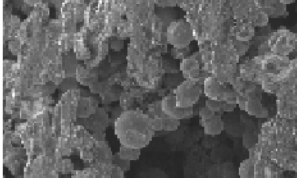
volume percent porosity were compared. In Table 5.5 basic features of porous biomedical materials that allow osseointegration (bone ingrowth) are tabulated in order to compare with the prepared Ti6Al4V foam in this study.

In this comparison, CoCr beads, Ti Fiber Mesh and Plasma Spray Coating do not have optimal pore size range as described in detail previously in bone ingrowth into porous implants section. Furthermore, CrCo beads and Plasma Spray Coating are known to not satisfy the required pore volume percent as their manufacturing processes limit the porosity up to 35%. Because of these disadvantages they only obtain bone integration limited to the implant surface rather than a complete bone ingrowth in to cell structure.

CSTi, Trabecular Metal and Actipore offer more optimized bone ingrowth conditions. CSTi and Trabecular Metal implants have been successfully implanted to human as acetabular component in hip replacement operations and as tibial base plate in total knee replacement operations. In these operations they obtain higher bone ingrowth and implant fixation. Among them, only Actipore has been used in spinal surgery as spinal fusion device. It offers advanced bone fusion and fixation in spinal disc replacement operation.

Although there have been some researches on biomedical usage of Ti6Al4V porous structures, none of porous structures available in the market is made of Ti6Al4V alloy. Ti6Al4V foam spinal cages have similar pore structure and porosity with successful biomedical porous structures. Main difference is based on manufacturing of a different material, which is also satisfies the biomedical implantation requirements. Being made of Ti6Al4V and processing by a simpler process compared with other products in market, it has lower manufacturing cost.

Table 5.5. Comparison of Ti6Al4V foams to the other porous structured biomedical materials.

| | | | | | | |
|---|---|---|--|---|---|---|
|  |  |  |  |  |  |  |
| CSTi | CoCr Breads | Ti Fiber Mesh | Plasma Spray | Trabecular Metal | ActiPore | Ti6Al4V Foam |
| Centerpulse | Howmedics Osteonics J&J Depuy | Zimmer | Biomet | Zimmer | Biorthex | IYTE |
| Pore Size | 400-600 μm | - | variable | 300 μm | 200-500 μm | 300-500 μm |
| Pore Volume | 50-60% | 68% | variable | 70% | 65% | 60% |
| Material | Ti | Ti | Ti | Ta | TiNi | Ti6Al4V |

CHAPTER 6

CONCLUSION

In this experimental study, the processing and design parameters of porous spinal cages based on Ti6Al4V foam metal were investigated. Ti6Al4V foams were prepared using space holder method. The effect of process parameters on the compression mechanical behavior was determined. Microstructural analysis of the prepared foams was performed using optical and SEM techniques. The foams with optimum pore size and porosity for bone ingrowth were used to design spinal cages. Spinal cages were designed for each vertebra segment and the cages with the designed geometries were cut from Ti6Al4V foam plates through water jet cutting. The results showed that the designed spinal cages with foam structure can be used as a fusion device in biomedical applications. The followings can be concluded;

1. Since the decomposition of ammonium bicarbonate completed at relatively low temperature, its use as space holding material was found to be more appropriate than urea.
2. The sintering process of Ti6Al4V particles changed the microstructure from needle-like α phase to Widmanstätten structure.
3. As the sintering temperature increased, the formation of TiO₂ presumably on the surfaces of the particles was found to intensify, leading to increased oxygen level in the sintered foams.
4. The resulting cellular structure of foams was found to show bimodal pore size distribution: macro pores (300-500 μm) resulted from space holder removal and micro pores (1-30 μm) due to incomplete sintering of the spherical particles.
5. Compression tests showed that increasing sintering temperature increased the elastic modulus, yield and compressive strength and failure strain of the foams.
6. Increasing strain rate in compression tests slightly decreased the failure strains of the foams, while it increased the elastic modulus values.

7. Powder 2 foams showed higher compression strength as compared with Powder 1 foams. The improvements in the mechanical properties of Powder 2 foams were attributed to the increased number of sintering necks and contact areas between the particles.

8. Ti6Al4V foams failed in a plane of 45° to the loading axis in shear bands. In failure process noncontacting particles developed contacts with other particles and bonded particles produced cracks at the interparticle bonding regions or were completely separated.

9. Separated particle sintering neck regions showed both brittle and ductile mode of fracture.

10. The mechanical properties of 60% porous Powder 2 foams sintered at 1350 °C were found to satisfy the requirements for bone replacements. The elastic modulus was found to be closer to the elastic modulus of human bone (1-20 GPa), leading to reduced elastic mismatch between implant and bone and therefore implant loosening.

11. Although, the mechanical properties of 50% porous Powder 2 foams were also found to satisfy the strength requirements of bone replacement, however the porosity level did not satisfy optimum bone ingrowth conditions.

12. Shaping through water jet cutting was found to result in finer dimensional tolerances and stronger edges of the foams as compared with direct near net shape sintering.

REFERENCES

- Agrawal, C. 1998. Reconstructing the human body using biomaterials. *JOM Journal of the Minerals, Metals and Materials Society* 50 (1):31-35.
- Assad, M., A. V. Chernyshov, P. Jarzem, M. A. Leroux, C. Coillard, S. Charette, and C. H. Rivard. 2003. Porous titanium-nickel for intervertebral fusion in a sheep model: Part 2. Surface analysis and nickel release assessment. *Journal of Biomedical Materials Research Part B-Applied Biomaterials* 64B (2):121-129.
- Assad, M., P. Jarzem, M. A. Leroux, C. Coillard, A. V. Chernyshov, S. Charette, and C. H. Rivard. 2003. Porous titanium-nickel for intervertebral fusion in a sheep model: Part 1. Histomorphometric and radiological analysis. *Journal of Biomedical Materials Research Part B-Applied Biomaterials* 64B (2):107-120.,
- Augustin, C., and W. Hungerbach. 2009. Production of hollow spheres (HS) and hollow sphere structures (HSS). *Materials Letters* 63 (13-14):1109-1112.
- Banhart, J. 2001. Manufacture, characterisation and application of cellular metals and metal foams. *Progress in Materials Science* 46 (6):559-U3.
- Barth, E., H. Ronningen, L. F. Solheim, and B. Saethren. 1986. Bone Ingrowth into Weight-Bearing Porous Fiber Titanium Implants - Mechanical and Biochemical Correlations. *Journal of Orthopaedic Research* 4 (3):356-361.
- Bloebaum, R. D., K. N. Bachus, N. G. Mombberger, and A. A. Hofmann. 1994. Mineral Apposition Rates of Human Cancellous Bone at the Interface of Porous-Coated Implants. *Journal of Biomedical Materials Research* 28 (5):537-544.
- Bobyn, J. D., R. M. Pilliar, H. U. Cameron, and G. C. Weatherly. 1980. The Optimum Pore-Size for the Fixation of Porous-Surfaced Metal Implants by the Ingrowth of Bone. *Clinical Orthopaedics and Related Research* (150):263-270.
- Bobyn, J. D., G. J. Stackpool, S. A. Hacking, M. Tanzer, and J. J. Krygier. 1999. Characteristics of bone ingrowth and interface mechanics of a new porous tantalum biomaterial. *J Bone Joint Surg Br* 81 (5):907-14.
- Bobyn, 1999. Characteristics of bone ingrowth and interface mechanics of a new porous tantalum biomaterial. *Journal of Bone and Joint Surgery-British Volume* 81B (5):907-914.
- Bobyn, J.D., and J.E. Miller. 1994. Features of biologically fixed devices. *Orthopaedic Basic Science, American Academy of Orthopaedic Surgeons, Chicago*

- Bobyn JD, Cameron HU, Abdulla D, Pilliar RM, and Weatherly GC. 1982. Biologic fixation and bone modeling with an unconstrained canine total knee prosthesis. *Clinical Orthop Relat Res* 166:301-312.
- Bram, M., C. Stiller, H. P. Buchkremer, D. Stover, and H. Baur. 2000. High-porosity titanium, stainless steel, and superalloy parts. *Advanced Engineering Materials* 2 (4):196-199.
- British Columbia 2003. Ossification, Bone Formation, Growth and Repair. <http://commons.bcit.ca/biology/ossification/index.html> (accessed May, 2009).
- Cameron, H. U., R. M. Pilliar, and I. Macnab. 1976. Rate of Bone Ingrowth into Porous Metal. *Journal of Biomedical Materials Research* 10 (2):295-302.
- Cameron H. U., R. M. Pilliar, I. Macnab. 1976. The rate of bone ingrowth into porous metal. *J Biomed Mater Res* (10(2)):295-302.
- Cestero, H. J., K. E. Salyer, and I. R. Toranto. 1975. Bone-Growth into Porous Carbon, Polyethylene, and Polypropylene Prostheses. *Journal of Biomedical Materials Research* 9 (4):1-7.
- Chen, L. B., X. B. Jiang, and L. Yang. 2004. Differentiation of rat marrow mesenchymal stem cells into pancreatic islet beta-cells. *World J Gastroenterol* 10 (20):3016-20.
- Clemow, A. J. T., A. M. Weinstein, J. J. Klawitter, J. Koeneman, and J. Anderson. 1981. Interface Mechanics of Porous Titanium Implants. *Journal of Biomedical Materials Research* 15 (1):73-82.
- Cook, S. D., K. A. Walsh, and R. J. Haddad. 1985. Interface Mechanics and Bone-Growth into Porous Co-Cr-Mo Alloy Implants. *Clinical Orthopaedics and Related Research* (193):271-280.
- Dunand D. C. 2004. Processing of Titanium Foams. *Advanced Engineering Materials* 6 (6):369-376.
- Ducheyne, Paul, and Marc Martens. 1986. Orderly oriented wire meshes as porous coatings on orthopaedic implants I: Morphology. *Clinical Materials* 1 (1):59-67.
- Eidelson, S.G. 2002. Minimally Invasive and Open Surgery Procedures Minimally Invasive Spine Surgery: Part 1. <http://www.spineuniverse.com/displayarticle.php/article2002.html> (accessed May 2009)
- Eugene W. White, Jon N. Weber, Della M. Roy, Edwin L. Owen, Richard T. Chiroff, Rodney A. White,. 1975. Replamineform porous biomaterials for hard tissue implant applications. *Journal of Biomedical Materials Research* 9 (4):23-27.
- Galante, J., and W. Rostoker. 1973. Fiber Metal Composites in Fixation of Skeletal Prosthesis. *Journal of Biomedical Materials Research* 7 (3):43-61.

- Galante, Jorge, William Rostoker, Roger Lueck, And Robert D. Ray. 1971. Sintered Fiber Metal Composites as a Basis for Attachment of Implants to Bone. *J Bone Joint Surg Am* 53 (1):101-114.
- Guden, M., E. Celik, E. Akar, and S. Cetiner. 2005. Compression testing of a sintered Ti6Al4V powder compact for biomedical applications. *Materials Characterization* 54 (4-5):399-408.
- H. Hahn, W. Palich. 1970. Preliminary evaluation of porous metal surfaced titanium for orthopedic implants. *Journal of Biomedical Materials Research* 4 (4):571-577.
- Head, W. C., D. J. Bauk, and R. H. Emerson. 1995. Titanium as the Material of Choice for Cementless Femoral Components in Total Hip-Arthroplasty. *Clinical Orthopaedics and Related Research* (311):85-90.
- Hofmann, A. A., R. D. Bloebaum, and K. N. Bachus. 1997. Progression of human bone ingrowth into porous-coated implants - Rate of bone ingrowth in humans. *Acta Orthopaedica Scandinavica* 68 (2):161-166.
- Itala, A. I., H. O. Ylanen, C. Ekholm, K. H. Karlsson, and H. T. Aro. 2001. Pore diameter of more than 100 μ m is not requisite for bone ingrowth in rabbits. *Journal of Biomedical Materials Research* 58 (6):679-683.
- Nilles, J. L., M. T. Karagianes, K. R. Wheeler,. 1974. Porous titanium alloy for fixation of knee prostheses. *Journal of Biomedical Materials Research* 8 (4):319-328.
- Joel, S., Hirschhorn, Andrew A. McBeath, Manek R. Dustoor,. 1971. Porous titanium surgical implant materials. *Journal of Biomedical Materials Research* 5 (6):49-67.
- Klawitter, J. J., J. G. Bagwell, A. M. Weinstein, B. W. Sauer, and J. R. Pruitt. 1976. Evaluation of Bone-Growth into Porous High-Density Polyethylene. *Journal of Biomedical Materials Research* 10 (2):311-323.
- Korner, C., and R. F. Singer. 2000. Processing of metal foams - Challenges and opportunities. *Advanced Engineering Materials* 2 (4):159-165.
- Laptev, A., M. Bram, H. P. Buchkremer, and D. Stover. 2004. Study of production route for titanium parts combining very high porosity and complex shape. *Powder Metallurgy* 47 (1):85-92.
- Li, Bing-Yun, Li-Jian Rong, Yi-Yi Li, and V. E. Gjunter. 2000. A recent development in producing porous Ni-Ti shape memory alloys. *Intermetallics* 8 (8):881-884.
- Li, J. P., S. H. Li, K. de Groot, and P. Layrolle. 2002. Preparation and characterization of porous titanium. *Bioceramics* 14 218-2:51-54.

- Likibi, F., G. Chabot, M. Assad, C. Coillard, M. A. Leroux, and C. H. Rivard. 2004. Effect of implant structure on bone apposition and integration: Comparative study of two posterior lumbar fusion devices. *50th Annual Meeting of the Orthopaedic Research Society, San Francisco, CA, USA.*
- Long, Marc, and H. J. Rack. 1998. Titanium alloys in total joint replacement--a materials science perspective. *Biomaterials* 19 (18):1621-1639.
- Mader, Sylvia S. 2005. *Understanding Human Anatomy & Physiology, 5/e*: The McGraw-Hill.
- Marieb, E. N. 1998. Human Anatomy & Physiology, edited by Menlo Park. *California: Benjamin/Cummings Science Publishing.*
- Markaki, A. E., and W. C. Trevor. 2005. Magneto-mechanical bone growth stimulation by actuation of highly porous ferromagnetic fiber arrays. *Biomedical Applications of Micro- and Nanoengineering II* 5651: 61-67
- Martell, J. M., R. H. Pierson, J. J. Jacobs, A. G. Rosenberg, M. Maley, and J. O. Galante. 1993. Primary Total Hip Reconstruction with a Titanium Fiber-Coated Prosthesis Inserted without Cement. *Journal of Bone and Joint Surgery-American Volume* 75A (4):554-571.
- Martens, M., P. Ducheyne, P. Demeester, and J. C. Mulier. 1980. Skeletal Fixation of Implants by Bone Ingrowth into Surface Pores. *Archives of Orthopaedic and Trauma Surgery* 97 (2):111-116.
- Melikyan, M. L., and V. I. Itin. 2002. Dynamics of bone tissue mineralization in porous titanium and the mechanical properties of a titanium-bone tissue composite. *Technical Physics Letters* 28 (8):673-674.
- Murray, N. G. D., and D. C. Dunand. 2003. Microstructure evolution during solid-state foaming of titanium. *Composites Science and Technology* 63 (16):2311-2316.
- Nathan M, Pope M H, Grobler L J. 1994. Osteophyte formation in the vertebral column: a review of the etiologic factors--Part II.. *Contemp Orthop.* 29 (2):113-9.
- Nather, Aziz, H.J.C. Ong, and Zameer Aziz. 1998. Structure of Bone. http://www.worldscibooks.com/medsci/etextbook/5695/5695_chap01.pdf (accessed in May, 2009)
- Oh, I. H., N. Nomura, N. Masahashi, and S. Hanada. 2003. Mechanical properties of porous titanium compacts prepared by powder sintering. *Scripta Materialia* 49 (12):1197-1202.
- Okazaki, K., W. H. Lee, D. K. Kim, and R. A. Kopezyk. 1991. Physical Characteristics of Ti-6al-4v Implants Fabricated by Electrodischarge Compaction. *Journal of Biomedical Materials Research* 25 (12):1417-1429.

- Okazaki, Yoshimitsu, Emiko Nishimura, Hiroshi Nakada, and Kihei Kobayashi. 2001. Surface analysis of Ti-15Zr-4Nb-4Ta alloy after implantation in rat tibia. *Biomaterials* 22 (6):599-607.
- Okazaki, Yoshimitsu, Sethumadhavan Rao, Tetsuya Tateishi, and Yoshimasa Ito. 1998. Cytocompatibility of various metal and development of new titanium alloys for medical implants. *Materials Science and Engineering A* 243 (1-2):250-256.
- Pillar, R. M. **21** A1 (1987),. *Porous-surfaced metallic implants for orthopaedic applications* 1987**21** A1 (1987).
- Prymak, O., D. Bogdanski, M. Koller, S. A. Esenwein, G. Muhr, F. Beckmann, T. Donath, M. Assad, and M. Epple. 2005. Morphological characterization and in vitro biocompatibility of a porous nickel-titanium alloy. *Biomaterials* 26 (29):5801-5807.
- Rhalmi, S., M. Odin, M. Assad, M. Tabrizian, C. H. Rivard, and L. H. Yahia. 1999. Hard, soft tissue and in vitro cell response to porous nickel-titanium: a biocompatibility evaluation. *Bio-Medical Materials and Engineering* 9 (3):151-162.
- Rho, Jae-Young, Liisa Kuhn-Spearing, and Peter Zioupos. 1998. Mechanical properties and the hierarchical structure of bone. *Medical Engineering & Physics* 20 (2):92-102.
- Robertson, D. M., L. S. Pierre, and R. Chahal. 1976. Preliminary-Observations of Bone Ingrowth into Porous Materials. *Journal of Biomedical Materials Research* 10 (3):335-344.
- Rothman, R. H., F.A. Simena, and P.M. Bernini. 1982. Lumbar disc disease. *The Spine*, edited by Rothman R.H. and Simone F.A., 2nd ed Philadelphia: WB Saunders:508-645.
- Ryan, G., A. Pandit, and D. P. Apatsidis. 2006. Fabrication methods of porous metals for use in orthopaedic applications. *Biomaterials* 27 (13):2651-2670.
- S. F. Hulbert, F. A. Young, R. S. Mathews, J. J. Klawitter, C. D. Talbert, F. H. Stelling., 1970. Potential of ceramic materials as permanently implantable skeletal prostheses. *Journal of Biomedical Materials Research* 4 (3):433-456.
- Sauer, B. W., Weinstein, Am, Klawitte, Jj, S. F. Hulbert, R. B. Leonard, and J. G. Bagwell. 1974. Role of Porous Polymeric Materials in Prosthesis Attachment. *Journal of Biomedical Materials Research* 8 (3):145-153.
- Schliephake, H., F. W. Neukam, and D. Klosa. 1991. Influence of Pore Dimensions on Bone Ingrowth into Porous Hydroxylapatite Blocks Used as Bone-Graft Substitutes - a Histometric Study. *International Journal of Oral and Maxillofacial Surgery* 20 (1):52-58.

- Simancik, F. 2002. *Introduction: The Strange World of Cellular Metals*. Edited by H.-P. Degischer and B. Kriszt, *Handbook of Cellular Metals: Production, Processing, Applications.*: Wiley-VCH Verlag GmbH & Co. KGaA.
- Song, Y., D. S. Xu, R. Yang, D. Li, W. T. Wu, and Z. X. Guo. 1999. Theoretical study of the effects of alloying elements on the strength and modulus of [beta]-type bio-titanium alloys. *Materials Science and Engineering: A* 260 (1-2):269-274.
- Spector, M., M. J. Michno, W. H. Smarook, and G. T. Kwiatkowski. 1978. A high-modulus polymer for porous orthopedic implants: biomechanical compatibility of porous implants. *J Biomed Mater Res* 12 (5):665-77.
- Sumner, D. R., J. M. Bryan, R. M. Urban, and J. R. Kuszak. 1990. Measuring the Volume Fraction of Bone Ingrowth - a Comparison of 3 Techniques. *Journal of Orthopaedic Research* 8 (3):448-452.
- Thieme, M., K. P. Wieters, F. Bergner, D. Scharnweber, H. Worch, J. Ndop, T. J. Kim, and W. Grill. 2001. Titanium powder sintering for preparation of a porous functionally graded material destined for orthopaedic implants. *Journal of Materials Science-Materials in Medicine* 12 (3):225-231.
- Tsuruga, E., H. Takita, H. Itoh, Y. Wakisaka, and Y. Kuboki. 1997. Pore size of porous hydroxyapatite as the cell-substratum controls BMP-induced osteogenesis. *Journal of Biochemistry* 121 (2):317-324.
- Turner, T. M., R. M. Urban, D. R. Sumner, A. K. Skipor, and J. O. Galante. 1989. Bone Ingrowth into the Tibial Component of a Canine Total Condylar Knee Replacement Prosthesis. *Journal of Orthopaedic Research* 7 (6):893-901.
- Valentine, Leonard. 2009. *Valentine Chiropractic website - Disc Problems, Degenerative Disc Disease, Bulging Discs, Herniated Discs* <http://www.valentinechiropractic.com/disc-problems.php> (accessed May, 2009)
- Weiner, S., and H. D. Wagner. 1998. The material bone: Structure mechanical function relations. *Annual Review of Materials Science* 28:271-298.
- Wen, C. E., M. Mabuchi, Y. Yamada, K. Shimojima, Y. Chino, and T. Asahina. 2001. Processing of biocompatible porous Ti and Mg. *Scripta Materialia* 45 (10):1147-1153.
- Wen, C. E., Y. Yamada, K. Shimojima, Y. Chino, T. Asahina, and M. Mabuchi. 2002. Processing and mechanical properties of autogenous titanium implant materials. *Journal of Materials Science-Materials in Medicine* 13 (4):397-401.

APPENDIX A

ASTM F1580-1 STANDARD



Designation: F 1580 – 01

Standard Specification for Titanium and Titanium-6 Aluminum-4 Vanadium Alloy Powders for Coatings of Surgical Implants¹

This standard is issued under the fixed designation F 1580; the number immediately following the designation indicates the year of original adoption or, in the case of revision, the year of last revision. A number in parentheses indicates the year of last reapproval. A superscript epsilon (ϵ) indicates an editorial change since the last revision or reapproval.

1. Scope

1.1 This specification covers the requirements for unalloyed titanium and Ti-6Al-4V alloy powders for use in fabricating coatings on titanium alloy implants.

1.2 Powders covered under this specification may be used to form coatings by sintering or thermal spraying techniques.

1.3 This specification covers powder requirements only. It does not address properties of the coatings formed from them.

2. Referenced Documents

2.1 ASTM Standards:

B 214 Test Method Sieve Analysis of Granular Metal Powders²

B 215 Practices for Sampling Finished Lots of Metal Powders²

B 299 Specification for Titanium Sponge³

E 11 Specification for Wire-Cloth Sieves for Testing Purposes⁴

E 120 Test Methods for Chemical Analysis of Titanium and Titanium Alloys⁵

F 67 Specification for Unalloyed Titanium for Surgical Implant Applications⁶

F 981 Practice for Assessment of Compatibility of Biomaterials for Surgical Implants With Respect to Effect of Materials on Muscle and Bone⁶

F 1472 Specification for Wrought Ti-6Al-4V Alloy for Surgical Implant Applications⁶

2.2 American Society for Quality (ASQ) Standards:⁷

ASQ C1 General Requirements for a Quality Program

2.3 Aerospace Material Specifications:⁸

AMS 2249 Chemical Check Analysis Limits, Titanium and Titanium Alloys

AMS 4998A Powder, 6Al-4V, Premium Quality (noncurrent)

3. Methods of Manufacture

3.1 Powders may be manufactured by the plasma rotating electrode process, inert gas atomization, hydride-dehydride, or other method capable of producing powder meeting the requirements of this specification.

4. Chemical Requirements

4.1 The chemical analysis of the powder shall conform to the requirements set forth in Table 1. Analysis shall be performed before the addition of any processing aids.

4.1.1 Requirements for the major and minor elemental constituents for unalloyed titanium and Ti-6Al-4V alloy powders are listed in Table 1. Also listed are all important residual elements. Analysis for elements not listed in Table 1 is not required to verify compliance with this specification.

4.2 The product analysis tolerance shall conform to the requirements set forth in Table 2.

4.3 For referee purposes, Test Methods E 120 shall be used.

4.4 Intentional elemental additions other than those specified in Table 1 are not permitted.

4.5 For powder that includes particle size fractions finer than 200 mesh (74 μm), the oxygen content limits shall be agreed upon between buyer and seller.

5. Particle Size and Shape

5.1 Powder shall be sieved to the customer's requirements with stainless steel screens conforming to Specification E 11. Analysis of sieved powder for conformance to the customer's particle size range requirements shall be in accordance with Test Method B 214.

5.2 Powder made from the plasma rotating electrode process and inert gas atomization tends to be spherical in shape, powder made from the hydride-dehydride process tends to be

¹ This specification is under the jurisdiction of ASTM Committee F04 on Medical and Surgical Devices and is under the direct responsibility of Subcommittee F04.12 on Metallurgical Materials.

Current edition approved October 10, 2001. Published January 2002. Originally published as F 1580 - 95. Past previous edition F 1580 - 95¹.

² Annual Book of ASTM Standards, Vol 02.05.

³ Annual Book of ASTM Standards, Vol 02.04.

⁴ Annual Book of ASTM Standards, Vol 14.02.

⁵ Annual Book of ASTM Standards, Vol 03.05.

⁶ Annual Book of ASTM Standards, Vol 13.01.

⁷ Available from the American Society for Quality, 600 N. Plankinton Ave., Milwaukee, WI 53203.

⁸ Available from Society of Automotive Engineers, 400 Commonwealth Dr., Warrendale, PA 15096-0001.

TABLE 1 Chemical Requirements

| Element | Unalloyed Ti Powder Weight Percent | | Ti-6Al-4V Powder Weight Percent | |
|---------|---------------------------------------|-------------------|------------------------------------|-------|
| | Min | Max | Min | Max |
| Al | | | 5.50 | 6.75 |
| V | | | 3.50 | 4.50 |
| O | | 0.40 | | 0.20 |
| Fe | | 0.50 | | 0.30 |
| C | | 0.10 | | 0.08 |
| H | | 0.05 | | 0.015 |
| N | | 0.05 | | 0.05 |
| Cu | | | | 0.10 |
| Sn | | | | 0.10 |
| Si | | 0.04 | | |
| Cl | | 0.20 ^A | | |
| Na | | 0.19 ^A | | |
| Ti | balance ^B | | balance ^B | |

^A Lower maximum chlorine and sodium contents may be agreed upon between buyer and seller.

^B The percentage of titanium is determined by difference and need not be measured.

TABLE 2 Product Analysis Tolerances^A

| Element | Variation Under Min or Over Max |
|----------|---------------------------------|
| Aluminum | 0.04 |
| Vanadium | 0.015 |
| Oxygen | 0.03 ^B |
| Oxygen | 0.02 ^C |
| Iron | 0.10 |
| Hydrogen | 0.002 |
| Carbon | 0.02 |
| Nitrogen | 0.02 |
| Copper | 0.05 |
| Tin | 0.15 |
| Silicon | 0.02 |

^ARefer to AMS 2249.

^BFor unalloyed Ti powder.

^CFor Ti-6Al-4V alloy powder.

angular in shape and sponge powder tends to be irregular in shape.

6. Cleanliness

6.1 Powder shall be handled at all times so as to ensure freedom from contamination with nonmetallic materials or other metal alloy powders or both.

6.2 Powder cleanliness shall be determined by examining a representative sample, per Practices B 215 or as agreed upon

between buyer and seller, comprising at least 1 in.²(6.45 cm²) of a closely packed mono-layer of powder per lot at 20× magnification. No foreign material shall be visible under these conditions. Powder cleanliness shall be determined before the addition of any processing aids.

7. Special Requirements

7.1 Various materials known as processing aids may be added to the powder to provide enhanced processibility. The powder supplier shall identify the chemical composition and weight percentage of any added processing aids on the material certification.

7.2 Processing aids shall have no detrimental effect on the corrosion resistance or biocompatibility of the final coating.

NOTE 1—Finely divided titanium powder may be considered pyrophoric and should be handled in accordance with the appropriate guidelines in the Material Safety Data Sheet.

8. Certification

8.1 Powder shipped under this specification shall be accompanied by certification that includes:

8.1.1 ASTM designation and date of issue.

8.1.2 Quantity (weight).

8.1.3 Method of manufacture.

8.1.4 Chemical analysis per 4.1.

8.1.5 Sieve analysis per 5.1.

8.1.6 Powder cleanliness per 6.2.

8.1.7 Special requirement per 7.2.

8.1.8 Other requirements.

9. Quality Program Requirements

9.1 The producer shall maintain a quality program, such as that defined in the ASQ C1, for example.

9.2 The manufacturer of surgical implants shall be ensured of the producer's quality program for conformance to the intent of ASQ C1 or other recognized programs.

10. Keywords

10.1 coatings; metallic; metals (for surgical implants titanium alloys); orthopaedic medical devices (titanium/titanium alloys); powder; porous coatings; titanium/titanium alloys (for surgical implants)

APPENDICES

(Nonmandatory Information)

XI. RATIONALE

XI.1 Coatings formed from metallic powders have become widely used as a means of improving tissue attachment to uncemented orthopedic joint prosthesis. Such coatings have also been demonstrated to improve bonding of acrylic cement to prostheses. The method used to create the coatings can determine which powder size and shape is suitable for the specific application. Not all powder sizes or shapes are applicable for all coating processes.

XI.2 Chemical composition limits for O, Fe, C, and N in the unalloyed grade are taken from Specification F 67, Grade 4. Limits for Si, Cl, H, and Na are taken from Specification B 299, Grade SL.

XI.3 Chemical composition limits for Al, V, O, Fe, C, H, and N in the Ti-6Al-4V grade are taken from Specification F 1472. Limits for Cu and Sn are taken from AMS 4998.

X1.4 Product analysis tolerances are taken directly from AMS 2249. No recognized product analysis tolerances currently exist specifically for Cl or Na in titanium alloys.

X1.5 Processing aids are frequently used to facilitate powder processing and application of porous coatings to implant surfaces. It is beyond the scope of this specification to identify suitable processing aids or define their use. It is the responsibility of the implant manufacturer to ensure that any processing aid or residue of a processing aid has no detrimental effect on biocompatibility or coating properties.

X1.6 It should be recognized that the heat treatments used to form porous coatings can create microstructures that are substantially different from wrought titanium alloys. Porous coated implants also exhibit much greater surface area than monolithic implants. For these reasons, the biocompatibility and corrosion behavior must be characterized on finished coatings.

X1.7 Likewise, these heat treatments can create microstructures that give substantially different corrosion fatigue behavior from that of typical wrought titanium alloys. Corrosion fatigue behavior must be evaluated on finished coated substrates.

X1.8 Pore size and morphology are important factors influencing tissue ingrowth and acrylic penetration of porous coatings. Particle size, size distribution, and shape are critical to controlling the pore size and morphology in the final

coating. Particle size and size distribution are conventionally controlled by screening. The referenced ASTM International standards allow comparison of powder to a manufacturer's specifications for a given coating process. A number of methods to characterize particle shape exists. The coating manufacturer should select a means of particle shape characterization suitable for his process.

X1.9 This specification requires sampling for particle size and powder cleanliness on each powder lot. In some cases, sampling on each shipping container of powder may be appropriate.

X1.10 Other process parameters are also critical to determining final pore size and morphology in the final coating. Because these parameters are not directly related to the chemical and physical characteristics of the starting powder, they are not addressed in this specification.

X1.11 The requirements for powder cleanliness ensure freedom from contaminants that might adversely affect either the biocompatibility or the finished coatings or the ability to bond the coating properly during manufacturing. The method in 6.2 (Practices B 215) is commonly used for relatively coarse spherical powders used to fabricate sintered porous coatings. Other types of powders may require different methods for cleanliness characterization. The development and implementation of such methods are the responsibility of the implant manufacturer.

X2. BIOCOMPATIBILITY

X2.1 The biocompatibility of metallic implants is a direct function of their composition. The alloy compositions covered by this specification have been used in the wrought form for surgical implants and have been used successfully in human implant applications in contact with soft tissue and bone for over a decade. Because of the well characterized level of biological response exhibited by these alloys, they have been used as a control material in Practice F 981.

X2.2 No known surgical implant material has ever been shown to be completely free from adverse reactions in the human body. Long-term clinical experience of the use of the material referred to in this specification, however, has shown that an acceptable level of biological response can be expected, if the material is used in appropriate applications.

SUMMARY OF CHANGES

(1) Added 6.2 concerning particle shape, eliminated Section 3 and renumbered document, and added X1.1 in which powder shape and application is addressed.

(2) Editorial corrections have been made to meet terminology and formatting guidelines established for implant material standards.

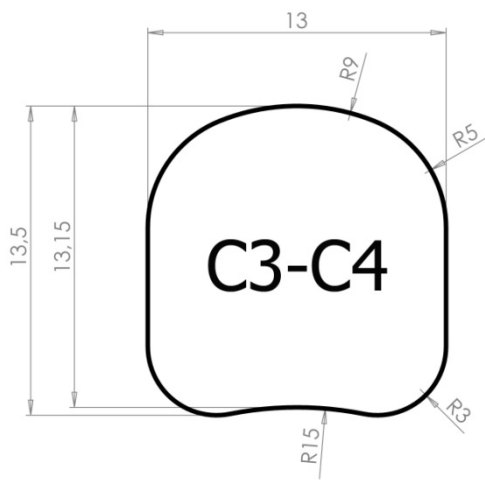
ASTM International takes no position respecting the validity of any patent rights asserted in connection with any item mentioned in this standard. Users of this standard are expressly advised that determination of the validity of any such patent rights, and the risk of infringement of such rights, are entirely their own responsibility.

This standard is subject to revision at any time by the responsible technical committee and must be reviewed every five years and if not revised, either reapproved or withdrawn. Your comments are invited either for revision of this standard or for additional standards and should be addressed to ASTM International Headquarters. Your comments will receive careful consideration at a meeting of the responsible technical committee, which you may attend. If you feel that your comments have not received a fair hearing you should make your views known to the ASTM Committee on Standards, at the address shown below.

This standard is copyrighted by ASTM International, 100 Barr Harbor Drive, PO Box C700, West Conshohocken, PA 19428-2959, United States. Individual reprints (single or multiple copies) of this standard may be obtained by contacting ASTM at the above address or at 610-832-9585 (phone), 610-832-9555 (fax), or service@astm.org (e-mail); or through the ASTM website (www.astm.org).

APPENDIX B

TECHNICAL DRAWINGS AND SOLID MODELS OF DESIGNED SPINAL CAGES

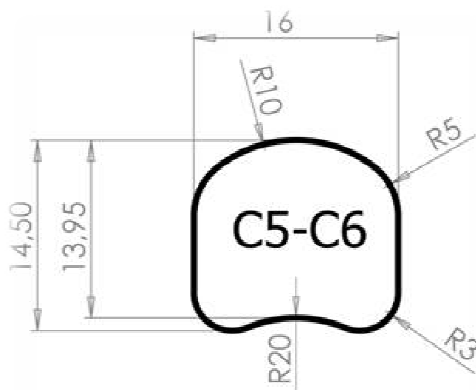


a)



b)

Figure B.1. a) Technical drawing and b) solid model of spinal cage belongs to C3-C4 vertebra segments.

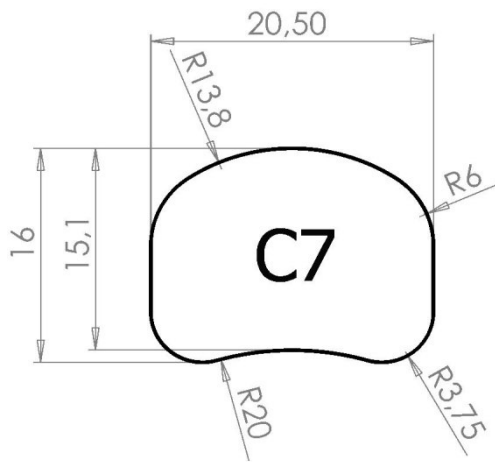


a)



b)

Figure B.2. a) Technical drawing and b) solid model of spinal cage belongs to C5-C6 vertebra segments.

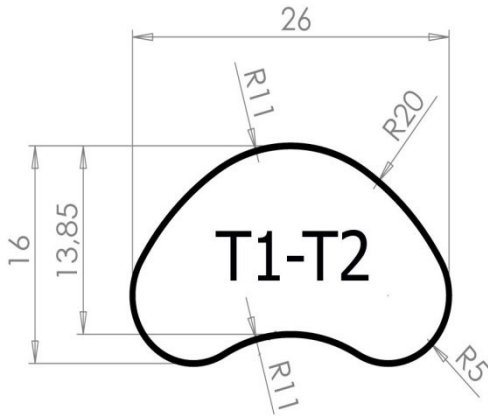


a)



b)

Figure B.3. a) Technical drawing and b) solid model of spinal cage belongs to C7 vertebra segment.

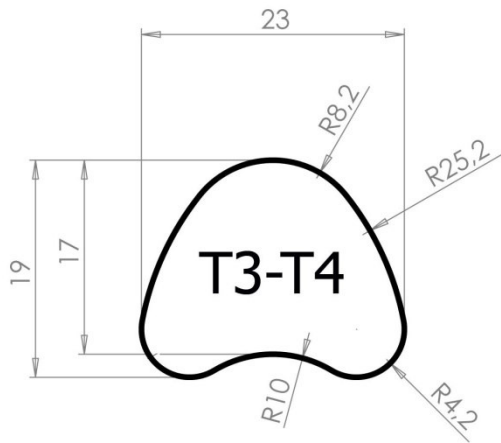


a)

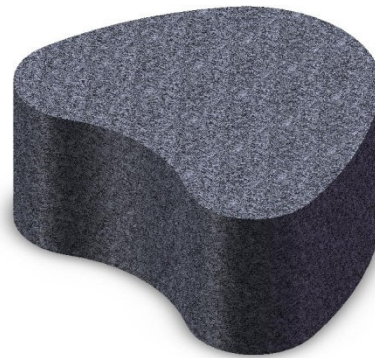


b)

Figure B.4. a) Technical drawing and b) solid model of spinal cage belongs to T1-T2 vertebra segments.

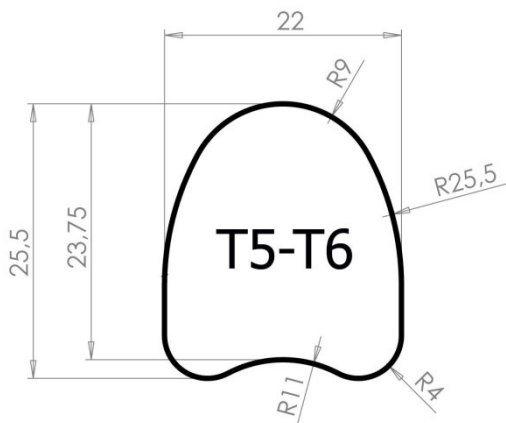


a)

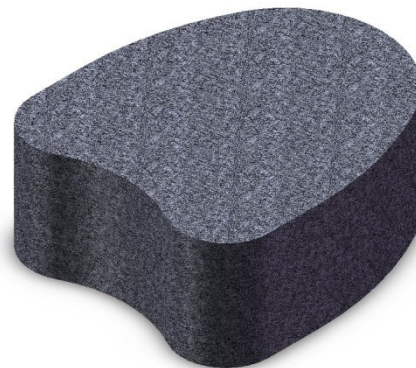


b)

Figure B.5. a) Technical drawing and b) solid model of spinal cage belongs to T3-T4 vertebra segments.



a)



b)

Figure B.6. a) Technical drawing and b) solid model of spinal cage belongs to T5-T6 vertebra segments.

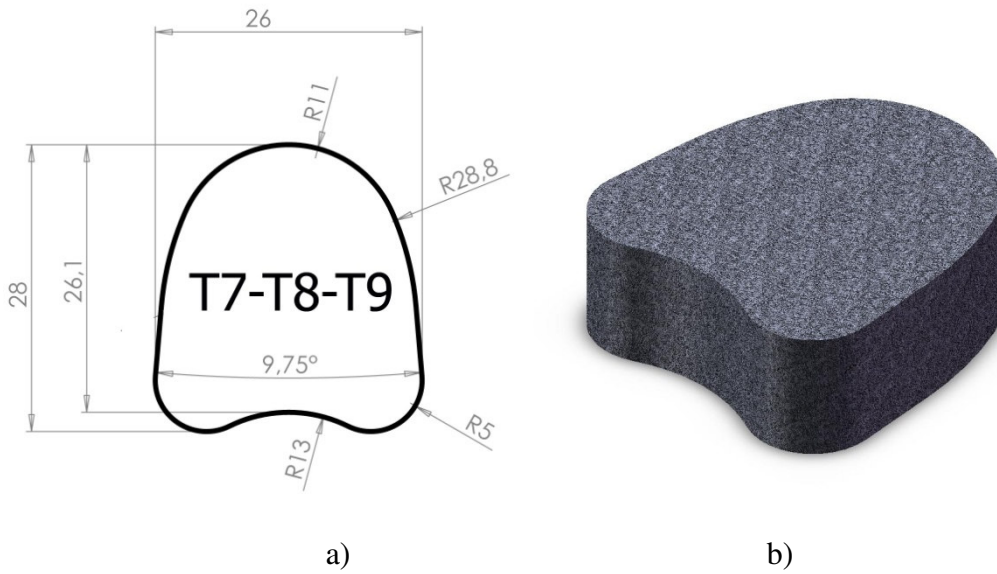


Figure B.7. a) Technical drawing and b) solid model of spinal cage belongs to T7-T8-T9 vertebra segments.

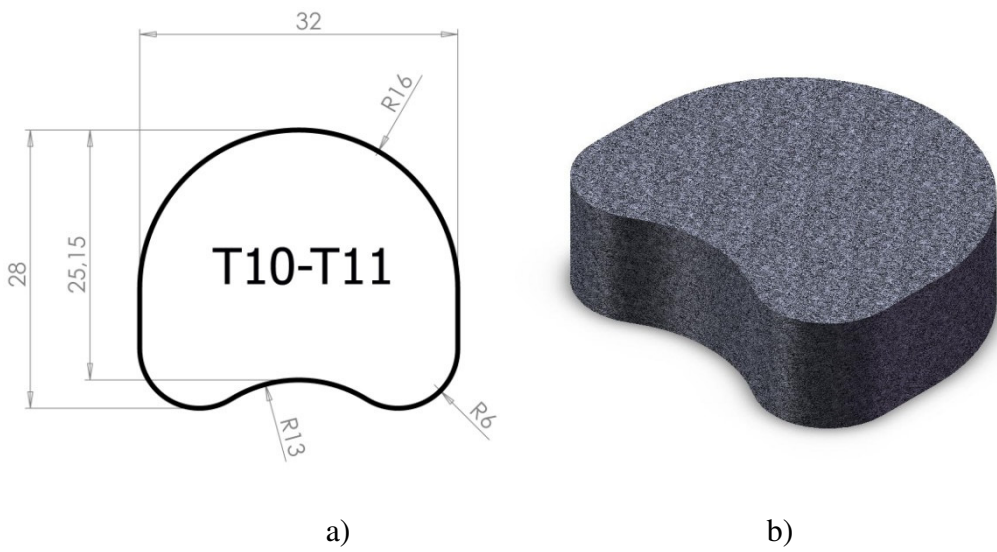


Figure B.8. a) Technical drawing and b) solid model of spinal cage belongs to T10-T11 vertebra segments.

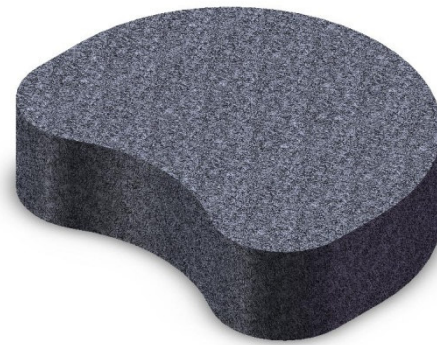
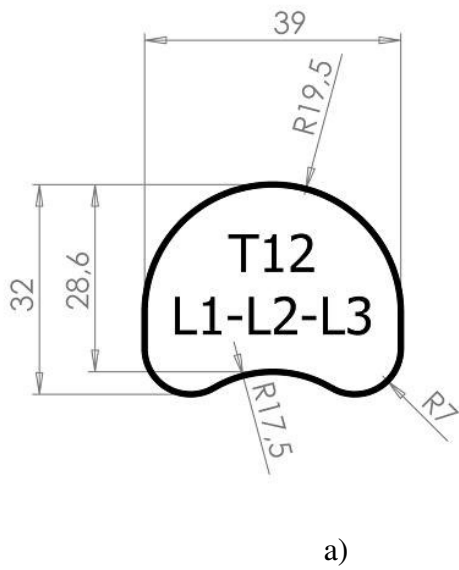


Figure B.9. a) Technical drawing and b) solid model of spinal cage belongs to T12-L1-L2-L3 vertebra segments.

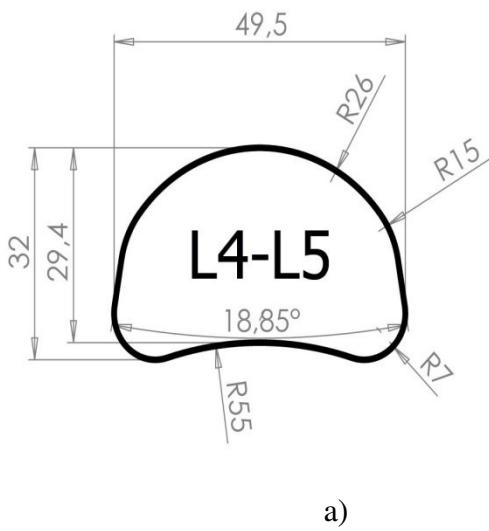


Figure B.10. a) Technical drawing and b) solid model of spinal cage belongs to L4-L5 vertebra segments.